Overview and Optical Design for

DAVINCI: the Diffraction limited Adaptive optics Visible and Infrared iNtegral field spectrograph and Coronagraphic Imager

By Sean Adkins, Renate Kupke, Sergey Panteleev, Mike Pollard and Sandrine Thomas

Version 1.1
April 15, 2010

Table of Contents

1 Introduction 1
2 Scope and Applicability 1
3 Revisions 2
3.1 Revision History 2
3.2 Document Control 2
4 DAVINCI Glossary 2
5 Overview 4
5.1 Science Drivers 4
5.1.1 Imaging Science with DAVINCI 5
5.1.1.1 Imager Pixel Scale 8
5.1.1.2 Imager Sensitivity 10
5.1.2 Spatially Resolved Spectroscopy Science with DAVINCI 12
5.1.2.1 IFS Sensitivity 13
5.2 Design and Build to Cost 15
5.3 The DAVINCI Concept 16
5.3.1 Mechanical Design Concept 18
5.3.1.1 Dewar and Internal Structure 18
5.3.1.2 Mechanisms 19
5.3.2 Interfaces 20
5.3.3 Electronics 20
5.3.4 Software 21
6 Optical Design 22
6.1 Design Drivers and Choices 22
6.2 Optical Performance Goals 23
6.3 Optical Design Description 24
6.3.1 Imager 27
6.3.2 IFS Scale Changer 29
6.4 Design Trades 31
6.4.1 Pupil image quality 32
6.4.2 Image quality 33
6.4.3 Transmission 36
6.4.4 Tolerances 36
6.4.4.1 Optical Manufacturing, Effect on Correctable and Uncorrectable WFE 36
6.4.5 Scale changing relay for IFS 38
6.4.6 Coronagraph 42
6.4.6.1 Assumptions 42
6.4.6.2 Simulation Results 42
6.4.6.3 Results 43
6.4.6.3.1 J Band 44

Table of Contents

6.4.6.3.2 H Band 45
6.4.6.3.3 K Band 45
6.4.6.4 Sensitivity 46
6.4.6.5 Conclusions 46
6.5 DAVINCI IFS 47
6.5.1 IFS Design Considerations 47
6.5.1.1 Lenslet Slicers 48
6.5.1.2 Mirror Slicers 49
6.5.1.3 Hybrid Slicer Design 49
6.5.2 IFS Optical Design 50
6.5.2.1 Lenslet Slicer 51
6.5.2.2 Hybrid Slicer 52
6.5.2.2.1 Hybrid Slicer Optical Layout 55
6.5.2.2.2 Hybrid Slicer Optical Performance 55
6.5.2.2.3 Distortion 57
6.5.2.2.4 Tolerances 57
6.5.2.2.5 Surface roughness 58
6.5.2.2.6 Hybrid Slicer and IFS Transmission 59
6.5.3 DAVINCI IFS Passbands 61
6.5.4 DAVINCI IFS Spectral Formats 61
6.5.4.1 8 Virtual Slits 62
6.5.4.2 6 Virtual Slits 64
6.5.5 DAVINCI IFS Collimator and Camera 67
7 References 68
8 Appendix A – Zemax Prescription 70
8.1 DAVINCI Imager Zemax Prescription 70
8.2 JHK Scale Changer 74
8.3 IZ Scale Changer 76
9 Appendix B: Atmosphere and System Transmissions 79

Figures and Tables

Figure 1: NGAO parameter space 4
Figure 2: DAVINCI photometric wavelength bands and spatial sampling 8
Figure 3: Maximum exposure time to 50% of charge storage capacity in K band 9
Figure 4: DAVINCI opto-mechanical block diagram (not to scale) 16
Figure 5: DAVINCI FOVs 17
Figure 6: MOSFIRE internal structure (cross section) 18
Figure 7: DAVINCI electronics block diagram 21
Figure 8: The DAVINCI optical layout, as seen from directly overhead 25
Figure 9: The DAVINCI optical layout, shown in perspective to emphasize the 2-tier design 26
Figure 10: DAVINCI fore-optics and imager optical layout 27
Figure 11: DAVINCI IFS fore-optics and scale changer 30
Figure 12: IFS scale changer optical layout 31
Figure 13: Pupil footprint at the tilted pupil mask 32
Figure 14: Characteristics of the pupil image at the pupil mask 33
Figure 15: Image quality metrics at the DAVINCI imager's detector plane 35
Figure 16: Geometric spot analysis of visible scale changer 38
Figure 17: Grid distortion analysis for visible scale changing optics 39
Figure 18: Geometrical spot analysis, JHK band scale changer 40
Figure 19: Grid distortion analysis, JHK-band scale changer 41
Figure 20: J band contrast (82.5%, 8) case 45
Figure 21: J band contrast (75%, 5) case 45
Figure 22: H band (90%, 4) case 45
Figure 23: H band (75%, 6) case 45
Figure 24: K band (75%, 5) case 45
Figure 25: K band (75%, 6) case 45
Figure 26: DAVINCI coronagraph companion sensitivity in K band 46
Figure 27: Lenslet slicer based IFS 48
Figure 28: Mirror slicer based IFS 49
Figure 29: Hybrid slicer based IFS 50
Figure 30: Reformatting the 80 x 80 sample pupil plane into 8 pseudo-slits 52
Figure 31: Optical layout of the hybrid slicer 53
Figure 32: Slicing mirrors 54
Figure 33: Pupil images at detector (for $\lambda = 1.5\ \mu m$). 56
Figure 34: Curvature of single sub-slit in spectral direction 57
Figure 35: Rotation angles for gratings (8 virtual slits) 63
Figure 36: Distribution of spectra on the detector using 8 virtual slits 64
Figure 37: Rotation angles for gratings (6 virtual slits) 65
Figure 38: Distribution of spectra on the detector using 6 virtual slits 66

Figures and Tables

Table 1: Summary of the primary science driven parameters for DAVINCI imaging 6
Table 2: Zero points and background magnitudes for DAVINCI imaging 11
Table 3: DAVINCI imaging sensitivity 11
Table 4: Hawaii-4RG performance parameters 11
Table 5: Summary of the primary science driven parameters for an IFS 12
Table 6: Zero points and background magnitudes for DAVINCI IFS 14
Table 7: DAVINCI optical performance goals 23
Table 8: Optical element specifications for the DAVINCI imager 29
Table 9: DAVINCI IFS scale changer requirements 29
Table 10: Characteristics of the pupil image at the pupil mask 32
Table 11: Image quality with and without a field flattener 34
Table 12: Transmission estimates for the DAVINCI imager 36
Table 13: Correctable and uncorrectable wavefront error due to manufacturing figure errors 37
Table 14: Tolerances for optical surface position in both slicing mirrors 58
Table 15: Scattering as a function of wavelength 58
Table 16: DAVINCI IFS transmission estimate 60
Table 17: IFS passbands 61
Table 18: Baseline for groove frequency G (1/mm) 61
Table 19: Diffraction grating parameters for an 8 virtual slit configuration 63
Table 20: Diffraction grating parameters for a 6 virtual slit configuration 65
Table 21: IFS camera and collimator parameters 67
Table 22: Atmosphere and AO system throughput estimates 79
Table 23: Keck telescope transmission 80

1 INTRODUCTION

DAVINCI, the Diffraction limited Adaptive optics Visible and Infrared iNtegral field spectrograph and Coronagraphic Imager is the first light science instrument for the Keck Next Generation Adaptive Optics system (NGAO) at the W. M. Keck Observatory (WMKO).

DAVINCI is a fully cryogenic instrument providing imaging at the diffraction limit over a wavelength range of 0.7 μm to 2.4 μm with a fixed plate scale of 8 milliarcseconds (mas). The field of view (FOV) for imaging is 32.8" x 32.8" using a Teledyne Hawaii-4RG detector with 4096 x 4096 pixels and a 2.5 μm cut-off wavelength. The imager provides a selectable coronagraph mask and a large selection of photometric, continuum, and narrow band filters. A tracking cold pupil mask is provided for H and K band observations, and an additional selection of pupil masks is provided for the shorter wavelength bands and for the coronagraph mode.

DAVINCI also provides integral field spectroscopy (IFS) with a baseline configuration of 80 x 80 spatial samples over a wavelength range of 0.7 μm to 2.4 μm. Samplings scales of 10, 35, and 50 mas are provided, resulting in an FOV of 0.8" x 0.8", 2.8" x 2.8", and 4" x 4". A deployable pick-off mirror located on axis sends the central portion of the DAVINCI FOV to the IFS. The IFS is located near an intermediate focal plane to minimize vignetting, allowing simultaneous spectroscopy and imaging. Fixed gratings are provided for each wavelength range, operating in the first order near the blaze angle with R ~4,000. The IFS is optimized for narrow band observations (~5% bandpass) and uses a lenslet image slicer combined with novel reformatting optics to provide 6 virtual slits (512 pixels per spectra) on a Hawaii-4RG detector with a 2.5 μm cut-off wavelength.

This document provides an overview of the DAVINCI instrument and describes the DAVINCI optical design.

2 SCOPE AND APPLICABILITY

This document describes the preliminary optical design for the DAVINCI fore-optics and imager, and the conceptual design for the DAVINCI integral field spectrograph (IFS).

3 REVISIONS

This revision of the document is as a template for the preparation of the report.

3.1 Revision History

Revision	Date	Author	Reason for revision / remarks
0.1	March 17, 2010	SMA	Template for report, not released
1.0	April 13, 2010	SMA	Released for review

Due to the difficulties encountered with documents using moderately complex formatting such as this one, the Microsoft Word "Track Changes" feature is not useable. To see the changes in this document since the previous revision, use the "Tools, Track Changes, Compare Documents" drop down menu sequence and compare this document to the previously released version. It is not recommended that you attempt to print the results. There is no previously released version of this document. Subsequent versions of this document will include the filename and date for the previous version.

3.2 Document Control

This is not a controlled document.

4 DAVINCI GLOSSARY

The following names and definitions are adopted for the components of DAVINCI:

DAVINCI: the complete system consisting of the DAVINCI instrument and associated computers, private network, software and accessories.

DAVINCI Instrument: the telescope-mounted portion of DAVINCI consisting of the dewar, electronics rack and interconnecting cables.

Dewar: a vacuum cryostat chamber containing the imager and integral field spectrograph science optical paths, science detectors, and associated components.

DAVINCI Instrument Electronics Rack: an EMI tight, forced air cooled EIA 19 inch equipment rack that provides a single bay with 45 U of panel space with tapped EIA 19 inch rack mounting rails. The electronics cabinet is located in the AO electronics vault on the Keck II right Nasmyth platform.

DAVINCI Computer: a computer dedicated to providing software functions for DAVINCI. There will be three of these, and they are divided into two broad categories, host and detector targets.

DAVINCI will use a client-server architecture. Low-level servers implement Keck keyword communications for clients and low level interfaces to instrument hardware to allow keyword control of the instrument. A global server is used to coordinate keyword activities by multiple low level servers. Low-level server applications can run on either the host computer or a target computer. Low-level servers that demand significant amounts of processor resources are often deployed on dedicated computers; these are commonly called target computers. The host computer is the computer where the user interface applications are run, even though this same computer may also run on or more of the server applications as well.

DAVINCI Target Computer: a computer dedicated to running one or more low-level server applications that provide keyword control of DAVINCI hardware systems. A target computer has one or more hardware interfaces to subsystems of the instrument such as detectors or mechanism motion control.

DAVINCI Host Computer: the computer where the DAVINCI global server and user interface software is run.

DAVINCI Computer Rack: an EIA 19 inch rack located in the Keck II computer room and housing the DAVINCI computers, data storage disk array, private network interfaces and related components.

5 OVERVIEW

5.1 Science Drivers

DAVINCI is expected to offer high performance imaging and spectroscopy for science observations with NGAO. The top level science driven requirements (Table 1 and Table 5) for DAVINCI are:

1. Diffraction limited imaging from 0.7 to 2.4 μm with at least 3 pixel sampling to 1 μm, and 2 pixel sampling to 0.7 μm
2. High throughput
3. Imaging over an FOV that is as large as possible for NGAO, ~20" to 30" diameter
4. Integral field spectroscopy from 0.7 to 2.4 μm with spatial scales suited to the diffraction limit and the maximum ensquared energy provided by NGAO
5. Coronagraphic imaging with contrast of at least 10^{-4} from 1 to 2.4 μm over an inner working angle of 200 mas

NGAO offers a significantly extended parameter space for these observations, both in terms of spatial resolution and wavelength range. Figure 1 illustrates this parameter space.

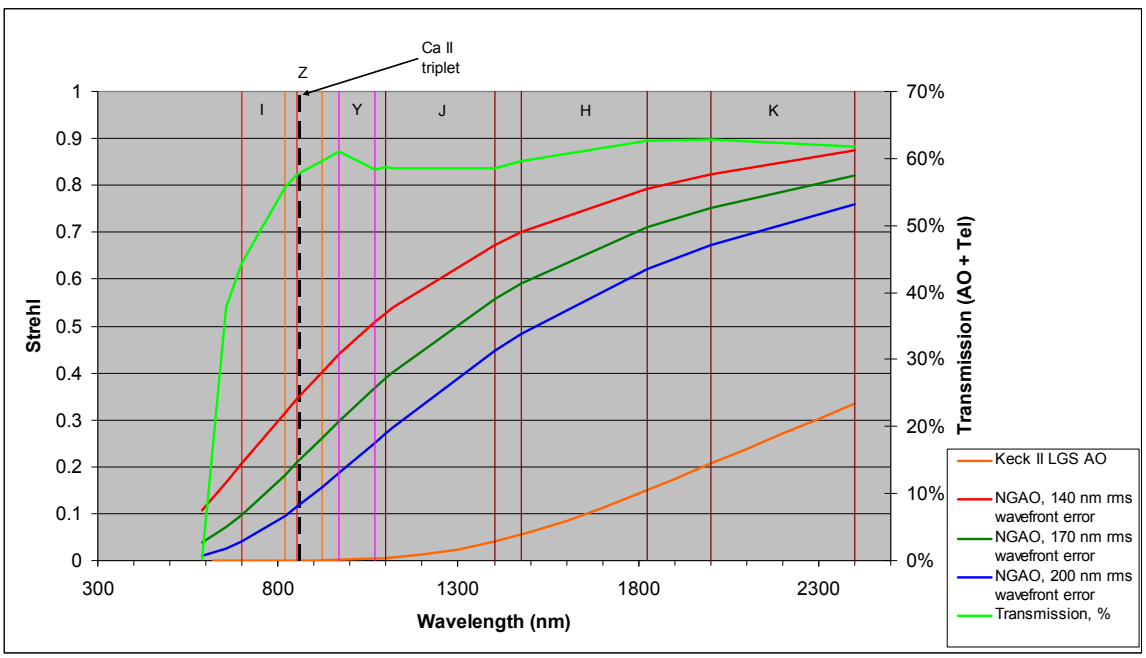

Figure 1: NGAO parameter space

The performance expected from the NGAO system (Dekany et al., 2009) includes average Strehls of at least 15% in the I band and performance of ~78% in the K band, assuming 170 nm rms of

residual wavefront error. Detailed studies of the performance for various science cases and sky coverage fractions support the view that imaging capability suited to the diffraction limit will provide excellent results over the wavelength range of 0.7 to 2.4 μm. The combination of the AO system and imaging capability are expected to support high accuracy relative photometry and high accuracy astrometry. The imaging capability is also expected to have high throughput and appropriate background suppression in order to take advantage of the low backgrounds provided by NGAO, and the imaging capability must provide a coronagraph to support the detection and characterization of planets around nearby low mass stars.

An integral field spectrograph (IFS) is recognized as an ideal way to take advantage of the image quality offered by NGAO because of its ability to provide spatially resolved spectroscopy of diffraction limited images without suffering from losses due to a mismatch between a long slit and the shape of a complex object. IFS data can provide information essential for deconvolution of the point spread function (PSF) and offers a comprehensive tool for determining kinematics, mass distributions and velocity dispersions.

5.1.1 Imaging Science with DAVINCI

DAVINCI's imaging capability represents a general purpose tool that will be expected to serve a wide range of scientific needs as well as provide a tool for characterizing the performance of the NGAO system. The imager's performance requirements are in turn defined from two viewpoints, the NGAO science cases, and a technical viewpoint that defines the requirements for performance measurement. Here we will consider the science driven performance requirements with an understanding that satisfying the most demanding of these will also provide the performance needed for AO system characterization.

The general purpose nature of the imaging capability is reflected in the number of NGAO science cases that require imaging. Based on a review of those science cases, the important performance parameters for the imaging capability are summarized by science case in Table 1.

Several of these science cases identify the desirability of accessing wavelengths below 1 μm, either for specific diagnostic lines such as the Ca II triplet (~850 nm), or for the improved spatial resolution available at the shorter wavelengths. A number of the science cases also require high levels of performance from astrometric and photometric measurements obtained from NGAO observations. Initial evaluation of the I band for color-color diagrams indicates that extending coverage to this band will prove highly beneficial to the study of stellar populations.

Science Case	Wavelength Coverage†	Field of View	Spatial Sampling	Sensitivity and SNR	Other requirements
Measurements of General Relativity Effects in the Galactic Center*	H, K (1.49 to 2.37 μm)	10" x 10"	At least λ/2D sampling	Better than current AO system with NIRC2	Astrometric performance > 0.1 mas
Imaging and Characterization of Extrasolar Planets around Nearby Stars*	Y, J, H, K (0.97 to 2.37 μm) Also below Y to 0.9 μm	< 5"	Diffraction limited sampling. At least 1.5 x better than λ/2D sampling at J (goal Y)	10^{-4} contrast at 200 mas separations, goal of coronagraph with inner working angle of 70 to 100 mas. ΔH = 13 at 1" separation, H = 25 for σ = 5 in 20 minutes.	R ~100 spectroscopy? Relative photometry to accuracy ≤ 0.1 magnitudes, astrometric precision of 2 mas. 6 λ/D general purpose coronagraph.
Multiplicity of minor planets*	Z, Y, J, H, K (0.818 to 2.37μm)	≤ 4"	Diffraction limited, λ/3D for J, H, and K-bands, or λ/2D for R and I-bands		
Gravitational Lensing	I, Z, Y, J, H, K (0.7 to 2.37 μm)	≥ 15" dia., goal of 30" dia.	Diffraction limited, λ/2D		Relative photometry to accuracy ≤ 0.1 magnitudes
Size, shape, and composition of minor planets	Z, Y, J, H, K (0.818 to 2.37 μm) I band to 0.7 μm desirable for asteroid shapes	≤ 4"	Diffraction limited, λ/3D for J, H, and K-bands, or λ/2D for R and I-bands	R = 29 for 5σ in 1 hour (from NGAO proposal, table 14)	R ~100 spectroscopy?
Characterization of Gas Giant Planets	J, H, K (1.17 to 2.37 μm)	≥ 30" dia. in K, ≥ 20" dia. in J,H	Diffraction limited, λ/2D or finer sampling	Moons are very bright, need a large dynamic range, short exposures	
Resolved Stellar Populations in Crowded Fields	I, Z (0.7 to 0.922 μm), J, H, K (1.1 to 2.37 μm)	≥ 15" dia.	Diffraction limited, λ/2D or finer sampling	K = 27 for σ = 5 in one hour	

Table 1: Summary of the primary science driven parameters for DAVINCI imaging

* = NGAO key science driver

† = Photometric filter passbands

Photometric accuracy depends strongly on the stability of the point spread function (PSF). For observations of closely spaced targets, accurately modeling the PSF becomes critical to successfully employing deconvolution techniques to separate the flux contributed by each object. Britton et al. (2007) suggest that effects due to imperfect correction of atmospheric turbulence and field dependent aberrations will be dominant over effects due the instrumentation. Non-common path errors between the science instrument and the AO system will contribute to instability of the PSF at the instrument. Motion within the instrument structure during an observation (flexure) can

also contribute to PSF variability. Flexure is not expected to be a problem for DAVINCI as its structure is completely fixed, and there are no moving parts that can induce differential motion between parts of the optical path during an observation. We will not attempt an extended discussion of the instrumental contributions to photometric accuracy, but detector characteristics are expected to be the dominant factor in the instrument's photometric performance. Such effects are well understood and largely controllable with good design practices.

The accuracy of position determination or astrometry for a point source is ultimately determined by the width of the PSF and noise in the image due to photon statistics, sometimes referred to as the photonic limit. As with photometric accuracy, the performance of the AO system, including the Strehl and the quality of the PSF both affect the signal to noise ratio (SNR) of the observation. As discussed in Cameron et al. (2007) additional impacts on astrometric accuracy arise from AO performance issues such as variable angular displacement across the FOV due to differential tip-tilt anisoplanatism, and changes in plate scale that may result from blind modes in multi-conjugate AO (not currently a planned operating mode for the NGAO system).

In addition to sensitivity, the primary effect of the instrument on astrometric accuracy will be the amount of distortion present in the optical system. In addition to minimizing the presence of distortion through careful design and construction a high performance approach to measuring the distortion across the field of the imager will be required. Such characterization has been shown to have a significant impact on the astrometric accuracy that can be achieved with the existing Keck II AO system and the NIRC2 instrument (Cameron et al., 2007). It should be noted that the Galactic center case makes the greatest demand on astrometric accuracy at < 0.1 mas, an accuracy approaching the limit of what can be achieved due to photon statistics.

The pixel scale at the detector will determine the sampling of the delivered PSF and in turn will have an impact on both photometric and astrometric accuracy. The effects of sampling on the spatial frequency content of the PSF image can be appreciated using the techniques common to understanding the MTF of digital imaging systems. The loss of spatial frequencies due to sampling will translate directly to a reduction in the accuracy with which the original flux distribution is represented in the sampled image, and will also result in an increase in position uncertainty for well resolved image features.

For the specific case of imaging of multiple asteroid systems Baek and Marchis (2007) have undertaken simulations which indicate that pixel scales resulting in three pixel sampling across the diffraction limited image size (a pixel scale of $\lambda/3D$) results in the best representation of the flux ratio between the primary and the secondary in the J, H and K bands. For near-IR wavelengths for which the chosen object sizes are well resolved (J and H band) Baek and Marchis also report that three pixel sampling produces good results for position measurements. In the I band the shorter wavelengths offer higher spatial resolution, but the decrease in Strehl reduces the SNR of the

simulated observations, and as a result two pixel sampling (a pixel scale of λ/2D) provides the best representation of the flux ratio and the most accurate position measurements.

5.1.1.1 Imager Pixel Scale

For reasons of complexity, optical performance, and cost we consider it desirable for the DAVINCI imaging mode to have a single fixed pixel scale. The considerations for the DAVINCI imager's pixel scale are described in detail in Adkins (2010) and are summarized here.

As described in Kupke (2009) the NGAO science relay will offer an unvignetted field of view (FOV) covering 40" diameter. Given a square detector, the square area that will fall entirely within a 40" FOV is 28.28" x 28.28". Given a 4096 x 4096 pixel detector, the corresponding pixel scale is 7 mas. A second candidate is an 8 mas scale, which provides a FOV of 32.8" x 32.8". As noted in the previous section, the imager should have a pixel scale that provides at least 3 pixel sampling in the near-IR bands, and at least 2 pixel sampling in the Z and I bands. The sampling obtained in each waveband for pixel scales of 7 and 8 mas is illustrated in Figure 2.

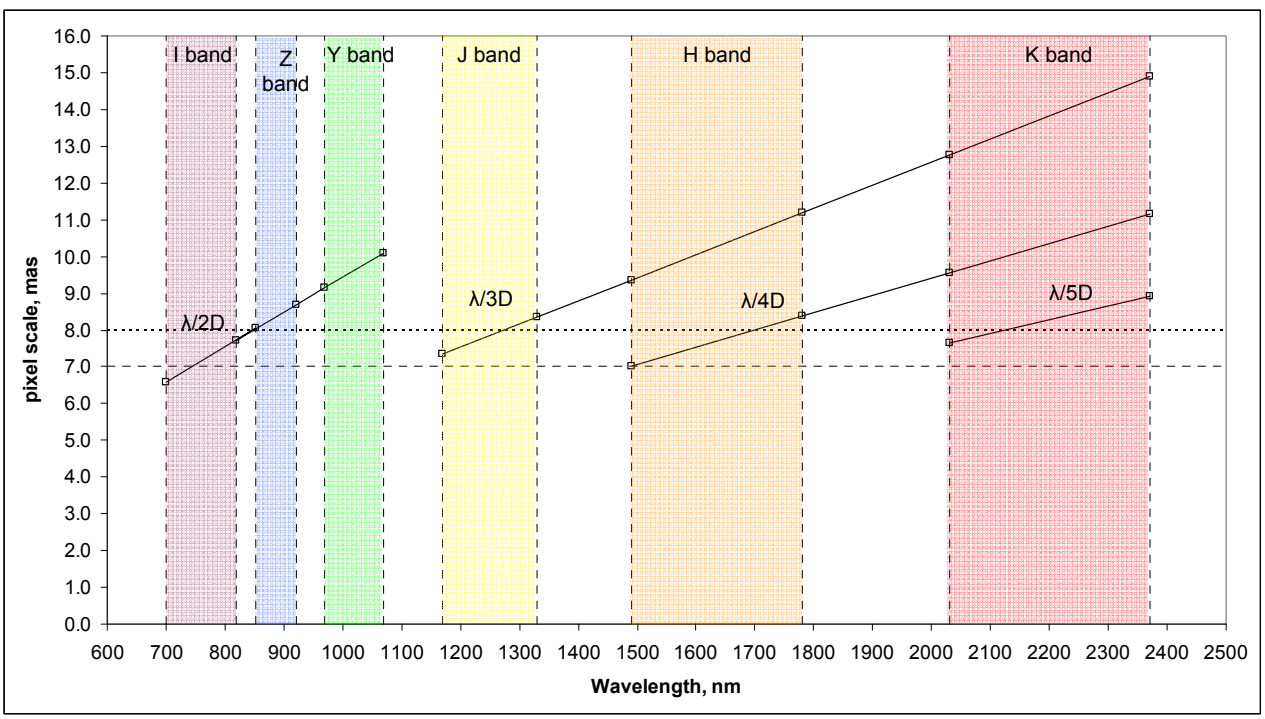

Figure 2: DAVINCI photometric wavelength bands and spatial sampling

From Figure 2 we can see that a 7 mas pixel scale would provide >2 pixel sampling down to near the I band cut-on wavelength, >2 pixel sampling in the Z and Y bands, >3 pixel sampling in the J band, ≥ 4 pixel sampling in H, and > 5 pixel sampling in K band. An 8 mas pixel scale would provide 1 to 2 pixel sampling in I band, >2 pixel sampling in the Z and Y bands, 2 to 3 pixel

sampling in the J band, 3 or more pixel sampling in H, and 4 to 5 pixel sampling in K band. The benefit of the 8 mas pixel scale would be an increased FOV.

The trade off between pixel scale and background limited exposure time has been evaluated for a range of pixel sizes. As shown in Figure 3, smaller pixels receive less background per pixel, but as can also be appreciated more pixels also increase the read noise contribution. Fortunately the Hawaii-2RG detector has demonstrated read noise of ~4 e- with 16 Fowler samples (Kulas, 2010), considerably reducing the impact of oversampling due to a fixed pixel scale. The time required for 16 Fowler samples with 100 KHz pixel rate is 23 s.

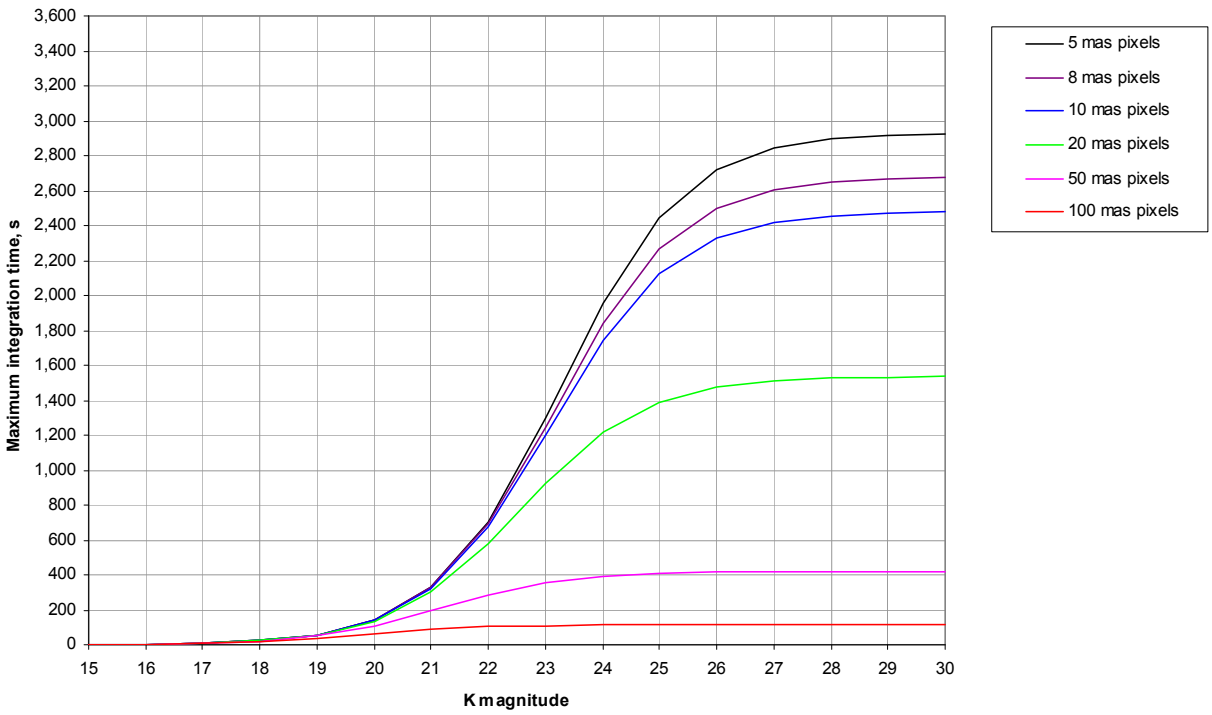

Figure 3: Maximum exposure time to 50% of charge storage capacity in K band

For the infrared bands the sky background is the dominant factor in the SNR as indicated by the relatively short exposure times required to reach a background limited exposure (Table 3). This is also reflected in the limited impact on 5σ limiting magnitude for the range of pixel scales from 50 mas to 5 mas as shown in **Error! Reference source not found.**. This suggests there is no compelling sensitivity argument to guide the choice of pixel scale in the range around choices that address the diffraction limited sampling requirements for DAVINCI, and also suggests that oversampling at longer wavelengths does not result in a penalty for SNR.

On the other hand, within the infrared bands the sky background does limit the maximum exposure time before either the accumulated charge rises to the point where the detector's response becomes non-linear or saturates. Here, smaller pixels are better, allowing significantly longer exposure times.

Finally, when the benefit of a larger field of view is considered it seems logical to consider either the 7 or 8 mas pixel scale as the best single choice. The 8 mas scale offers shorter exposure times to reach a background limited condition, and also offers a field of view that takes better advantage of the 40" diameter FOV of the AO system. For this reason we have baselined the 8 mas scale. It does have the disadvantage of under sampling the I band, where the Strehl is an average of 15%. Given the relatively broad PSF this under sampling is probably acceptable. However, there is no significant penalty except for a reduction in FOV if the 7 mas scale is adopted instead. This change would have minimal impact on the optical design.

5.1.1.2 Imager Sensitivity

The imager photometric passbands, zero points, and background predictions for DAVINCI imaging are shown in Table 2. The sensitivity predictions for DAVINCI imaging are shown in Table 3. The background predictions are based on a cooled AO system operating at a temperature of -15 °C and emissivity for the LGS observing mode assuming degraded optical transmission due to dust and aging of coatings. The background predictions include the effects of moonlight (50% dark time) for the I and Z band. Average transmission in each passband is used for the atmosphere, telescope, and AO system. The values for these transmissions are given in appendix B. The DAVINCI imager transmission values for each passband are shown in Table 12. Thermal background within DAVINCI is suppressed by operating the instrument at 120 K in a vacuum dewar.

The zero point magnitudes and the sensitivity predictions (Table 3) are based on the detector characteristics summarized in Table 4. Sensitivities are calculated assuming the delivered NGAO Strehl based on 170 nm wavefront error. The required aperture for a diffraction limited image is assumed to be that needed for a well compensated image (Hardy, 1998, p. 42), i.e. a diameter equal to $2\lambda/D$ where D is the diameter of the telescope aperture, and λ is the long wavelength cut-off in the passband of interest.

.

Table 2: Zero points and background magnitudes for DAVINCI imaging

Photometric Passband	Cut-on, nm	Cut-off, nm	CWL, nm	Zero point	Background, mag./sq. arcsecond
I band photometric	700	853	776.5	27.42	22.13
Z band photometric	818	922	870	27.24	21.28
Y band photometric	970	1070	1020	26.97	17.28
J band photometric	1170	1330	1250	27.05	16.04
H band photometric	1490	1780	1635	27.07	13.76
K band photometric	2030	2370	2200	26.52	14.78

Table 3: DAVINCI imaging sensitivity

Photometric Passband	Ave. Strehl (170 nm wavefront error)	Time per exposure	5σ mag.	Time for single exposure to background limit, mag. = 27
I band photometric	15%	120 s	27.8	6.7 h
Z band photometric	22%	120 s	27.9	5.6 h
Y band photometric	33%	900 s	28.0	1800 s
J band photometric	39%	900 s	27.4	560 s
H band photometric	59%	900 s	26.5	70 s
K band photometric	79%	900 s	26.7	280 s

Point source limiting magnitude for 4 co-added exposures to reach 5σ in 1 hour for Y through K bands, and 8 minutes for I and Z bands

Table 4: Hawaii-4RG performance parameters

Parameter	Min. Value	Notes
Dark Current	0.01 e^-/s	Median dark current of all imaging pixels
Charge Storage Capacity	100,000 e^-/pixel	Array average number of electrons where the photon transfer curve first deviates from a straight line
Read Noise	15 e^-/pixel	Per CDS read
Quantum Efficiency	0.80 0.75 0.70	970 to 2400 nm 850 to 970 nm 700 to 850 nm

5.1.2 Spatially Resolved Spectroscopy Science with DAVINCI

DAVINCI's IFS capability is intended to meet the needs of a range of Galactic and extra galactic science observations. We have evaluated the key IFS performance parameters and determined that the parameters most critical to IFS science are wavelength coverage including the placement of the short wavelength cut-off, spectral resolution, FOV, spatial sampling, and sensitivity. Table 5 gives the values of these parameters for each of the science cases that represent the primary drivers of IFS performance for DAVINCI.

Science Case	Wavelength Coverage	Spectral Resolution	Field of View	Spatial Sampling	Sensitivity and SNR
Galaxy Assembly and Star Formation History*	Z, Y, J, H, K (0.818 to 2.4 μm), narrow band coverage acceptable since redshifts will be obtained before IFS observations	R >3000 (for OH line removal and discrimination of key diagnostic lines (Hα vs. NII)	1" x 3" or greater	Optimized for 50% ensquared energy, range of 50 to 100 mas acceptable	K band performance improvements needed (lower background). Seeking 5 times better sensitivity than OSIRIS on current Keck AO system
Nearby Active Galactic Nuclei*	Z, Y, J, H, K (0.818 to 2.4 μm, or at least to below 850 nm for the Ca II triplet)	R ~3000 to 4000	≥ 5" dia.	20 mas in the near-IR, 8.5 mas in Z	High spatial resolution and precision radial velocities
Measurements of General Relativity Effects in the Galactic Center*	H, K (1.475 to 2.4 μm), primarily narrow band observations of specific absorption lines	R ~4000	≥ 5" dia., goal of 10" dia.	20 mas (H band) and 35 mas (K band)	RV precision at least 10 km/s
Gravitational Lensing	I, Z (0.7 to 1.05 μm), J, H, K (1.10 to 2.4 μm)	R ~4000	> 4" dia., goal of 8" to 10" dia.	50 mas or smaller	RV precision at least 20 km/s (1 σ)

Table 5: Summary of the primary science driven parameters for an IFS

* = NGAO key science driver

In the IFS design one of the key performance trades is the relationship between spectral coverage, spectral sampling, and FOV. For a given number of detector pixels one can trade between these three parameters, finding that certain combinations are more efficient in using the available detector area than others. Our analysis indicates that the NGAO science cases requiring IFS observations are generally more concerned with obtaining a larger FOV than they are with full coverage of an entire IR or visible passband in one exposure.

For example, the Galactic Center case emphasizes the measurement of absorption lines in the H and K bands (such as HI absorption of Brγ emission at 2.166 μm) that fall within 5% band passes, while FOVs of 5" diameter are desirable for simultaneous measurements of multiple stars near the

Galactic center to improve the strength of the orbital solutions. Measurements of GR effects at the Galactic center demand high SNR and diffraction limited spatial sampling. FOV and sensitivity are also important for population studies at the Galactic center (Lu et al., 2009).

Similarly, for emission line observations such as excitation temperatures, observations of molecular hydrogen emissions (Beck et al., 2008), and other spectral line features such as the CO bandheads, 5% band passes will suffice. For the galaxy assembly and star formation case the primary requirement is sensitivity, while FOV is less important provided that it is large enough that sufficient spatial pixels are available to accurately sample the sky background. For this science case since the targets are of known redshifts, and the key spectroscopic lines of interest for kinematics at redshifts of $1 < z < 3$ are observable within ~5% passbands in the near-IR (J, H, and K) bands, a narrow band pass is also satisfactory.

Because the solution for black hole mass requires having a good model for the larger-scale structure of the galaxy the nearby AGN science case has a need for larger FOVs of 3" to 5" diameter, but again the observations required for the stellar and gas dynamics around the central black hole are based on absorption lines for stellar dynamics and emission lines for gas dynamics, all of which can be observed within 5% band pass or less in the z through K bands. This science case in particular identifies the benefits of high angular resolution observations below 1 μm wavelength where the more compact PSF core at the shorter wavelength and the reduced sky background will enable BH detection over greater distances. Gravitational lensing also requires high SNR and an FOV of at least 4" to 5". The lensing science case can also benefits from observations below 1 μm for access to diagnostic lines for the lensed source and for red shifted lines of the lensing galaxy.

In cases where observations of multiple lines are required, if the IFS field is suitably matched to the object size, such that the entire PSF of the object is imaged, then image motion can be detected and discounted using simple PSF fitting techniques (Roth, 2006). This allows multiple narrow band exposures to be a practical alternative to a single broad band exposure.

5.1.2.1 IFS Sensitivity

The predicted sensitivity for the DAVINCI IFS is shown in Table 6. This table is based on the predicted transmission of the IFS, and the assumptions for Strehl, atmospheric transmission, background, and detector as described in §5.1.1.2.

Table 6: Zero points and background magnitudes for DAVINCI IFS

Passband	Cut-on, nm	Cut-off, nm	CWL, nm	Zero point	Background, mag./sq. arcsecond
I band spectroscopic	700	853	776.5	26.48	22.13
Z band spectroscopic	855	1050	952.5	26.90	20.68
Y band spectroscopic	970	1120	1045	26.49	17.05
J band spectroscopic	1100	1400	1250	26.89	16.33
H band spectroscopic	1475	1825	1650	26.40	13.79
K band spectroscopic	2000	2400	2200	25.85	14.62

5.2 Design and Build to Cost

DAVINCI originates within the design and build to cost requirement for NGAO, and is based on a design and build to cost approach supported by six principles:

1. Ensure that the instrument capabilities are well matched to key science requirements
2. Ensure that the instrument capabilities are matched to the AO system in order to maximize the science gains
3. Understand which requirements drive cost
4. Resist the temptation to add features
5. Maximize heritage from previous instruments
6. Evaluate ways to break the normal visible/near-IR paradigm of using different detectors in separate instruments

The concept developed for DAVINCI is aimed at satisfying principles 1 and 2 as fully as possible. The main aspects of the concept as described here are then intended to address the remaining principles with a clearly cost driven approach supported by sound engineering and technical decisions. The design adopts significant portion of subsystem designs from previous instruments, in particular the MOSFIRE (McLean et al., 2008) and OSIRIS (Larkin et al., 2006) instruments. To meet the cost requirements DAVINCI incorporates two instrument capabilities (imaging and spectroscopy) in a single cryogenic dewar with common fore-optics. The single dewar offers significant cost savings by eliminating the need to duplicate the dewar itself as well as cryogenic cooling and a number of control and supervisory systems such as temperature control and pressure monitoring.

A second important aspect of the design concept addresses principal 6, and that is the use of substrate removed HgCdTe infrared focal plane arrays (FPAs). The substrate removed FPAs have good (~70%) QE down to 500 nm, and although the single CDS read noise is higher than typical science grade CCDs (~15 e^-/read for a Hawaii-2RG vs. 5 e^-/read for a deep depletion CCD, see Adkins, 2009) the low power dissipation of the FPA read out integrated circuit and non-destructive pixel read out allows many Fowler or up the ramp samples and results in essentially the same readout noise levels for exposures where the exposure duration allows time for the required number of reads. The result is that while the QE of CCDs will be at least 20% higher at 1 μm and below, this seems to be the only penalty for not using a CCD below 1 μm. This represents another important component of the cost reduction needed in order to ensure that DAVINCI supports the NGAO design and build to cost requirement.

5.3 The DAVINCI Concept

A block diagram of DAVINCI is shown in Figure 4. DAVINCI is a fully cryogenic infrared and optical (to 0.7 µm) imager and IFS enclosed in a vacuum dewar. The dewar contains two optical systems, one for the imager shown in the upper portion of the block diagram, and one for IFS, shown at the bottom center of the block diagram. The FOVs of the imager and IFS are both at the center of the NGAO science FOV as illustrated in Figure 5.

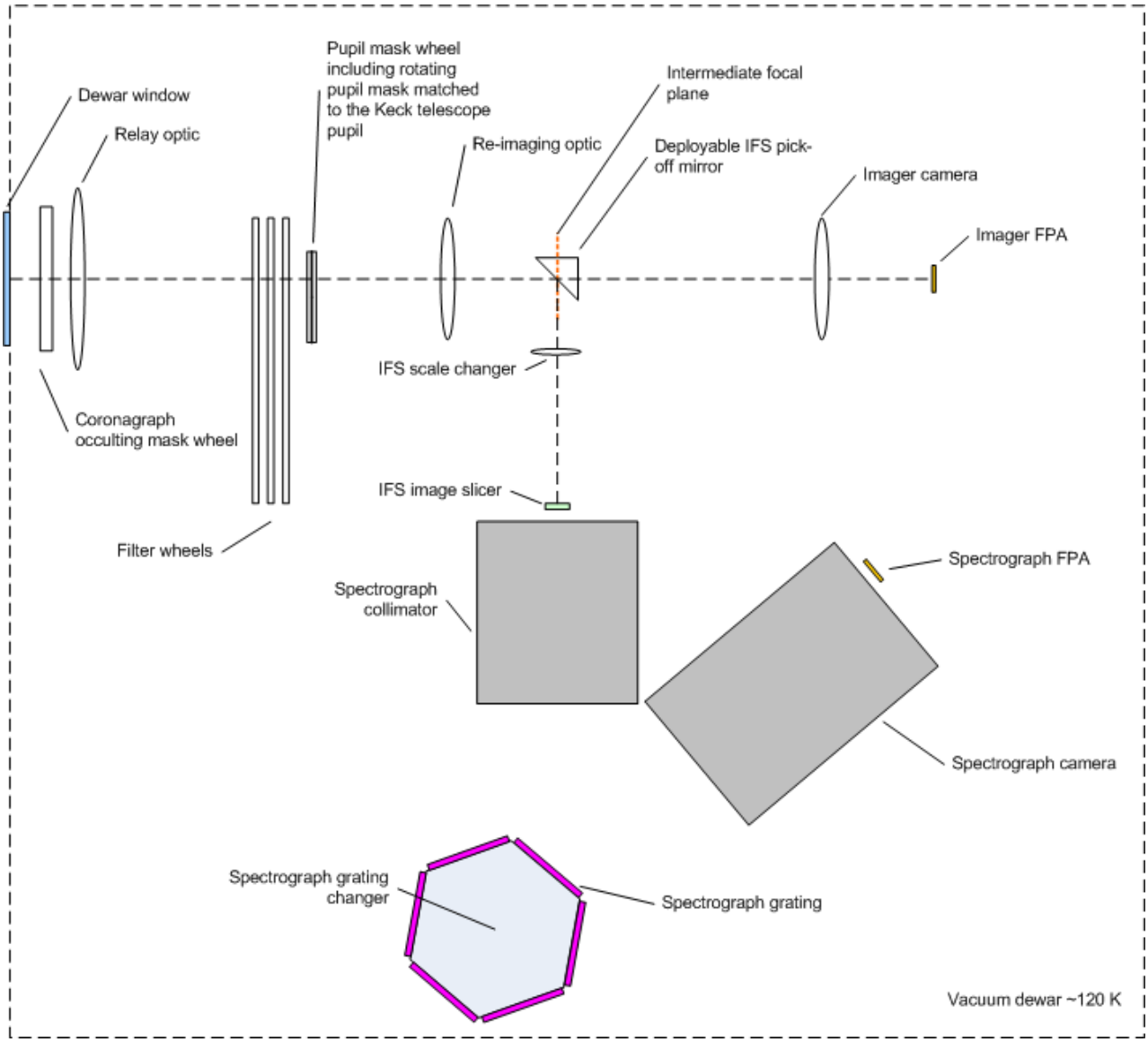

Figure 4: DAVINCI opto-mechanical block diagram (not to scale)

Starting at the top left side of the block diagram, light enters the dewar from the AO system through a vacuum window ~120 mm in diameter. The window is coupled to the NGAO system's cooled enclosure via a light and air tight bellows. The bellows isolates the two structures mechanically, and since the AO enclosure is cooled to -15 °C and filled with dry air, the emissivity of the window is reduced and the issue of condensation or ice on the window is eliminated during normal operation. A mechanism such as a dry air purge will need to be provided for the window during servicing or testing to prevent condensation when the window is exposed to ambient conditions.

The AO system's science focal plane is located inside the dewar where a wheel is located providing a selection of coronagraph occulting masks. A relay optic forms a pupil image at a wheel carrying a selection of cold pupil masks for imaging and coronagraphy including a tracking pupil mask matched to the primary mirror aperture and central obscuration of the Keck telescope.

A set of filter wheels is located just in front of the pupil plane, with ~45 filters shared between the imager (24) and the IFS (17). Each wheel will contain ~15 filters plus an open position. After the pupil mask a re-imaging optic forms an intermediate focal plane. Continuing to the right along the imager optical path this intermediate focal plane is followed by the imager camera and detector.

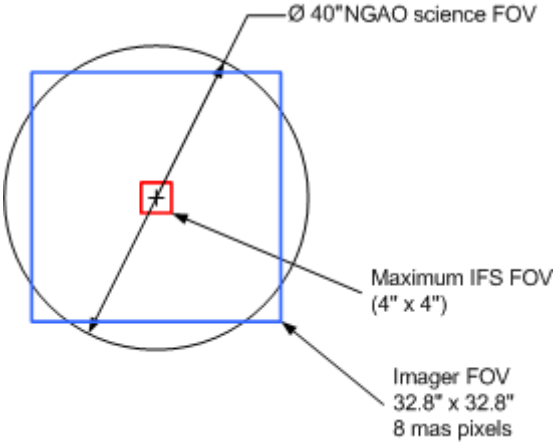

Figure 5: DAVINCI FOVs

Returning to the center of the diagram, the optical path to the IFS starts with a deployable pick-off mirror located near the first intermediate focal plane. This mirror sends the center of the intermediate focal plane to the IFS shown at the bottom center of the block diagram. The beam enters the IFS scale changer, which has three selectable scale changing optics to provide three spatial sampling scales for the IFS. The scale changer focuses the light on the IFS image slicer (baselined as a 80 x 80 lenslet array) and is then collimated by a three mirror anastigmat (TMA). The collimator TMA illuminates a grating working in the first order, and the dispersed light is then imaged onto the spectrograph detector by a second TMA. Multiple gratings will be used with a rotary grating changer to select the appropriate grating for each waveband.

5.3.1 Mechanical Design Concept

The key mechanical design feature of the NGAO science instrument is the re-use of the MOSFIRE dewar design. This may seem like an unusual choice but with appropriate modifications the concept has several benefits. First, the MOSFIRE dewar design represents a known cost with demonstrated thermal performance. Second, the dewar has a shape that minimizes deflection of the dewar walls, and is easily adapted for a fixed gravity orientation with the major axis of the dewar horizontal. Design details of the MOSFIRE dewar and internal structure may be found in the project's detailed design report ("MOSFIRE," 2007).

5.3.1.1 Dewar and Internal Structure

The MOSFIRE internal structure design is shown in Figure 6, taken from Figure 31 of the MOSFIRE detailed design report. The outer most portion of the structure is the composite support tube that provides a thermal stand-off for the instrument's internal structure. The front bulkhead (bulkhead A in the Figure) provides one of two main optical benches for mounting MOSFIRE's opto-mechanical systems. Bulkhead A is connected to a second bulkhead (bulkhead B) by a central tube and an outer support tube, these create a rigid structure that is essential to reduce flexure in MOSFIRE's variable gravity operating environment at the Keck I Cassegrain focus. Bulkhead B is the second main optical bench for MOSFIRE's opto-mechanics, and supports a continuation of the central support tube to a third smaller bulkhead where the MOSFIRE flexure control system (FCS) is mounted.

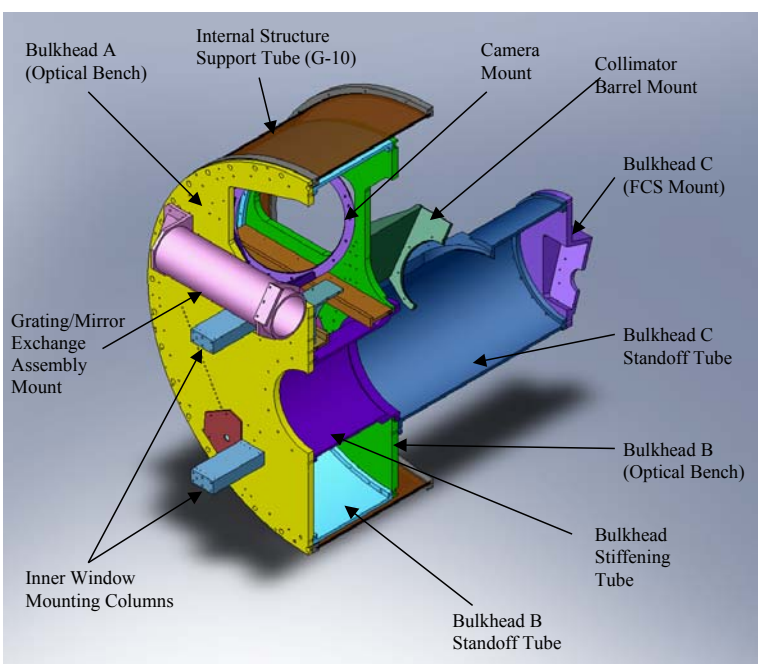

Figure 6: MOSFIRE internal structure (cross section)

The DAVINCI adaptation will eliminate the central support tube, the extension of the tube from bulkhead B, and bulkhead C. Most or all of bulkhead A will be eliminated, depending on the requirements for support of the IFS TMAs. The outer stand-off tube may need to be stiffened by additional structure to allow it to interface to the composite stand-off and support bulkhead B which will become the main optical bench for the instrument. The various other opto-mechanical support components shown in Figure 6 will be eliminated and the main optical bench layout will then be developed to match the requirements of the NGAO instrument's opto-mechanical systems.

There are some features of the MOSFIRE dewar design that are not needed. The NGAO instrument configuration will have the input light entering from a port on the side of the dewar rather than the front end cap, and the vacuum ports currently located on the front cap, which becomes the top cap, will be relocated to the rear cap. This will make the top cap a featureless dome shape. The rear cap will also be modified to eliminate the extension for the MOSFIRE FCS.

The baseline for the instrument's cryogenic cooling system will be to reuse the MOSFIRE design which employs two Brooks Automation (formerly CTI) model 1050 single stage closed cycle refrigerator (CCR) heads for cooling the dewar interior. The MOSFIRE detector is cooled by a model 350 two stage cold head, and two such cold heads will be required for the NGAO instrument. MOSFIRE is also equipped with a temperature stabilization system and uses variable speed drive for the cold heads. These features are also baselined for the NGAO instrument.

5.3.1.2 Mechanisms

The majority of the mechanisms required for the NGAO instrument can be implemented using straightforward rotary or wheel designs derived from the MOSFIRE and OSIRIS instruments. Referring to Figure 4 these include wheel mechanisms for the filters, pupil masks, and coronagraph occulting masks. The instrument's two detectors may be equipped with focus mechanisms derived from MOSFIRE's detector head assembly as well. While the AO system will maintain the focus for the instrument, there are integration and test advantages to being able to shift the detector focus, and it may be important for observing efficiency to maintain parfocality between the imager and IFS channels.

The scale changer mechanisms may also be implemented using a wheel design, but the instrument's wavefront error and pupil quality requirements may make these designs more demanding, and another design approach may have to be considered.

The pupil mask wheel will provide a selection of circular pupil masks for the near-IR passbands, as well as undersize masks for the coronagraph mode. For K band a rotating mask matched to the Keck telescope pupil is desirable to provide maximum background suppression without significant light loss.

The IFS pick-off mirror mechanism will exchange a plane mirror with a mirror having a central hole that allows light to reach the IFS. A possible design is to have an oversize mirror with a hole on one side, and rotate the mirror to translate the hole in and out of the beam. This approach would have the advantage of not disturbing the alignment of the imager optical path provided that the run-out the mechanism bearings was well controlled.

The one mechanism unique to the NGAO instrument is the grating changer. The proposed mechanism for this is a rotary turret carrying the gratings on an outer radius. Each grating can be mounted with precision adjustments to ensure proper alignment in the spectrograph. The requirements on positioning of the gratings will be demanding in order to ensure repeatability of instrument wavelength calibrations. It is likely that this motion axis will require high precision position encoding, perhaps by using either a series of LVDTs, or perhaps optical position sensing.

It should also be noted that all motors used in the mechanisms will require proper cold strapping and shielding to prevent thermal radiation into the optical path. It is expected that motors will be energized only during mechanism moves.

5.3.2 Interfaces

The mechanical interfaces between the NGAO instrument and the telescope/AO system will be simple, provided that analysis of the stability of the mounting of the instrument and the AO system to the Nasmyth platform will support the requirements for relative motion between the instrument and the AO system. This is understood to be primarily driven by the NGAO astrometry error budget.

The instrument will mount to the Keck II telescope left Nasmyth platform on kinematic mounting pads to allow adjustment of the instrument's position for alignment with the AO system's optical axis and science focal plane. The dewar will be supported by a steel tube structure that mounts to the bottom of the dewar shell's main cylinder. This corresponds to the location where the MOSFIRE dewar is mounted to the Cassegrain rotator module using an offset steel web structure.

The interface to the AO system's bench enclosure that is used to insulate the cooled bench from the dome ambient will be accomplished by a bellows. This may require insulation or be of double wall construction to ensure the integrity of the AO system's bench enclosure.

5.3.3 Electronics

DAVINCI's instrument electronics are derived directly from the MOSFIRE electronics design. A forced air cooled electronics rack will be located in the AO electronics vault and will contain all of the electronic and electrical systems required by the instrument. A block diagram of DAVINCI's electronics is shown in Figure 7.

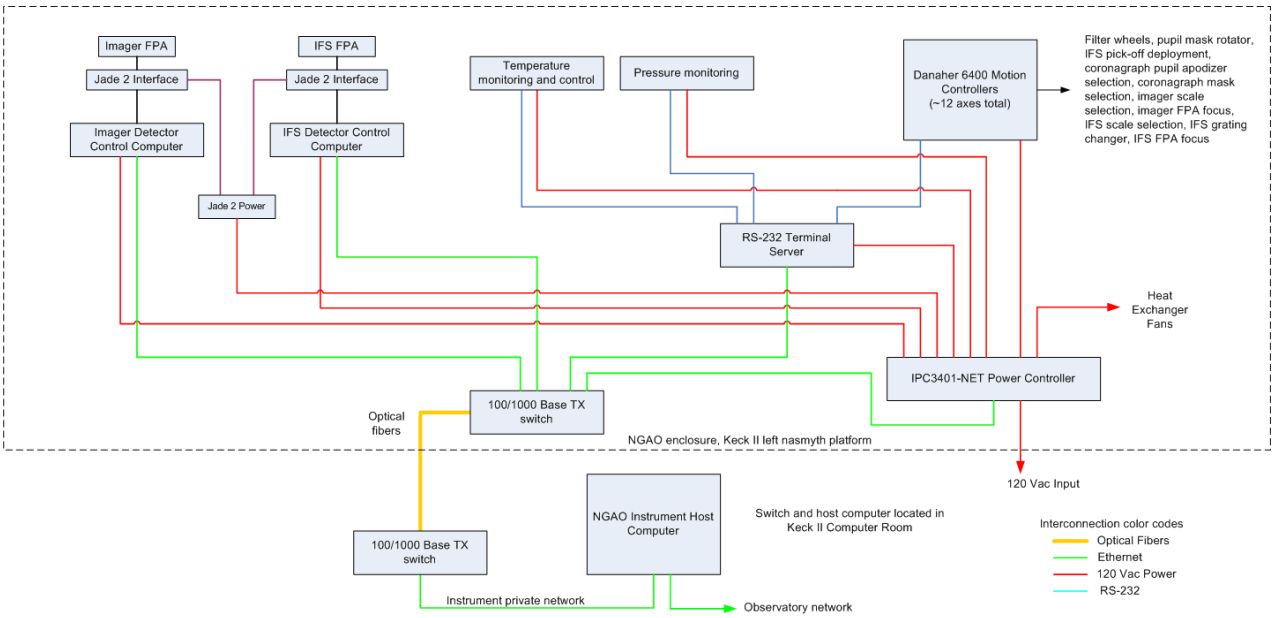

Figure 7: DAVINCI electronics block diagram

5.3.4 Software

DAVINCI's instrument software will be based on the software developed for the MOSFIRE instrument. The detector software, temperature and pressure monitoring, power controller and 6400 series motion controller software will be a straightforward port from MOSFIRE. The low level and global server architecture will also be re-used from MOSFIRE. The instrument graphical user interface (GUI) designs are TBD, but they could easily be based on a port of the MOSFIRE desktop and control GUIs.

6 OPTICAL DESIGN

6.1 Design Drivers and Choices

The concept for the DAVINCI instrument and the design of the AO system establish the following drivers for the optical design:

1. DAVINCI will function as a visible and near-IR imager with a coronagraph, and as an IFS.

2. The AO system's science relay focal plane should be inside the dewar at a location that can accommodate a wheel with a number of masks to be used in coronagraphy.

3. DAVINCI must include a selection of cold pupil masks, located at a pupil image, including a tracking pupil mask matched to the shape of the Keck telescope's primary mirror.

4. For ease in manufacturing of the masks the pupil on the cold stop should be no smaller than 25mm.

5. The imager detector will be a Hawaii 4RG with 4096 x 4096, 15 µm pixels for a detector area of 61.4 mm x 61.4mm.

6. The imager pixel scale is 8 mas, resulting in an FOV of 32.8" x 32.8" centered on the 40" FOV of the AO system's science relay.

7. The IFS should provide sampling scales of 10 mas, 35 mas, and 50 mas.

8. The mechanical package of DAVINCI, including all optics, mechanics, and detectors, should fit in a dewar based on the MOSFIRE dewar design with appropriate modifications for a fixed gravity orientation.

9. The AO system's science relay operates at f/46 and has a telecentric exit pupil.

The optical design also reflects specific choices that implement the design and build to cost requirement of NGAO. First, the three operating modes of DAVINCI share a common pupil image for placement of the cold stop or Lyot stop. Second, after the first pupil relay, an image plane will be produced in which the central 5" of the FOV are passed to the IFS. It is desirable that the imager and IFS can be used simultaneously (the imager, in this mode, is not required to see the central 5" that has been directed to the IFS).

6.2 Optical Performance Goals

Table 7 gives the optical performance goals for DAVINCI. These requirements are derived from the science drivers discussed in §5.1 and the 30 nm rms of uncorrectable (non-common path) wavefront error allocated to the science instrument in the NGAO flowdown budget.

Table 7: DAVINCI optical performance goals

Parameter	Goal	Min.	Max.	Units	Notes
Image quality					
Imager rms spot radius	≤ 1.22	-	1.22	λ x f/#	1
IFS	> 80	70	-	% ensquared energy	2
Wavefront error					
On-axis	<30	-	30	nm, rms	3
Off-axis	<60	-	60	nm, rms	4
Distortion					
Imager	< 0.25	-	0.5	%, peak to peak	5
Optical throughput					
Imager					
I band	> 60	50	-	% at 0.78 µm	6
Z band	> 70	60	-	% at 0.87 µm	6
Y band	> 70	60	-	% at 1.00 µm	6
J band	> 70	60	-	% at 1.25 µm	6
H band	> 70	60	-	% at 1.64 µm	6
K band	> 60	55	-	% at 2.2 µm	6
IFS					
I band	> 40	30	-	% at 0.78 µm	7
Z band	≥ 50	40	-	% at 0.87 µm	7
Y band	≥ 50	40	-	% at 1.00 µm	7
J band	≥ 50	40	-	% at 1.25 µm	7
H band	≥ 50	40	-	% at 1.6 µm	7
K band	> 40	40	-	% at 2.2 µm	7
Non-uniformity					
Imager	< 5	-	10	%, peak	8
IFS	< 5	-	10	%, peak	8
Instrument background					
Y-band	< 0.001	-	0.02	e^-/sec/pixel	9
J-band	< 0.001	-	0.02	e^-/sec/pixel	9
H-band	< 0.001	-	0.02	e^-/sec/pixel	9
K-band	< 0.001	-	0.02	e^-/sec/pixel	9
Ghosting					
Imager	< 10-5	-	< 10-4	-	10
IFU	< 10-5	-	< 10-4	-	10

Notes:

1. Based on the area weighted rms spot diameter over the wavelength range of 0.7 to 2.40 µm.
2. Ensquared energy in a 2 x 2 pixel box centered on the image centroid over the wavelength range of 0.7 to 2.40 µm.
3. Total on-axis rms wavefront error for the imager, total rms wavefront error for the IFS optical path to the image slicer (lenslet array).
4. Total rms wavefront error at 20" radius for the imager, total rms wavefront error at 20" radius for the IFS optical path to the image slicer (lenslet array).
5. Total geometric distortion over the entire imager FOV. The intent is to limit the instrumental contribution to astrometric error to < 0.05 mas rms for the 8 mas pixel scale.
6. Imager throughput, without coronagraph, QE of the science detector is not included.
7. IFS throughput, QE of the science detector is not included.
8. This is the peak variation in transmission over the full FOV. Flat fielding is not included.
9. This is the contribution of the instrument background to the total "dark counts"; the goal value is 10% of the goal for science detector dark current.
10. Intensity of the ghost image compared to the parent image at all wavelengths from 0.7 to 2.40 µm.

6.3 Optical Design Description

DAVINCI provides three operating modes: imager, coronagraph, and IFS. All three modes of operation are contained in a single dewar, and are fed by a single output of the second AO relay of the NGAO system. The AO relay provides a telecentric output to DAVINCI with a focal ratio of f/46. The image scale at the focal plane of the AO relay is 2.5 mm/", resulting in a 40" focal plane approximately 100 mm in diameter.

As mentioned above, it was decided that all modes of operation would share a common pupil image as a cold pupil mask or Lyot stop location, thus the first OAP relay of the instrument is shared between all modes. An optical layout of the DAVINCI instrument, including the imager light path and the integral field spectrograph scale changer, are shown in Figure 8. An annotated Zemax shaded model is shown in Figure 9 .

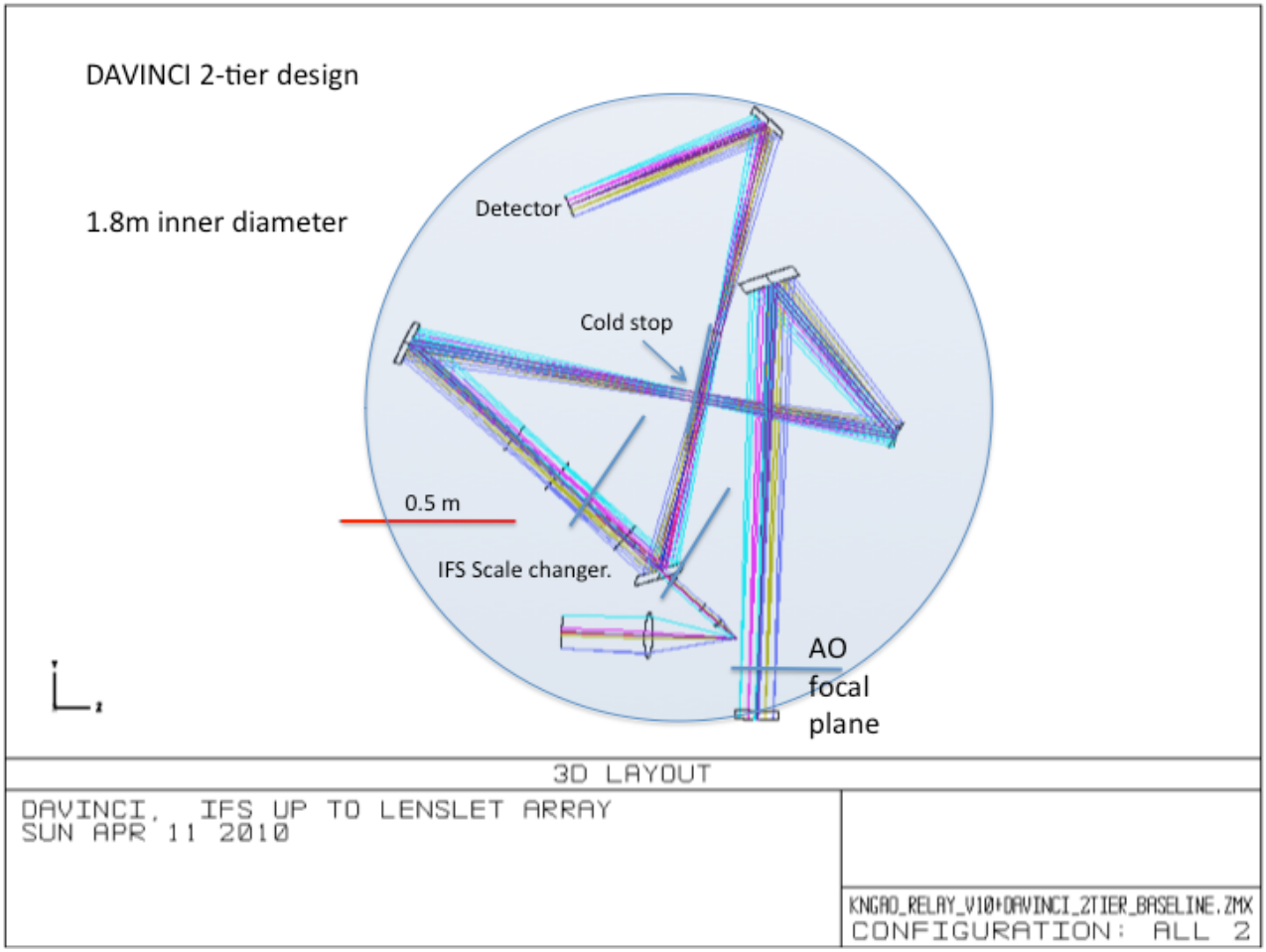

Figure 8: The DAVINCI optical layout, as seen from directly overhead

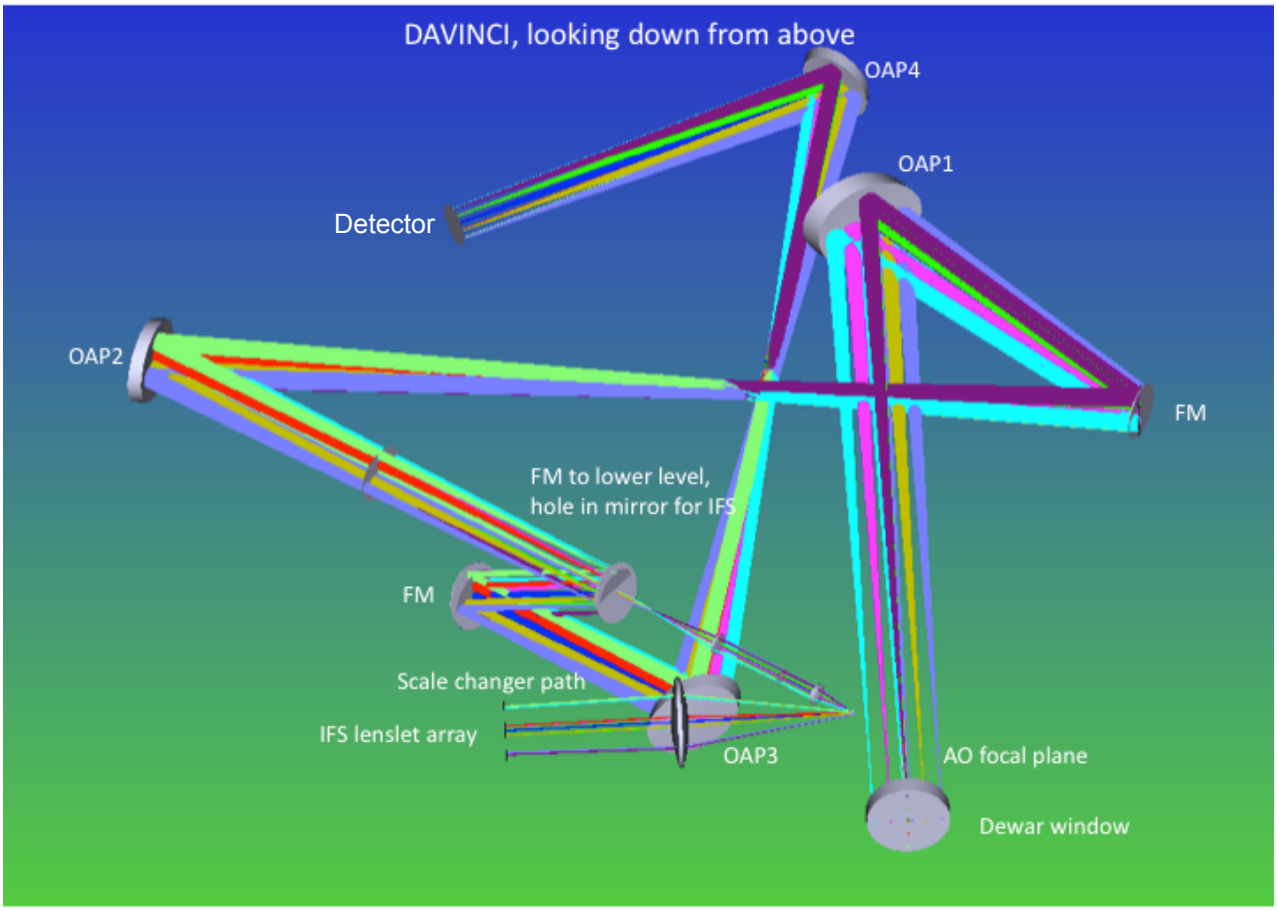

Figure 9: The DAVINCI optical layout, shown in perspective to emphasize the 2-tier design

6.3.1 Imager

The optical layout of DAVINCI's imager is illustrated in Figure 9 and Figure 10. Table 8 lists all of the optical elements in the imager with relevant dimensions. The complete optical prescription for the imager is given in appendix A.

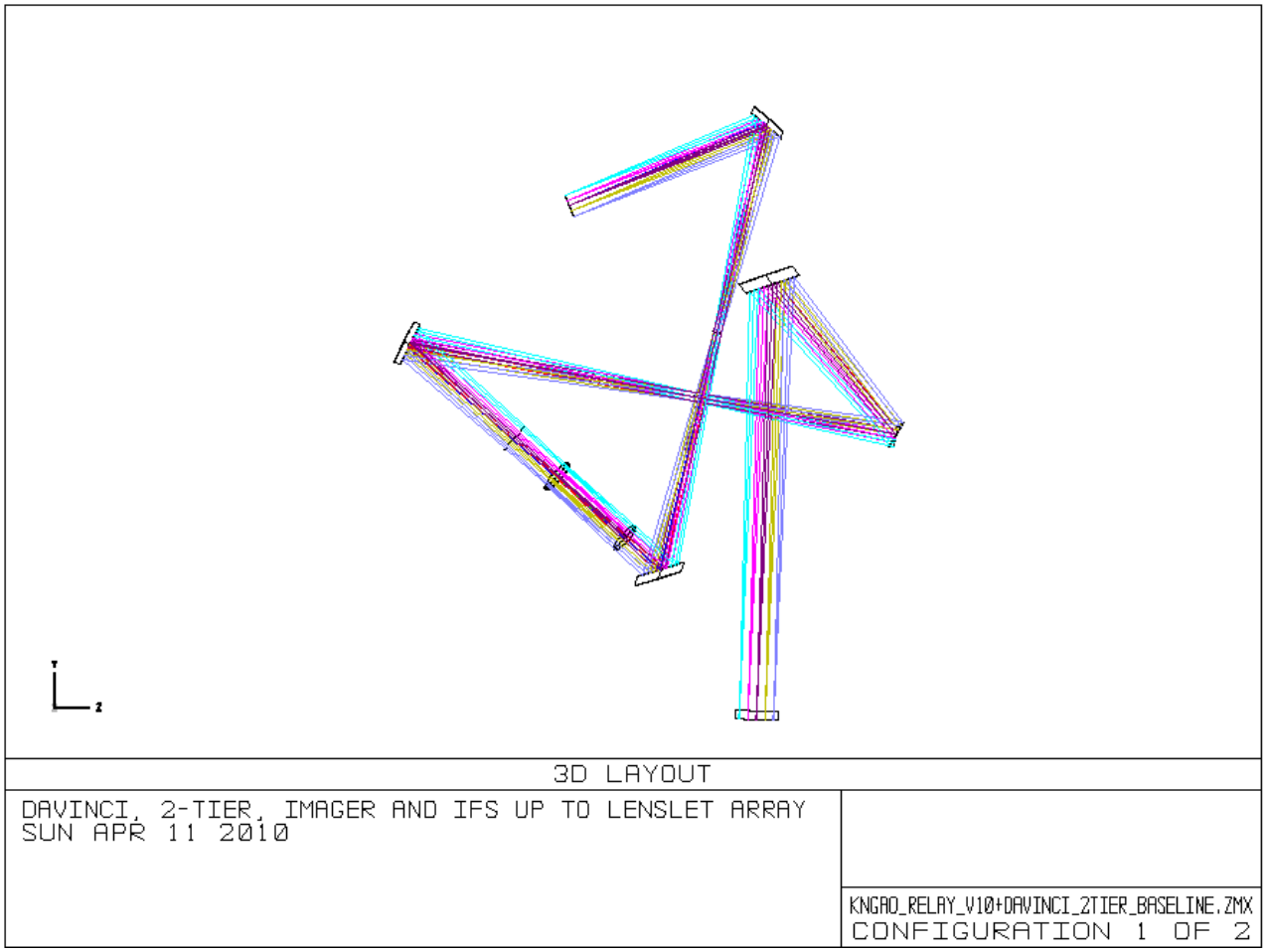

Figure 10: DAVINCI fore-optics and imager optical layout

The entrance window for the DAVINCI dewar lies in the converging beam of the AO relay's science feed, ~75mm before focus. The masks for the coronagraphic mode of the instrument are located at the AO focal plane inside the dewar.

Approximately 1 m after the focal plane is an OAP with a radius of curvature of 1998.7 mm, an off-axis angle of 41.5°, and a diameter of 150 mm. This OAP has been optimized in off-axis angle and focal length to produce a high quality, 25mm pupil image at the cold stop. This was accomplished in Zemax by producing a configuration in which the primary mirror of the telescope

was the object. Geometric rays from the primary mirror "object" were used to evaluate pupil image quality after passing through both the AO relay and DAVINCI's OAP1. OAP1 compensates for some aberrations and distortions produced in the preceding AO relay. The distance between OAP1 and OAP2 is long, almost 2 m, because of the slow input f/#, the desired 25 mm pupil size at the cold stop, and the need for telecentricity on the input to the IFS. Therefore a fold mirror is located 586 mm before the cold stop for packaging.

The 40 mm diameter bandpass filters are placed following the cold stop in collimated light.

The image scale required at the detector is about 1.54 mm/", and this corresponds to an f/29 beam. Because the optics of the DAVINCI imager must provide a scale change, OAP2's focal length is shorter than OAP1's (they are not a matched pair), giving an image scale of 1.9 mm/" at the intermediate focal plane. Because this focus also acts as the feed to the integral field spectrograph, which unfortunately requires a larger focal ratio, we chose to accomplish the focal ratio reduction for the imager with both OAP relays. OAP2 has a radius of curvature of 1531.9 mm, an off-axis angle of 31.5° and a diameter of 120 mm. It is placed one focal length away from the cold stop to provide a telecentric beam to the IFS scale changer and the second relay of the imager.

To allow access to mechanisms (coronagraph mask wheel, filter wheels, pupil mask wheel, and IFS scale changer wheels) we have divided the DAVINCI imager's optical path into two tiers, with the input optical path up to the intermediate focal plane located on an upper tier, and the optical path to the imager and detector on a lower tier. Near the image plane of the first OAP relay in DAVINCI is the first of two mirrors which fold the beam down at an incidence angle of 15° to a lower level of the dewar. A matching (15°) fold mirror completes the periscope to the second level. The vertical distance between levels is 150 mm.

To complete the scale change required by the imager's detector size, a second, also unmatched, OAP relay is used. OAP3 has a radius of curvature of 1034 mm, an off-axis angle of 61.3°, and a diameter of 120 mm. It produces a collimated beam in which a pupil image is formed one focal length away from OAP3. This pupil image is not utilized, so its quality is not relevant. The final OAP in the imaging system has a radius of curvature of 962 mm, a diameter of 100 mm, and off axis angle of 54.4°. It produces an image plane ~62mm in diameter.

Table 8: Optical element specifications for the DAVINCI imager

Optic	Diameter (mm)	Radius of curvature (mm)	Off-axis angle (degrees)	Thickness (mm)
Entrance Window	120			25
OAP1	150	1998.7	41.5	
FM1	100			
OAP2	120	1531.9	31.6	
FM2	120			
FM3	90			
OAP3	120	1034	61.3	
OAP4	100	962.1	54.4	

6.3.2 IFS Scale Changer

Figure 9, Figure 11 and Figure 12 illustrate the optical design of the IFS scale changing optics. Following the first OAP pair of DAVINCI is an intermediate focal plane, at which can be placed either a fold mirror, or a fold mirror containing an aperture at its center. This aperture allows light to enter the IFS scale changer.

The integral field spectrograph is required to work at three different sampling scales. The sampling is achieved by a 1.2 mm pitch lenslet array at the focal plane of the IFS scale changer. The scale changer is required to remain a constant length, regardless of sampling scale, to keep the lenslet array and all following optics stationary. The scale changer is also required to work at wavelengths from 0.7 μm to 2.4 μm (I through K bands). To help in meeting throughput requirements it was desirable that the scale changer contain as few elements as possible.

Table 9 provides the different sampling scales, their total field size on the 80 x 80 lenslet array, their physical size at the IFS pickoff, and the magnification required. The complete optical prescription for the scale changer is given in appendix A.

Table 9: DAVINCI IFS scale changer requirements

Sampling scale (mas)	Total field size (arcseconds)	Size at IFS pickoff focal plane (mm)	Magnification required
10	0.8	1.5	64
35	2.8	5.2	18
50	4.0	6.2	13

To achieve these disparate magnifications, two relays were used, each containing two BaF2 singlets in 4f configurations. Because we also have a wide wavelength range, separate singlet pairs were designed for the visible and infrared bandpasses. The first relay contains six pairs of interchangeable lenses, mounted in wheels, relaying the image over a constant distance but with different magnifications. The second relay has a fixed magnification for all sampling scales. See Figure 12 for the optical designs of the JHK band scale changer. All six lenses of the first relay are

shown in the Figure 12, top left (the first lens is very small, and close to the image plane), so that their relative positions can be seen. Figure 12, top right, shows the 10 mas relay, requiring the greatest magnification. Figure 12, bottom left is the 35 mas relay, and Figure 12, bottom right shows the relay requiring the least magnification, 50 mas. Notice that the final focal plane for all three relays is coincident and of identical size (96mm, or 80 lenslets multiplied by 1.2mm lenslet pitch). The visible band scale changer is almost identical with very slight differences in radii of curvature, image and object distances.

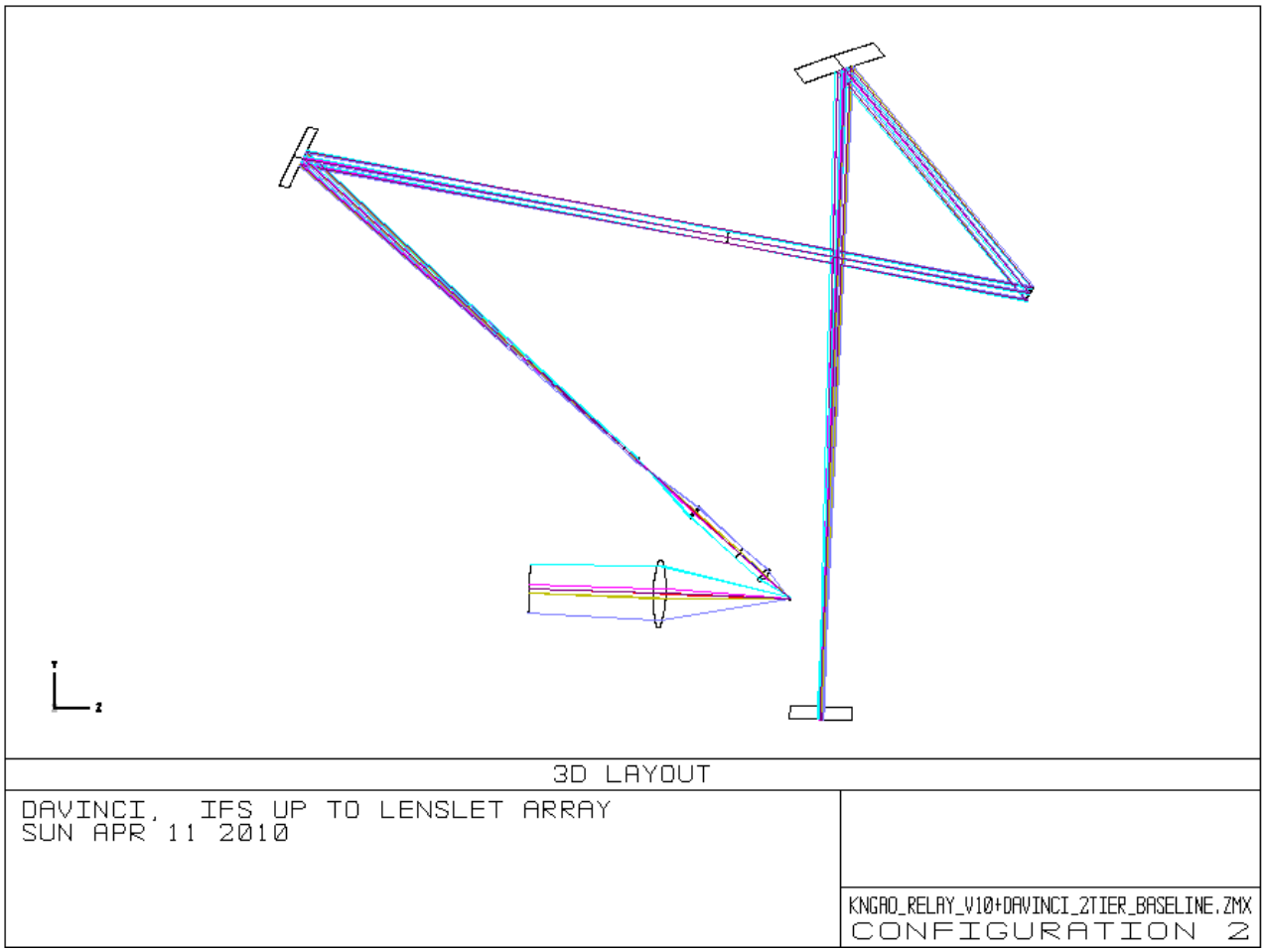

Figure 11: DAVINCI IFS fore-optics and scale changer

The scale changer contains one fold mirror between the two lenses of the fixed second relay for packaging. The total length of the scale changing optics is 930 mm. A Zemax glass file of barium fluoride tested at 120 K for MOSFIRE was included as input to the design. Unfortunately, we do not at present have index data at 120 K for wavelengths below 0.852 µm.

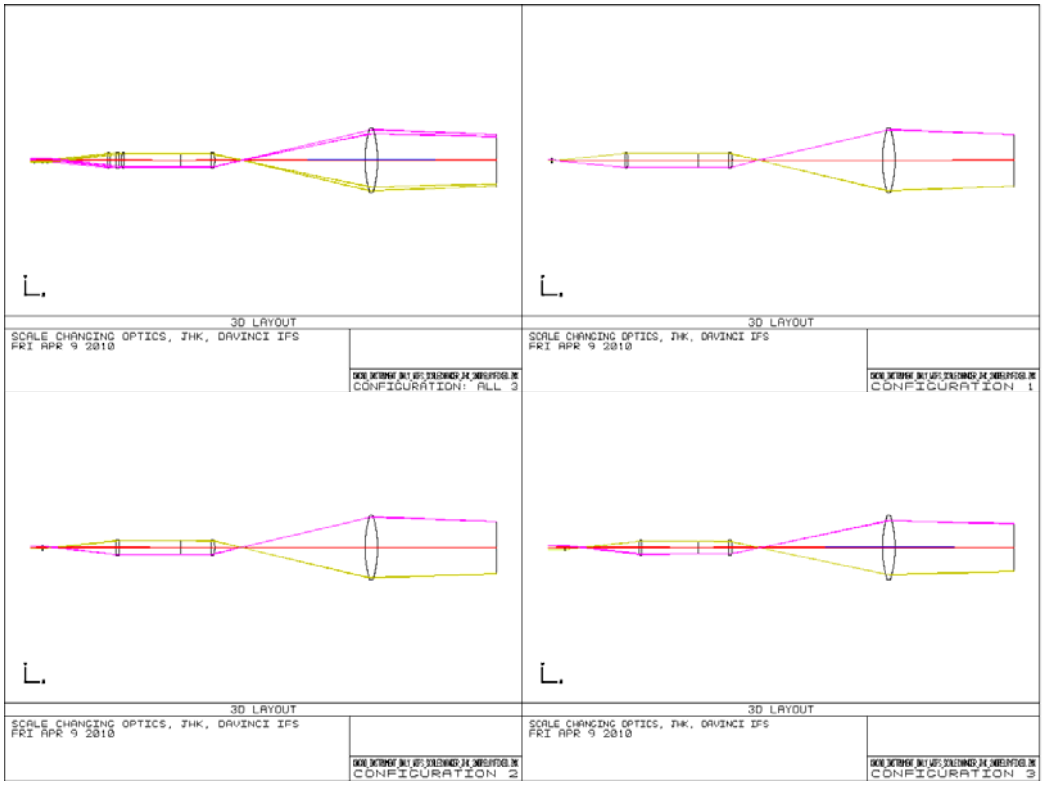

Figure 12: IFS scale changer optical layout
Clockwise from top left: All sampling scales, 10 mas, 50 mas, and 35 mas.

6.4 Design Trades

An all-refractive optical design was attempted for the DAVINCI imager, but it was found that a very large number of elements were required to reach the desired performance levels at both the pupil and image planes. This was mostly due to the large wavelength range the instrument is required to achieve. Instead, a design using all OAPs, but some with very large off-axis angle, was pursued. These off-axis angles may require special fabrication techniques, since simply cutting the OAP from a parent parabola becomes less feasible.

The spatial sampling of the integral field spectrograph will be achieved with a lenslet array having a 1.2 mm pitch to facilitate the optical design following the lenslet array. The scale changing optics would require less magnification with a smaller lenslet pitch, but the downstream optics become more cumbersome.

6.4.1 Pupil image quality

In order to maintain throughput to the detector, the pupil image at the cold stop must be of high quality. Overly aberrated pupils require undersized pupil masks, removing light from the system. The first OAP of DAVINCI was therefore designed with only the pupil image in mind. Table 10 lists the characteristics of the pupil image at the pupil mask. Figure 14 displays the results of a pupil analysis assuming the telescope mirror as the "object" and evaluating how the primary is imaged onto the cold stop plane. The geometric spots are approximately 1.6% of the size of the cold stop.

Table 10: Characteristics of the pupil image at the pupil mask

Diameter (mm)	Field considered, arcseconds	Tilt, degrees	Maximum Distortion %	Geometric spot radius (µm)
25	40	57	0.23	208

Figure 13 shows the footprint of the tilted pupil at the cold stop plane. In this case, the Zemax prescription was set up normally, with field stars at infinity as the "object". Each of the differently colored rings is the pupil edge produced by a different field point at infinite conjugate. In a highly aberrated pupil, these rings would not necessarily overlap each other.

Cancelling the pupil aberrations of the preceding OAP relays introduced a large amount of tilt at the pupil plane. The pupil masks will have to be tilted to accommodate this. The pupil quality is wavelength independent because only reflective powered optics are used to produce the pupil image.

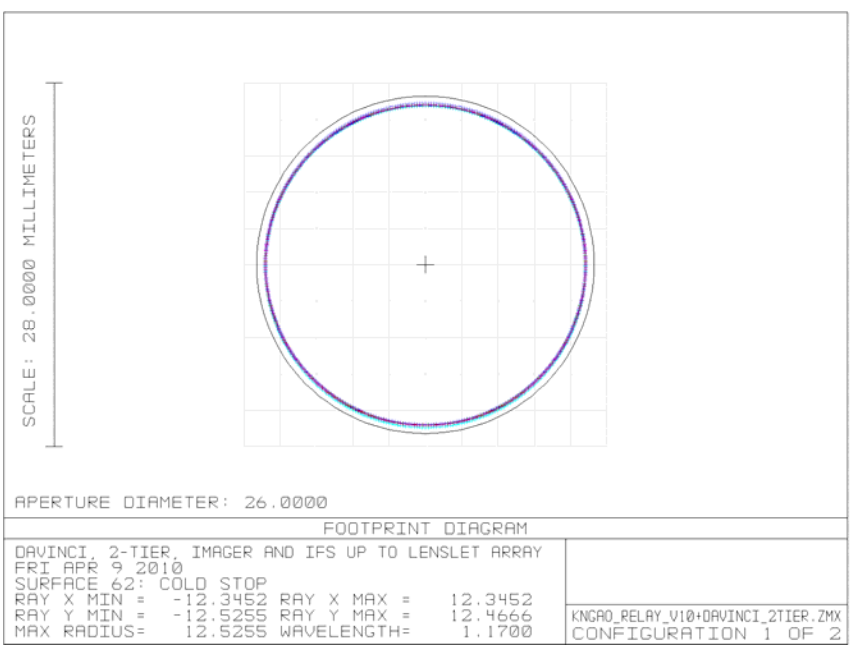

Figure 13: Pupil footprint at the tilted pupil mask

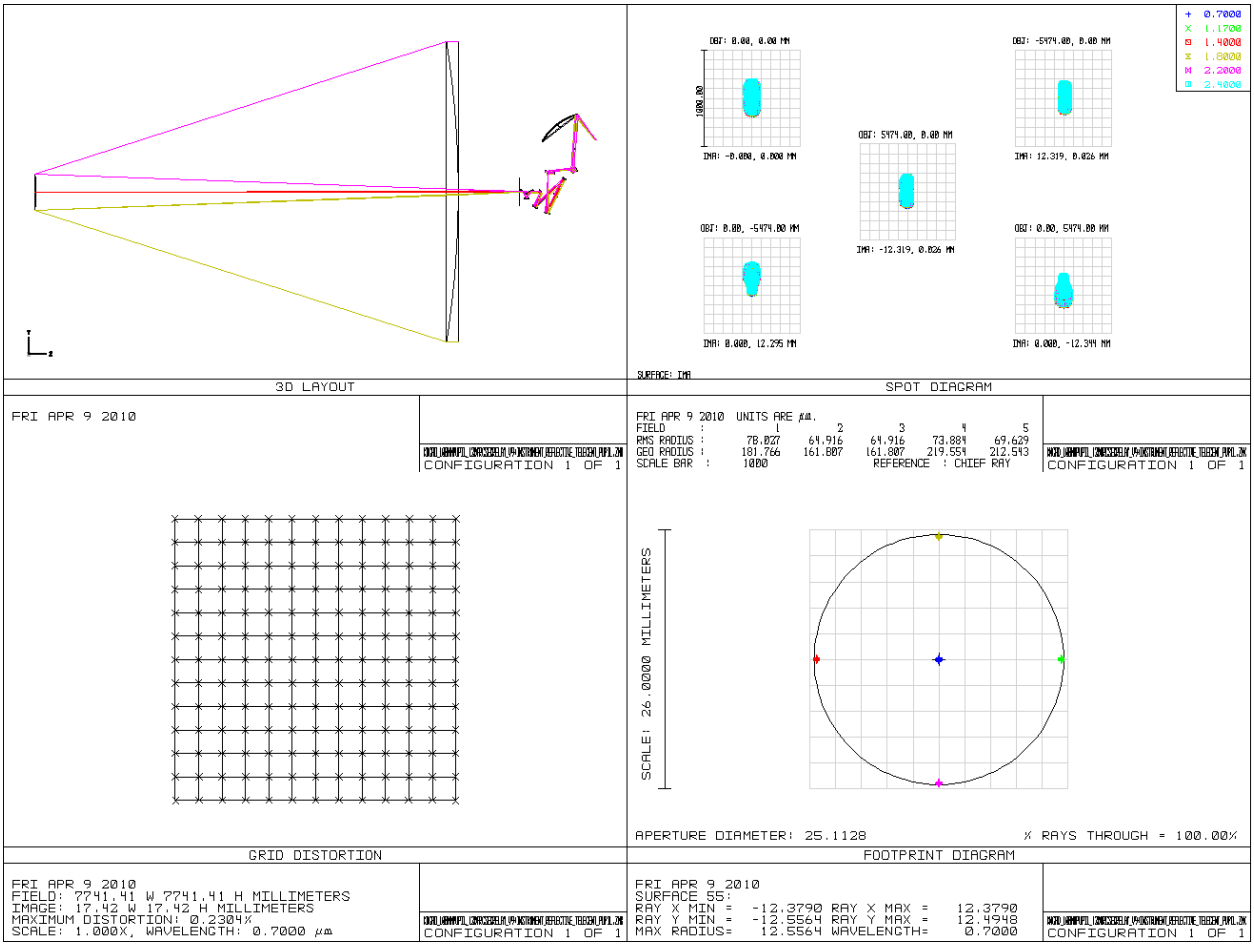

Figure 14: Characteristics of the pupil image at the pupil mask

Clockwise from top left: Zemax layout used to evaluate the pupil, geometric images of points on-axis and at edges of primary mirror(given a 40" FOV), grid distortion of the pupil image, and the footprint of the primary mirror imaged on the tilted pupil mask.

6.4.2 Image quality

The image quality of the DAVINCI imager suffers from the fact that the OAP pairs used in the instrument are not matched pairs, resulting in aberrations at extreme field points. Also, to keep distortion at acceptable levels, no attempt was made to correct field curvature at the image plane, which is the dominant source of wavefront error. On the other hand, because an entirely reflective system was designed, it suffers no color-dependent aberrations, focal shift, or lateral color. It will not require refocusing when switching to different wavelength bands. Table 11 shows the effect of adding a field flattener to the imager.

Table 11: Image quality with and without a field flattener

	FOV diameter, arcseconds	Field curvature (mm)	RMS WFE, on axis (nm)	RMS WFE, at 10 arc second radius (nm)	RMS WFE, at 20 arc second radius (nm)	Maximum grid distortion %
w/o field flattener	40	200	14	16	105	0.7
field flattener	40	0	17	9	58	5.3

A barium fluoride plano-convex singlet placed very close (~4 mm) to the focus with a radius of 75 mm on the convex surface removes the field curvature, producing diffraction-limited images at 0.7 μm across the field, but increases the maximum grid distortion to 5.3%. Smaller amounts of field curvature correction produce smaller distortion. Re-evaluating the maximum distortion requirement might be desirable to achieve diffraction-limited results at all bandpasses.

Figure 15 shows the as-built image quality without field flattening. RMS spot radii are larger than 2 pixels at the extreme field points. The system is diffraction-limited at all wavelengths for the central 20" diameter field, and diffraction-limited in K band for the entire 40" diameter field.

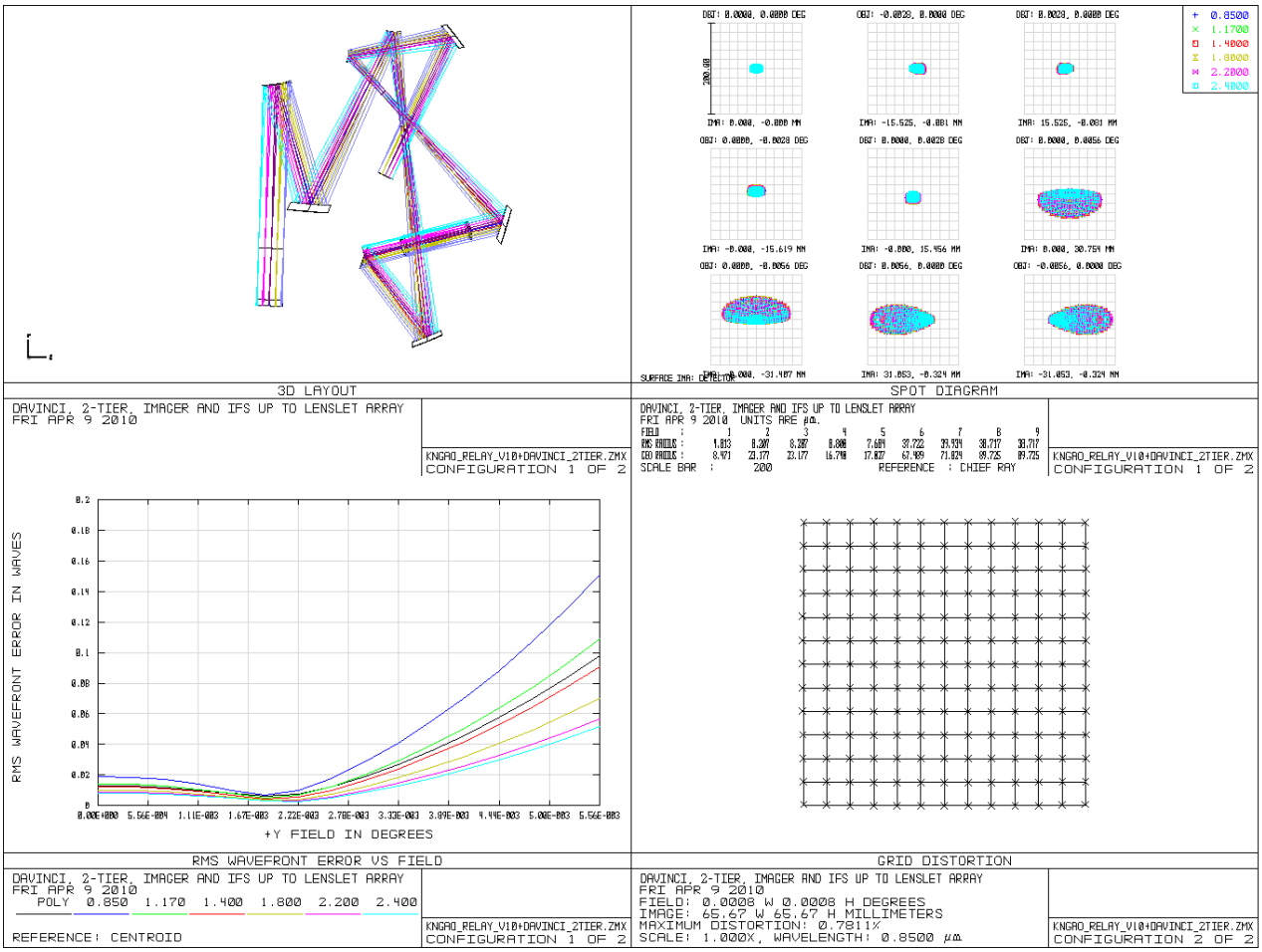

Figure 15: Image quality metrics at the DAVINCI imager's detector plane

6.4.3 Transmission

The transmissions shown in Table 12 for the DAVINCI imager were estimated using reflectance and transmittance values from the NGAO throughput and emissivity flowdown budget, version 9. It is assumed that all reflective optics are gold-coated, and all transmissive optics have a broadband AR coating

Table 12: Transmission estimates for the DAVINCI imager

Band	I	Z	J	H	K
Wavelength,μ	0.7	0.8542	1.25	1.5	2.3
Window 1	97.00%	97.00%	99.70%	99.70%	99.70%
Window 2	97.00%	97.00%	99.70%	99.70%	99.70%
OAP1	97.00%	97.00%	97.00%	97.00%	97.00%
Cold stop	100.00%	100.00%	97.00%	97.00%	97.00%
filter	90.00%	90.00%	88.00%	85.00%	95.00%
OAP2	94.59%	96.80%	98.40%	98.40%	98.70%
FM1	94.59%	96.80%	98.40%	98.40%	98.70%
OAP3	94.59%	96.80%	98.40%	98.40%	98.70%
FM2	94.59%	96.80%	98.40%	98.40%	98.70%
FM3	94.59%	96.80%	98.40%	98.40%	98.70%
OAP4	94.59%	96.80%	98.40%	98.40%	98.70%
Total	58.83%	67.58%	74.71%	72.16%	82.14%

6.4.4 Tolerances

6.4.4.1 Optical Manufacturing, Effect on Correctable and Uncorrectable WFE

An analysis of the effect of optical manufacturing errors on the total correctable and uncorrectable wavefront error has been performed for both the AO relay and the DAVINCI imager optics. Table 13 summarizes the results. Table 13 assumes manufacturing quality of $\lambda/10$ for OAPs, $\lambda/20$ for flat mirrors, and $\lambda/7$ for dichroics at the optical test wavelength of 632nm. These estimates have been obtained from optical manufacturers.

The total RMS WFE is the root sum square (RSS) of each of the elements. It is assumed that manufacturing errors follow a -2 power law in spatial frequency. The correctable wavefront error can be approximated by dividing the total RMS WFE by the square root of the number of actuators across the high order DM, in our case 64. On-axis WFE is assumed to be correctable, while the off-axis errors are not. Telescope errors, based on R. Dekany's model fit, are also included.

Table 13: Correctable and uncorrectable wavefront error due to manufacturing figure errors

Wavefront Error	# actuators	64	Test λ	6.32E-07
Correctable and Uncorrectable WFE estimates, AO Relay to Imager Detector				
λ/10 for OAPs (SORL), λ/20 for flats (Custom Scientific), λ/7 dichroics				
Static aberrations from design, WFE estimate from Zemax				40"dia. FOV
AO relay surfaces to science field	Manufacturing WFE, m	Manufacturing WfE, nm	On axis RMS WFE nm	Off axis RMS WFE, nm
AO Window 1	3.16E-08	31.6		
AO Window 2	3.16E-08	31.6		
K mirror	6.32E-08	63.2		
K mirror	6.32E-08	63.2		
K mirror	6.32E-08	63.2		
Fold	6.32E-08	63.2		
OAP1	1.26E-07	126.4		
DM1	1.26E-08	12.64		
Na dichroic science path	9.03E-08	90.28571429		
OAP2	1.26E-07	126.4		
Fold	6.32E-08	63.2		
OAP3	1.26E-07	126.4		
DM2	1.26E-08	12.64		
OAP4	1.26E-07	126.4		
IR/Vis dichroic IR path	9.03E-08	90.28571429		
DAVINCI optical path				
Window	3.16E-08	31.6		
OAP1	1.26E-07	126.4		
Fold	6.32E-08	63.2		
OAP2	1.26E-07	126.4		
Fold	6.32E-08	63.2		
Fold	6.32E-08	63.2		
OAP3	1.26E-07	126.4		
OAP4	1.26E-07	126.4		
AO relay			19.55	57.5
DAVINCI			16	105
Total (RSS) (ignoring DM print through)	4.23E-07	423.1646257	423.918038	440.4971656
total uncorrectable	5.29E-08	52.89557821	52.98975475	57.87890675
total correctable, rms		370.2690475	370.9282832	382.6182589
total correctable, PV		1282.649605	1284.933265	1325.428528
Telescope contribution, nm		79.16400043	based on R. Dekany's fit	
Total telescope + AO		430.5057948	431.2463819	447.5541217
Telescope + AO, uncorrectable		53.81322435	53.90579773	55.94426522
Telescope + AO, correctable rms		376.6925705	377.3405841	391.6098565
Telescope + AO, correctable PV		1304.901342	1307.146127	1356.576336

6.4.5 Scale changing relay for IFS

As outlined in 6.3.2, the scale changer must accommodate three different sampling scales over the wavelength range 0.7 µm to 2.4 µm. Figure 16, Figure 17, Figure 18, and Figure 19 show an analysis of the performance of the scale changing optics. Each panel contains the optical layout in top left, followed by the spot diagrams or grid distortion analyses for 10 mas sampling (top right), 35 mas sampling (bottom left), and 50 mas sampling (bottom right). The boxes in the geometric spot analyses represent the 1.2mm lenslet. Results for the entire bandpass are shown. Figure 16 and Figure 17 show the results for the optics designed to work at visible wavelengths, while Figure 18 and Figure 19 show performance for the JHK band optics.

For all sampling scales and all wavelengths, the spots remain within the 1.2mm lenslet. Distortion is only ~0.6% for all of the designs evaluated.

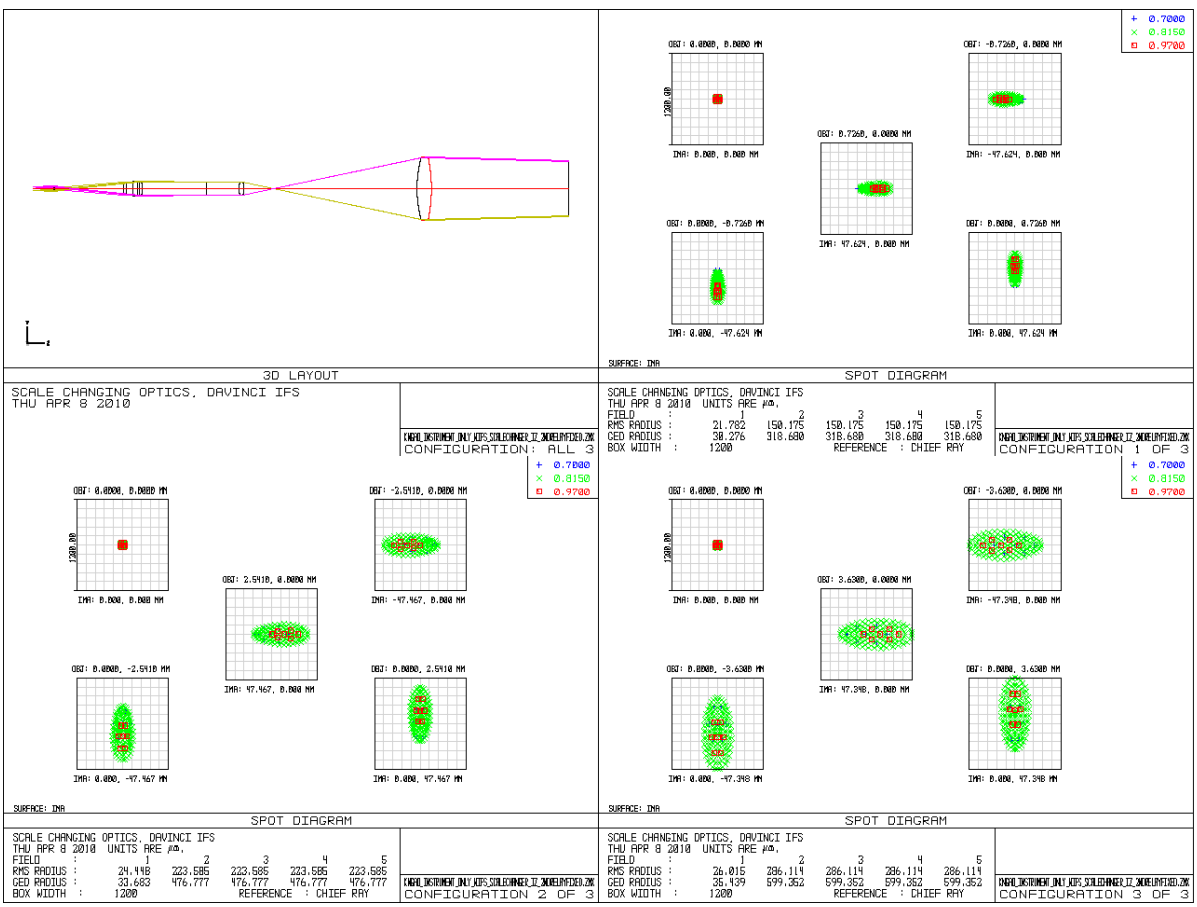

Figure 16: Geometric spot analysis of visible scale changer

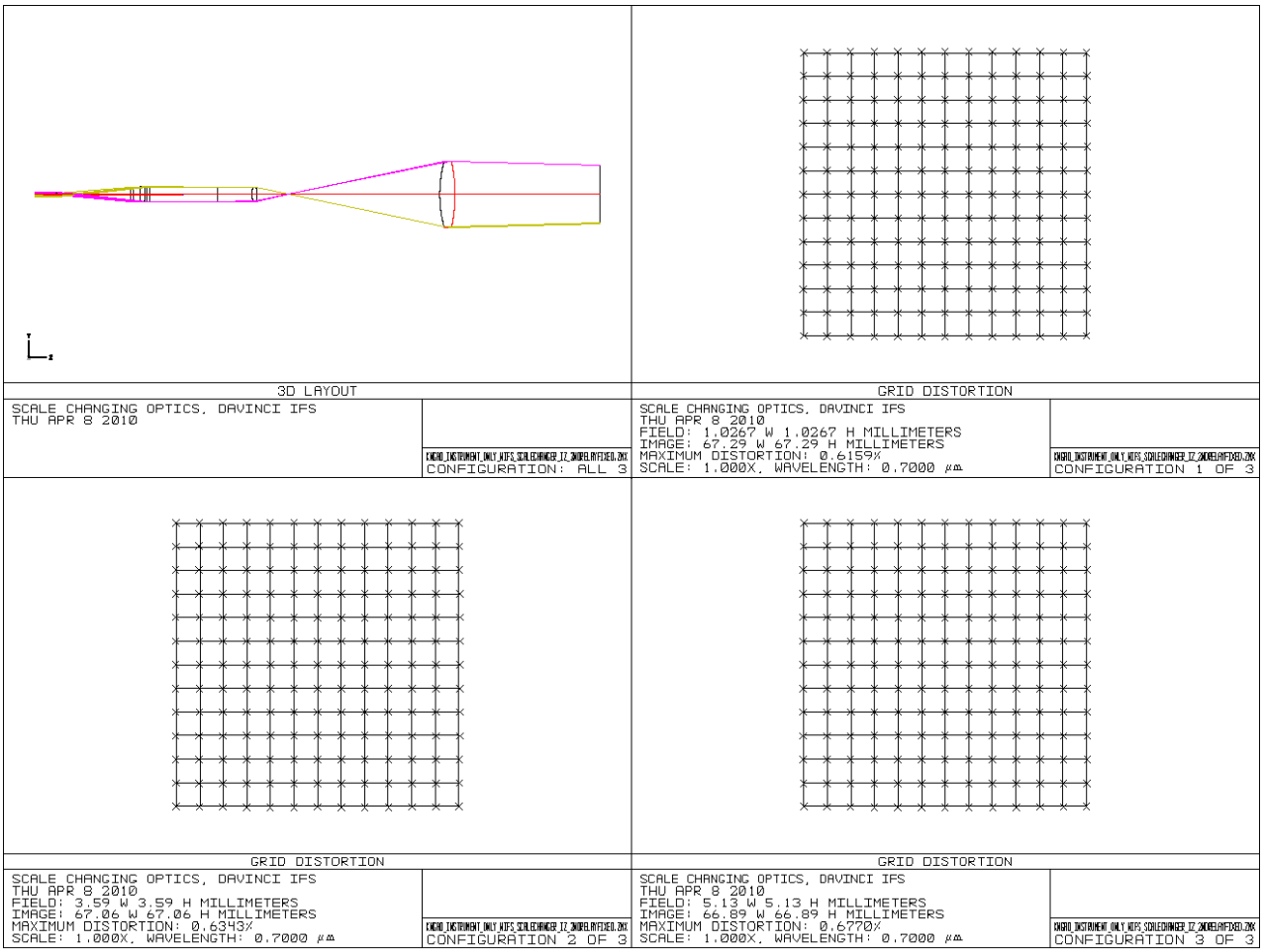

Figure 17: Grid distortion analysis for visible scale changing optics

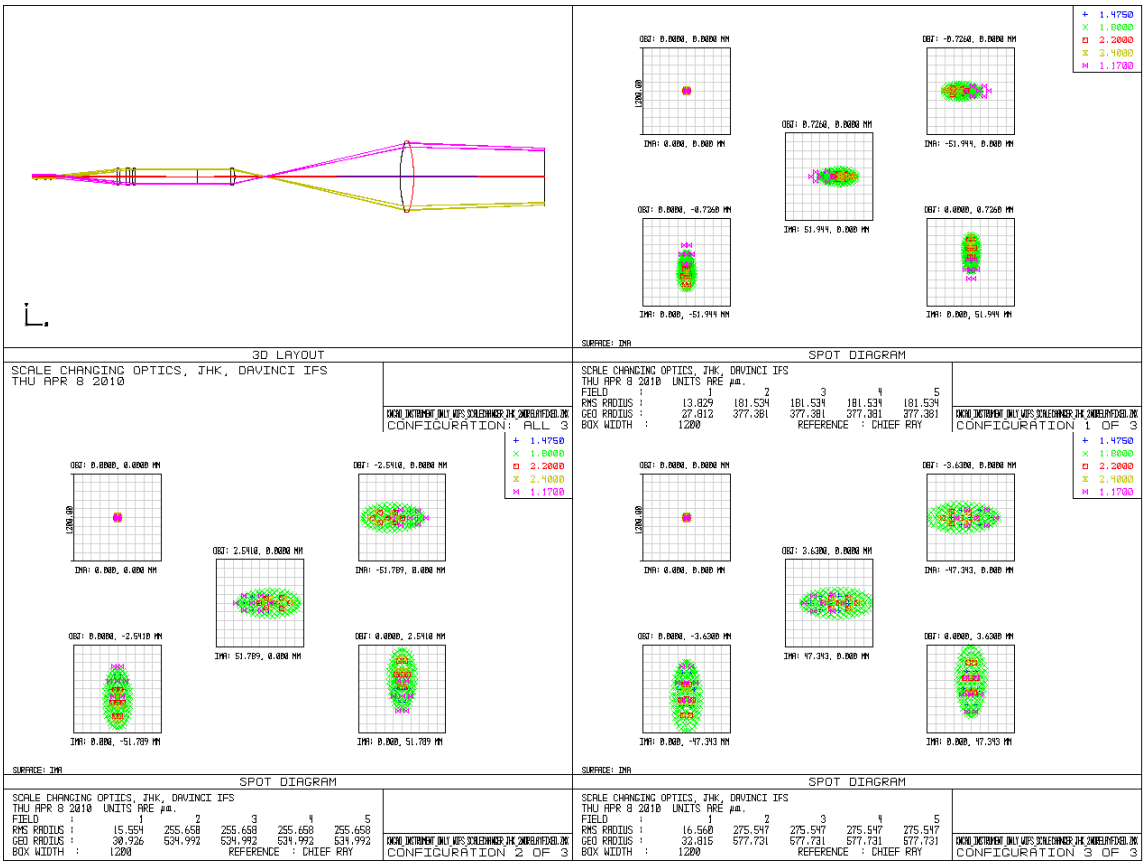

Figure 18: Geometrical spot analysis, JHK band scale changer

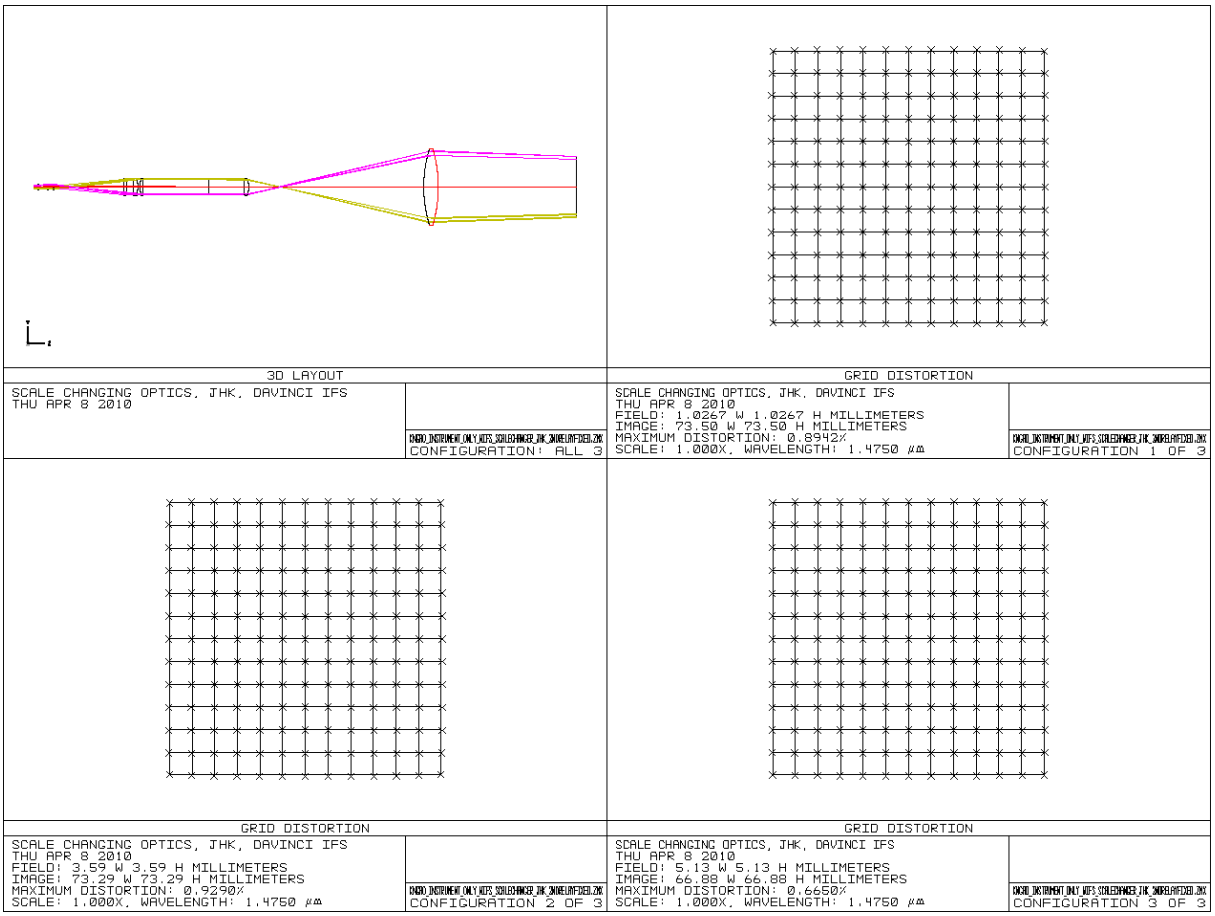

Figure 19: Grid distortion analysis, JHK-band scale changer

6.4.6 Coronagraph

DAVINCI will include a coronagraph, and our initial design is a simple Lyot coronagraph. We wanted to evaluate the performance of this approach first, but more sophisticated approaches will also be considered such as an apodized Lyot coronagraph (Soummer, 2005) or a vortex or four quadrant phase mask coronagraph. An apodizer would ideally be located exactly at a pupil plane ahead of the coronagraph mask. There is a location near a pupil plane at the second deformable mirror in the AO system, otherwise additional optics will be required to form a pupil plane for the apodizer.

6.4.6.1 Assumptions

The high contrast imaging expected performance for DAVINCI ("Keck," 2008) may be summarized as:

1. $\Delta J = 8.5$ (or contrast ratio of 4×10^{-4}) at 100 mas with a goal of $\Delta J = 11$ (4×10^{-5}) at 100 mas
2. $\Delta H = 10$ (or contrast ratio of 1×10^{-4}) at 200 mas with a goal of $\Delta H = 13$ (6.3×10^{-6}) at 1'
3. $\Delta K = 10$ (or contrast ratio of 1×10^{-4}) at 100 mas

The FOV considered for coronagraphy is only 1" therefore the field aberrations – and the pupil distortions – are negligible. We did consider a hexagonal pupil, although the shape of the aperture is not the limiting factor in the final performance.

Simulations have been done using an f/46 input beam and a Lyot stop of 25mm. We studied the performance in three observing bands, J (1.2 μm), H (1.6 μm) and K (2 μm).

Median seeing for Keck is assumed to be 0.8" and the effect of the turbulence is corrected using a square region of 62 x 62 actuators in a MEMS deformable mirror (DM). Assuming an rms wavefront error of 170 nm, the Strehl performance of the AO system for this application depends on the wavelength and is: K: 75%-82%, H: 60%, J: 40%-56%, I: 10%-22% (Dekany et al., 2009).

In theory and without aberrations, the optimum focal plane mask (FPM) depends on the wavelength, the shorter the wavelength, the smaller the FPM. However, the Strehl ratio decreases with wavelength, meaning that the halo fraction will increase leading to the need for a bigger FPM than for the perfect case. This is expected to reduce the number of different sized FPMs needed in practice.

6.4.6.2 Simulation Results

The performance of a simple Lyot coronagraph was simulated using an IDL program. The code is based on the fact that focal planes and pupil planes are related by a Fourier Transform.

The simulation is based on an f/46 beam converging onto the focal plane mask at each wavelength. The sampling resolution of the diffraction limited spot in the simulation is arbitrarily set to 12 simulation pixels per FWHM (defined as f# x λ). The pixel size in the focal plane is thus (f# x λ)/12.

The FPM is either an opaque dot or a 10% transmission dot to be able to eliminate most of the light coming from the parent star but still see the star for astrometry and photometry (some precise calibration will be needed). Such technique is being used on NICI (Chun et al., 2008).

The energy distribution in the following pupil plane or Lyot plane is the Fourier transform to get to the Lyot plane where we put an aperture to block the diffracted light from the FPM.

By the definition of the Fourier Transform, the pixel size on the pupil plane is equal to (λ x f1)/(n x θpixel), where f1 is the focal length of the first lens and θpixel the pixel size in the focal plane. We chose f1 from the f# and the diameter of the pupil in the Lyot plane (f1 = f# x d).

As stated earlier, the aberrations of the wavefront in the pupil plane are negligible because the FOV of that particular mode is very small (only 1"). Our initial simulations consider the effects of AO correction with a first approximation that considers only fitting error, using a high pass filter with a cut-off frequency set by the number of actuators. Another more accurate technique is to consider a parabolic filter instead of a Heaviside function (Sivaramakrishnan et al., 2001). The most precise estimation of the performance would be obtained by simulating true point spread functions after correction with the Keck NGAO. More thorough simulations including Strehl will be done to determine if the results found here will hold with less optimum corrections. Indeed, the Strehl in these initial simulations was kept relatively high (around 80%) which is a good approximation for K band but not for J band. We also will consider the effects of a 90% opaque FPM to account for astrometry and photometry

6.4.6.3 Results

Performance was estimated by determining the contrast obtained as a function of separation. The separation is given both in arcseconds and in cycles per aperture where one cycle per aperture is defined by the pitch of one actuator on the second DM in the AO relay.

Naturally, the results depend on the wavelength both because of the size of the spot at the focal plane and the AO correction obtained. They also depend on the size of the FPM and the size of the Lyot stop. We therefore studied contrast curves as a function of Lyot mask and FPM sizes. The goal is to define the best combination (Lyot, FPM) as a function of wavelength.

The FPM size d was varied from 2 to 12 λ/d. For the Lyot stop, only sizes bigger than 60% of the full aperture were considered because for smaller apertures, the transmitted flux goes down significantly.

The following graphs show the resulting contrast curves for the best combinations (Lyot mask, FPM), for the three different bands. A common solution was sought for the three bands in order to minimize the number of masks needed. In the following, the FPM sizes are given in λ/d. For the 3 wavelength chosen, there is a factor of 1.6 and 1.3 respectively between J and K, and between J and H. To reach the 100 mas inner working angle, an FPM equal or smaller than 5 λ/d is required for K band, 6 λ/d in H and 8λ/d in J. The Lyot mask remains the same size in all three bands. A reduction of the Lyot mask size from 90% to 75%, causes a decrease in sensitivity of 2.5 x $\mathrm{Log}(0.833^2)$ or 0.4 magnitudes.

6.4.6.3.1 J Band

For J band the Strehl is overestimated using the simple method of a Heaviside high pass filter. The requirements ask for an inner working angle smaller than 100 mas. The diffraction-limited spot is 25 mas and the maximum FPM size is thus 8λ/d diameter at 1.2 µm. For this band we varied the FPM radius from 3 to 8 λ/d by increments of 1 λ/d and the Lyot size from 75 to 90% by increments of 2.5%.

The best combination using the biggest size Lyot stop is (82.5%, 8), which is at the limit of the required separation (Figure 20). To increase the inner working angle and optimize the same FPM for a different wavelength, we need to reduce the size of the Lyot mask to 75% and use an FPM of diameter equal to 5λ/d (Figure 21). This reduces the transmission, but in this exercise the goal is to optimize the inner working angle instead of the flux. One could consider increasing the FPM to increase the Lyot stop mask and therefore increase the flux.

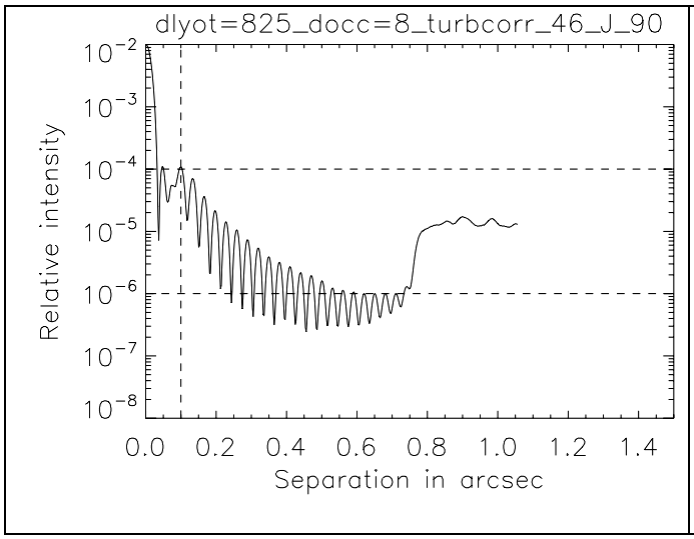

Figure 20: J band contrast (82.5%, 8) case

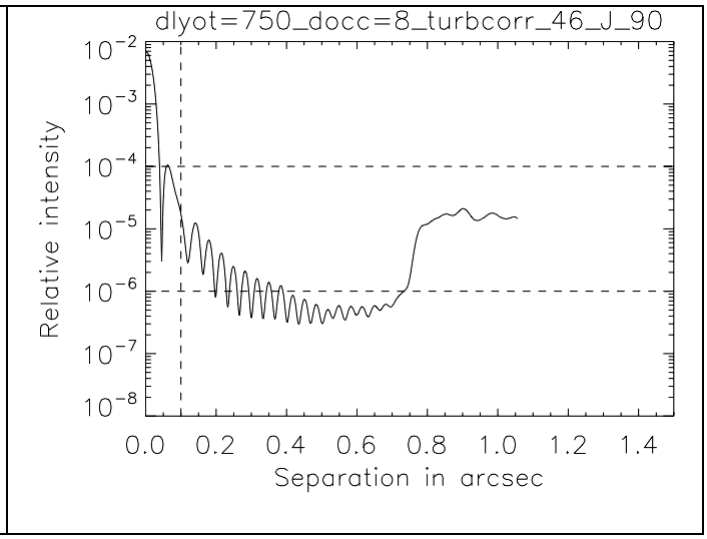

Figure 21: J band contrast (75%, 5) case

The plateau at about 0.8" is due to the limit at which the DM can control and correct the wavefront.

6.4.6.3.2 H Band

The requirements ask for an inner working angle of 200 mas. The diffraction-limited spot is equal to 33 mas and the maximum FPM size is thus 12λ/d radius at 1.6 µm. For this band we varied the FPM radius from 3 to 12 λ/d by increments of 1 λ/d and the Lyot size from 75 to 90% by increments of 2.5%.

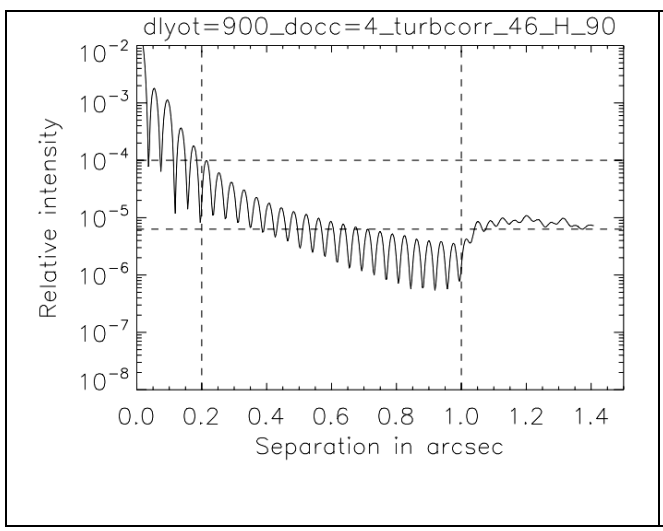

Figure 22: H band (90%, 4) case

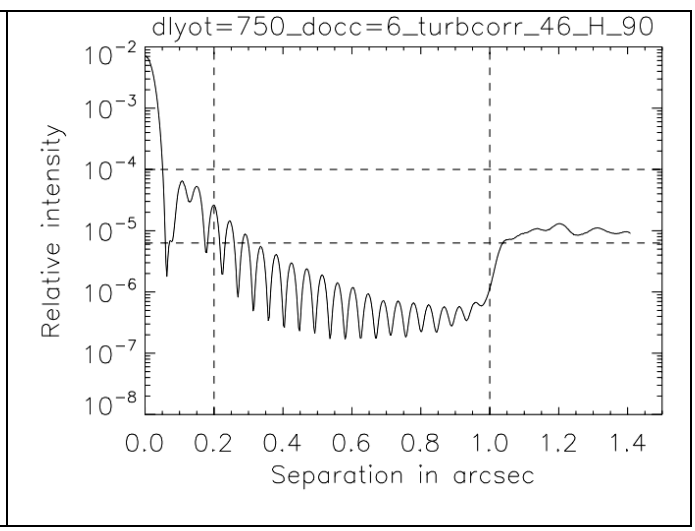

Figure 23: H band (75%, 6) case

The best combination is (90%, 4) to meet the requirements both at 200 mas and 1' (Figure 22). To minimize the changes in FPM sizes and Lyot stops between different wavelengths so far (J and H), one would have to choose the combination (75%, 6) as shown in Figure 23. The resulting contrast is even better at this wavelength.

6.4.6.3.3 K Band

The requirements ask for an inner working angle of 100 mas. The diffraction-limited spot is equal to 41 mas and the maximum FPM size is thus 5λ/d diameter at 2 µm. For this band we varied the FPM radius from 2 to 5 λ/d in increments of 1 λ/d and the Lyot size from 75 to 90% by increments of 2.5%. Because of previous results, we increased the range of the FPM size to 6λ/d.

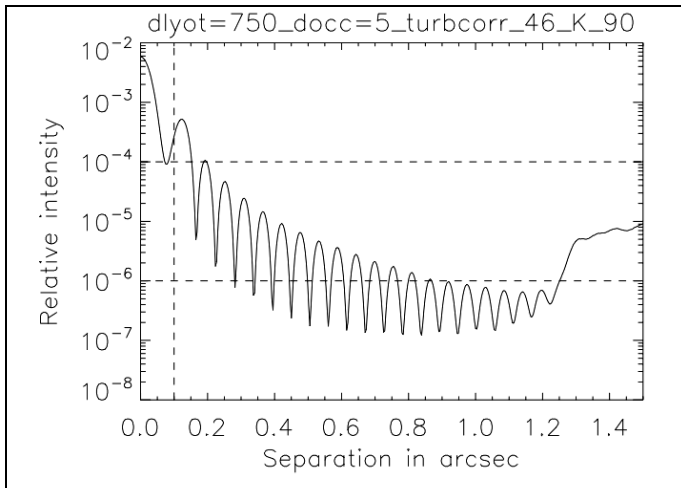

Figure 24: K band (75%, 5) case

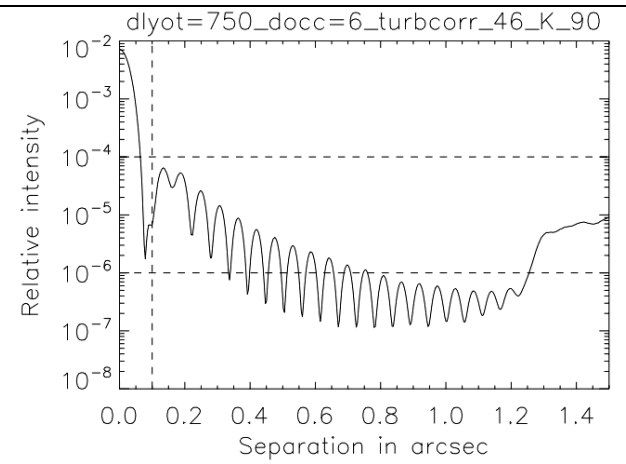

Figure 25: K band (75%, 6) case

To keep an inner working angle of 100 mas without loosing too much light, the best combination is (75%, 5) as seen in Figure 24. However, the contrast at 100 mas is higher than 10^{-4}. The combination (75%, 6) leads to better performance for a slightly bigger inner working angle (
Figure 25).

6.4.6.4 Sensitivity

The SNR vs. exposure time for companions of K band magnitudes of 18 and 24 are shown in Figure 26 for the (75%, 6) and (100%, 6) cases.

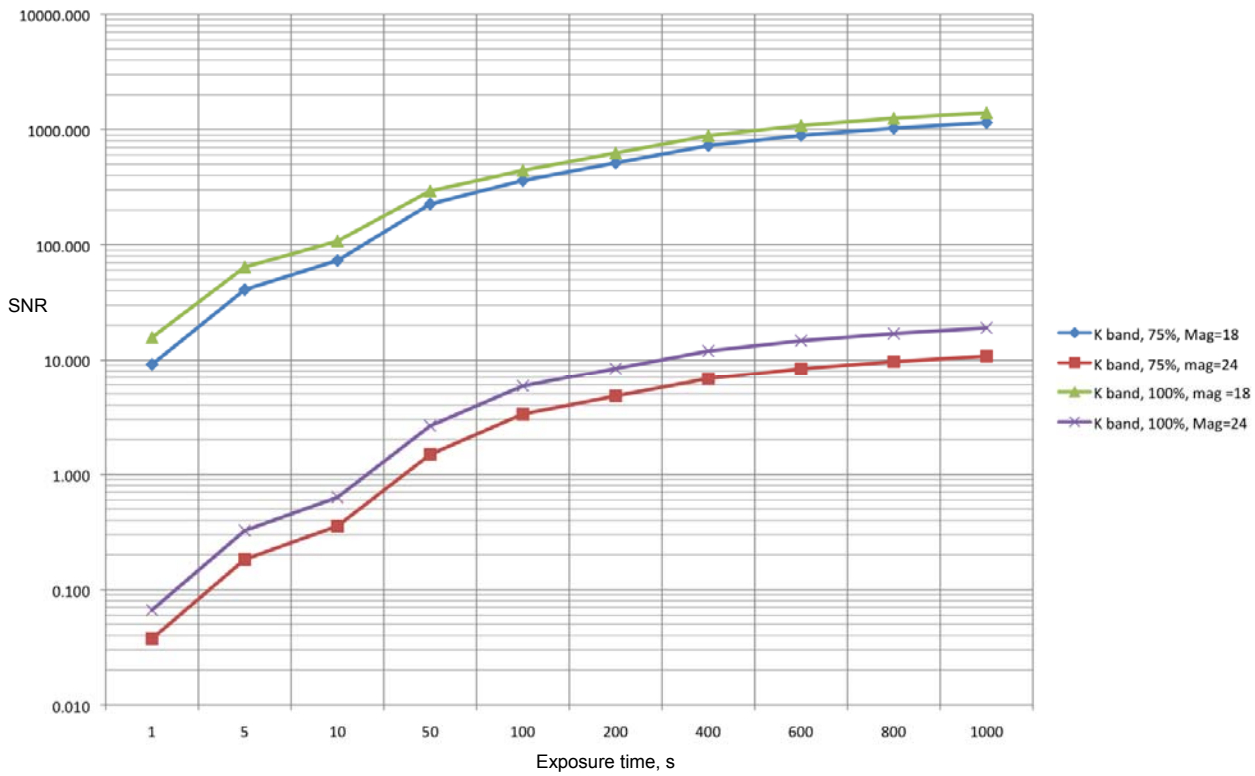

Figure 26: DAVINCI coronagraph companion sensitivity in K band

6.4.6.5 Conclusions

A simple Lyot coronagraph meets our requirements if the transmission losses and some compromises of inner working angles are acceptable. The best common combination is to use a Lyot mask of 75% the nominal pupil size and a focal plane mask of 100 mas. In order to further improve performance, we will need to use an apodizer, or consider other techniques such as a vortex coronagraph or quadrant phase masks.

6.5 DAVINCI IFS

As discussed in §0 the DAVINCI IFS requirements are driven by science where FOV and sensitivity are more important than simultaneous coverage of a single observing band. The IFS is also expected to provide spatial sampling scales suited to the diffraction limit and spatial sampling scales that optimize the ensquared energy in each spatial sample. There should be a minimum of two pixels per sample on the detector in the spatial direction, and two pixels per resolution element in the spectral or dispersion direction on the detector.

The design and build to cost requirement of NGAO leads to a concept for the DAVINCI IFS where the fore-optics (coronagraph, filters, and pupil masks) are shared with the DAVINVI imager. In order to ensure the image quality delivered to the IFS is the very highest, the IFS field is located at the center of the NGAO science relay FOV, and therefore at the center of the imager FOV. Using a pick-off mirror arrangement to send light to the IFS it is possible to image objects around the IFS field (such as PSF stars) during the IFS observation. Separate detector readout systems will provide for exposure control and readout cadences appropriate to each of the observing modes.

We have developed two concepts for the IFS, one based on a lenslet slicer similar to the OSIRIS instrument (Larkin et al., 2006), and a second concept that uses a lenslet array to perform the initial image sampling, and then reformats the array of pupil images formed by the lenslet array into a series of virtual slits.

6.5.1 IFS Design Considerations

An integral field spectrograph (IFS) instrument takes a certain, usually contiguous field of view (FOV), spatially samples the image, normally on some uniform grid, and then produces a spectrum over some wavelength range for each of the spatial samples. In the simplest form the IFS must accomplish three functions: image slicing, spectral dispersion, and detection of the dispersed spectra. Image slicing is a term used to describe the process of taking the spatial samples, effectively slicing the image into pixels, analogous to a CCD imager, but instead of becoming an intensity value each spatial pixel or “spaxel” is used to produce a spectrum. To avoid confusion with the common usage of the word pixels to mean detector pixels, the term spatial pixel or “spaxel” is often used to describe the image samples taken by an image slicer. The size of the spatial pixel determines the spatial resolution of the image formed by the image slicer output. Just as with a CCD, where each pixel exhibits a characteristic point spread function (PSF), the image slicer also has a PSF determined by the performance of the image slicer’s optical elements.

In general the design of the spectrograph portion of an IFS instrument is similar to a conventional slit spectrograph for the same wavelength range. There are three approaches to image slicing that have been used to build visible or infrared IFS instruments: fiber optics, mirrors and lenslets. The image slicer is placed at an image focal plane, often after scale changing optics which adjusts the

plate scale of the telescope to match the desired physical size of the image samples. To illustrate the basic operation of each concept, we will use a small scale example with 16 spatial samples, arranged in a 4 x 4 grid.

6.5.1.1 Lenslet Slicers

A schematic of the operation of a lenslet slicer is shown in Figure 27. Lenslet slicing (Bacon et al., 1995; Larkin et al., 2006) employs a two dimensional array of small lenses located at a focal plane to take each part of the image and focus it to a small pupil spot. The two dimensional pattern of spots effectively forms the entrance slit of a spectrograph, and the array of pupil spots is collimated and dispersed into spectra. By rotating the lenslet array slightly with respect to the dispersion axis of the grating the spectra from some number of consecutive lenslets in the column wise direction of the lenslet array will be interleaved between consecutive lenslets in the row wise direction. Increasing the rotation also allows adjacent spectra to be separated from each other, but this will decrease the number of spectra that will fit on the detector. The lenslet rotation also causes the spectra to be staggered on the detector as shown in Figure 1.

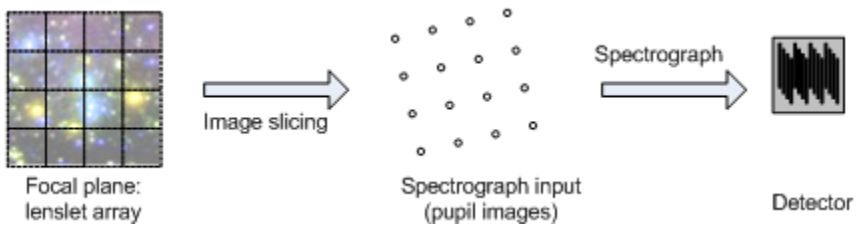

Figure 27: Lenslet slicer based IFS

Lenslet slicers have the advantage that each spatial sample is completely independent in both the spectral and spatial directions. High quality arrays of lenslets with very well matched focal lengths and nearly perfect fill factors are routinely made using specialized manufacturing techniques. The difficulty with lenslet slicing is that due to the lenslet rotation adjacent spectra are displaced with respect to each other on the detector in a pattern that repeats at the row pitch of the lenslets, this can result in bright features in one spectrum being next to fainter features in an adjacent spectrum. The displacement also leaves some of the detector area unused.

Without introducing additional optical elements, the f-number of the spectrograph collimator input is set by the need to match the f-number of the lenslet array. The combined focal lengths of the collimator and camera must match the input spatial sampling to the desired sampling on the detector (typically 2 pixels). Increasing the FOV in a lenslet slicer drives the collimator to a larger aperture and a longer focal length for a fixed f-number leading in turn to a larger aperture in the camera. The physical size of the collimator and camera apertures eventually limit the FOV of a lenslet based IFS from purely practical considerations.

6.5.1.2 Mirror Slicers

The operation of a mirror slicer is illustrated in Figure 28. Mirror slicing (Content, 1998; Eikenberry et al., 2006) employs an array of mirrors located at a focal plane to deflect portions of the image light in different directions. Each mirror is equal to the physical width of a single spatial sample in one direction, and equal to the length of n spatial samples in the other direction, where n = 4 for the example of 4 x 4 spatial sampling shown in Figure 2. The light from each slicing mirror is collected by a second set of mirrors that format the slices into one or more rows in a virtual slit for the spectrograph. Flat or powered mirrors may be employed, and additional mirrors or lenses may be needed to place the pupil image at the correct conjugate in the spectrograph optical path.

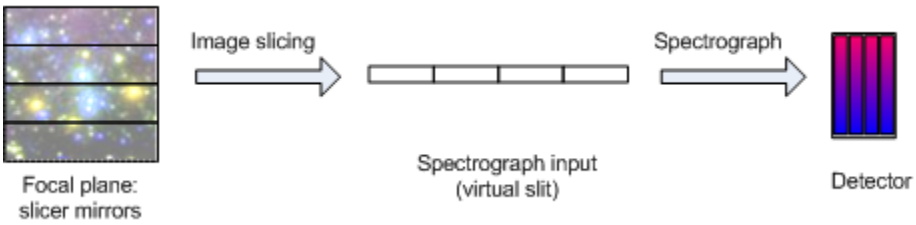

Figure 28: Mirror slicer based IFS

Mirror slicers have the advantage that the virtual slit approach can be more efficient in the use of the detector pixels. The disadvantages are greater light losses and additional sources of aberrations that can impact the quality of the spatial sampling. Light is lost at the input focal plane due the fact that the tilted mirrors move through focus, causing some light to be lost at each end of the long axis of each spatial sample. The mirrors are relatively small, typically between 0.3 and 0.5 mm in the narrow dimension. The mirrors only separate the samples in one dimension, so aberrations of the slicer mirror surfaces, as well as the aberrations through the spectrograph all contribute to loss of wavefront quality in the spatial direction. In a mirror slicer design the aperture of the collimator is set by the virtual slit length, and ultimately the total slit length will be limited by the practical size of the slicer and collimator, and the related down stream focal ratio and grating size considerations.

6.5.1.3 Hybrid Slicer Design

Comparing the lenslet based slicer, and the mirror slicer, one notes two important considerations. First, for slicers operating at the diffraction limit, the higher quality of the sampling in both spatial dimensions is a benefit. Second, the mirror slicer avoids the problem of the staggered spectra and the problems of bright feature/dark feature cross talk between adjacent spectra, and provides more consistent pixel to wavelength calibration for spatial samples along a given virtual slit, and makes more efficient use of detector pixels.

The technology for making lenslet arrays is capable of producing very precise arrays with high fill factors (≥ 97%), very low transmission losses, excellent focal length matching and very low wavefront error. With a proper choice of focal length the lenslet array can produce very clean

samples of the focal plane image, and spatial sampling is not degraded by the optical performance of the spectrograph. After considering an initial evaluation of the feasibility of a given FOV using either a mirror slicer or a lenslet array we have realized that a combined system might offer the best combination of low wavefront error and efficient detector utilization. A "straw man" design for this approach is shown in Figure 29.

In this hybrid design the lenslet array forms a series of pupils that are then reformatted by a slicer stack and a series of pupil mirrors into rows of virtual slits at the entrance of the spectrograph. This design has the advantage of maintaining the well isolated spatial samples of the lenslet array design all the way to the detector and avoids the problem of overlap between staggered spectra on the detector.

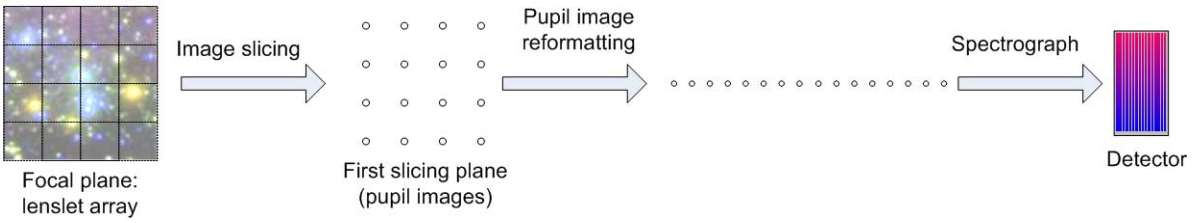

Figure 29: Hybrid slicer based IFS

A hybrid slicer will require a greater distance between the pupil image plane and the lenslet array to allow for mirrors to redirect columns of pupil images to the formatting optics. However, the lenslet focal length is not constrained by the need to achieve a small pupil image size in order to fit the desired number of lenslet images between the row pitch that results from rotation of the lenslet array.

6.5.2 IFS Optical Design

The overall arrangement proposed for the IFS is shown in the lower center of Figure 4. A pick-off mirror located near the intermediate focus sends the central portion of the beam to the IFS scale changer, and in turn to the IFS.

The current design for this pickoff system exchanges a plane mirror that sends all of the light to the DAVINCI imager with one that has a central hole 5" in diameter, allowing light from the center of the field to reach the IFS while permitting simultaneous imaging of the rest of the field by the imager. By moving only this mirror the centering of the IFS field on the imager should be able to be reliably maintained, allowing an initial imager observation of the full field to be used to refine the telescope pointing prior to beginning the observation. This image can also be used to identify, and compensate for, any shift in the field sent to the imager when the plane mirror is exchanged with the one having the central hole. Another possible variation is to have a third mirror with a

partially silvered central area, allowing the central object to be used for PSF imaging at the same time as an IFS observation.

As noted earlier, there are two concepts for the IFS image slicer, a lenslet slicer, and the hybrid slicer. The lenslet slicer employs a 16 mm x 16 mm lenslet array, while the hybrid slicer, requiring greater spacing between lenslet pupil images to allow for the reformatting optics, uses a 96 mm x 96 mm lenslet array. The IFS scale changing optics described in §6.4.5 are for the hybrid slicer, this is the more demanding application for the scale changer design, and it is the one that we have focused on at this point in the design process.

6.5.2.1 Lenslet Slicer

The baseline configuration for the IFS employs a lenslet based image slicer similar to the OSIRIS instrument. The initial analysis presented in the following paragraphs was developed with reference to OSIRIS optical design notes (OODN0300 and OODN0400 by James Larkin). The lenslet array is located at the focus of the scale changer and forms a pupil image from each spatial sample that in turn becomes the effective entrance slit of the spectrograph. The lenslet array is rotated with respect to the spectrograph causing successive lenslets column wise to produce adjacent, staggered spectra on the detector. By choosing a rotation such that 24 such spectra are produced for each row wise step across the lenslet array, the 4096 pixel wide Hawaii-4RG detector will accommodate 80 to 85 row wise steps. In the other dimension a total of 4 rows of staggered spectra can be accommodated with ~1024 pixels per spectrum for a total of 85 x 96 spectra on the detector. The 1024 pixels per spectrum imply that narrow band filters are used to limit the length of each spectrum.

An 80 x 80 lenslet array with a pitch of 200 µm results in a total area of 16 mm x 16 mm for the lenslet array. This is the same size as the OSIRIS lenslet array but with a smaller lenslet pitch. The lenslet array is rotated with respect to the spectrograph to produce 24 staggered spectra corresponding to 24 columns of lenslets (compared to 16 in OSIRIS). With a 50 mas spatial scale an 80 x 80 lenslet array will result in an FOV of 4".

The pupil size at the spectrograph based on 200 µm pitch lenslets and 24 spatial samples (lenslet columns) in the space of one lenslet pitch (1/24 stagger) is 8.3 µm for the 50 mas plate scale. The f-number of the lenslets is 3.4, and the collimator should match this f-number. With a larger detector (Hawaii-4RG) the spectrograph camera will require a somewhat larger field size (~1.6 times on each axis), but the required f-number is only 11 based on a 16 mm x 16 mm lenslet array and 15 µm detector pixels.

The focal length of the collimator will be determined by requirements to illuminate the proper area on the grating, and the combined focal length of the collimator and camera will be selected to ensure that the spectra are properly imaged on the detector. The baseline concept is to use a

different grating for each of the instrument's passbands. For efficiency the gratings will be chosen to operate close to the blaze condition ($\alpha - \theta B = \beta - \theta B$).

6.5.2.2 Hybrid Slicer

The hybrid slicer design uses the same 80 x 80 spatial sample configuration used with the lenslet slicer. Figure 30 shows how the hybrid slicer reformats consecutive rows of the lenslet array into 8 virtual slits of 800 spatial samples each. As discussed later in this section we have also considered an arrangement that uses 6 virtual slits with 1066 samples each.

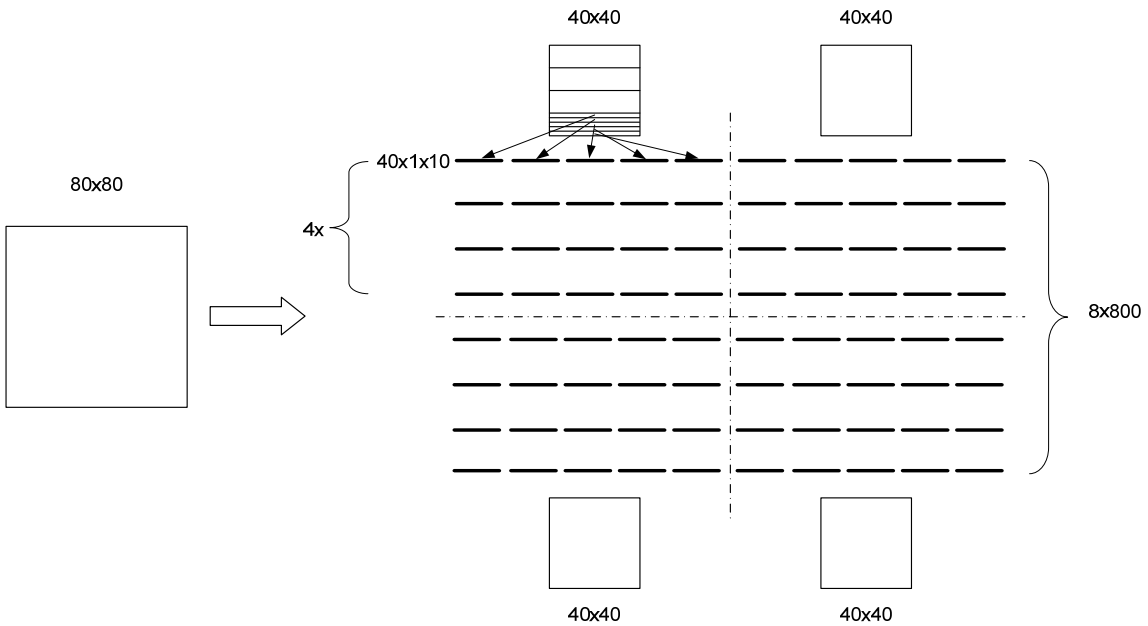

Figure 30: Reformatting the 80 x 80 sample pupil plane into 8 pseudo-slits

The 80 x 80 lenslet array is divided into four 40 x 40 sub-fields with the division in the y direction accomplished by a field splitting mirror, and the subdivision in the x direction accomplished by two separate reformatting mirror paths. Figure 31 shows the optical layout of the hybrid slicer. Note that this optical layout shows the scale changing optics after the lenslet array that are required to expand the field to the size needed to allow for the space required between lenslet images to allow the slicer optics to function properly. In the scale changer design discussed in §6.3.2 the entire field magnification required to match the field to the 80 x 80 lenslet array is accomplished prior to the lenslet array. This increases the size of the lenslet array but reduces the size of the hybrid slicer optical path.

As shown in Figure 31 the lenslet array creates a pupil plane that is split into two fields by a 45° field splitting mirror and then delivered to the reformatting mirrors by a second 45° fold mirror. This arrangement provides the space needed for the reformatting mirrors.

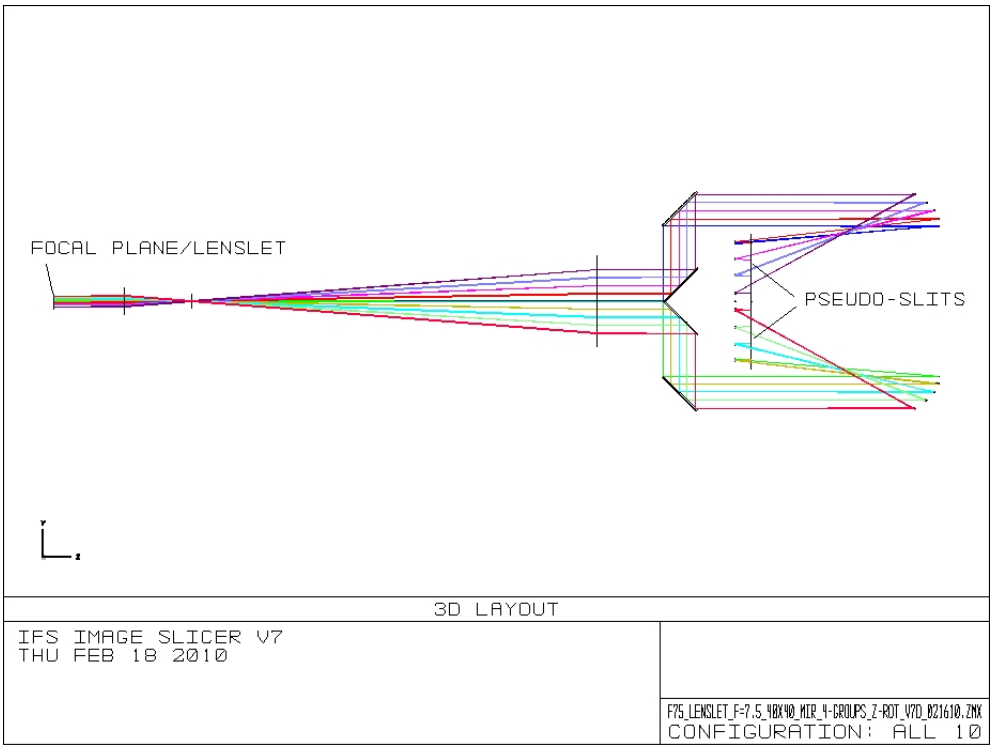

Figure 31: Optical layout of the hybrid slicer

After the field splitting mirror there are two sets of slicer mirrors which reformat the lenslet array pupils into virtual slits. Each subfield covers one quadrant of the pupil plane with 40x40 samples. From this point we describe the optical design of the slicing optics for one sub-field only. The slicing optics for the other three sub-fields are identical to the optics of the first sub-field and located symmetrically about the Z-axis. All four sub-fields converge at the slit plane. At the slit plane each of the square sub-fields is reformatted into one half of each of 4 virtual slits. Reformatting a 40x40 subfield into a set of pseudo-slits is achieved by using two sets of slicing mirrors as shown in Figure 32.

A first set of slicing mirrors (M1) is arranged in four groups. Each group consists of 10 rectangular mirrors (1.22 mm x 48 mm) with spherical front surfaces (R = 562 mm). It reformats a 40x10 sample rectangular field into a 1*400 sample staggered row. The second set of spherical mirrors (M2, R = 45 mm) rearranges this staggered row into a single straight row at a slit plane.

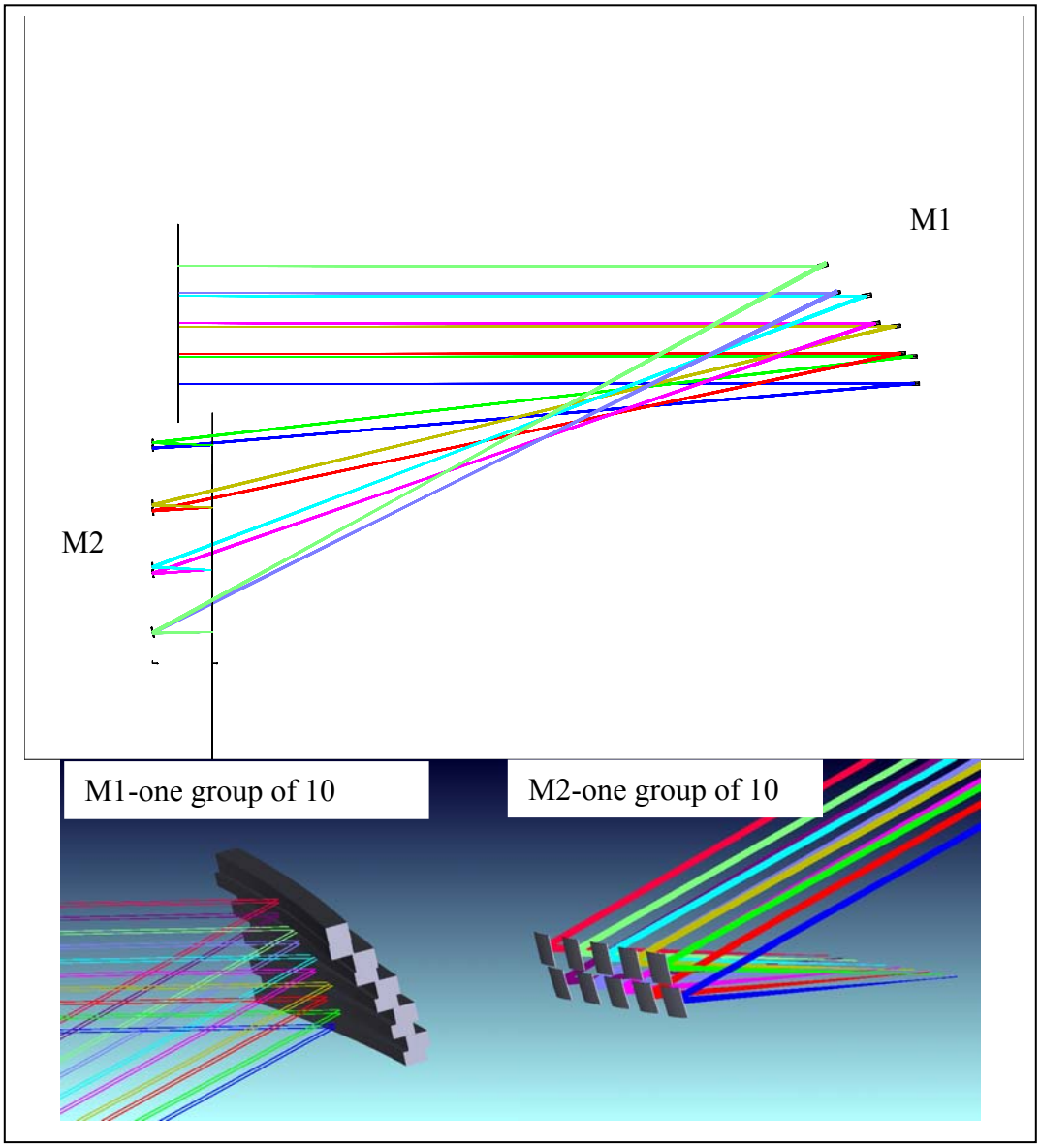

Figure 32: Slicing mirrors
The first set of slicing mirrors (M1) reformats the square field into a staggered line. The second set of mirrors (M2) rearranges the staggered line into a single line. For clarity only top and bottom mirrors in the M1 group are shown in the upper picture.

In the image slicer, a row of pupil images from a single 80 lenslet row is transformed from 16mm to 96mm (6x) at M1 and to a 7.7 mm sub-slit (1/12.5x) at the slit plane. These sub-slits are separated by 1.1 mm gaps in order to evenly distribute the slit length (spatial direction) along 2048

pixels of the detector. The total length of the slits is 101 mm, and the resulting field at the slit plane is 101 mm x 202 mm.

6.5.2.2.1 Hybrid Slicer Optical Layout

The slicing mirrors not only reformat the lenslet array sub-field but also provide the following optical functions:

1. De-magnification of the field by 12.5x to achieve a reasonable size for the pseudo-slits. M1 and M2 are separated by F1+F2 distance preserving the telecentricity at the slit plane.

2. Collimate the beams in the M1 to M2 space. This is achieved by placing M1 at one focal distance from the intermediate focal plane. This helps to keep the beam footprint small at M2.

Each group of M1 mirrors arranges the beams into a single staggered row. Figure 32 shows that the M1 mirrors in the group #4 (the farthest from the center line) point to a row of M2 mirrors that is the closest to the center line. This seems counterintuitive because such a layout results in steep angles of incidence at M1 and M2 for this group. This layout was adopted in order to eliminate vignetting between the M1 mirrors in two adjacent groups.

6.5.2.2.2 Hybrid Slicer Optical Performance

In this section we describe the performance of the IFS reformatting optics. The effect of the DAVINCI fore-optics and scale changer is not included. The lenslet elements are modeled as 0.2 mm diameter and 7.5 mm focal length lenses made of BK7. In the model described here a paraxial collimating lens and a camera lens provide required image scaling at the detector. We assume a detector with a 15 µm pixel size and a required scale of 2 pixels per spectra in the spatial direction (50 mas spatial sampling at the AO focal plane). This will require [15um*2/(200um*6/12.5] = 0.3 magnification for re-imaging the slit plane by the IFS optics in order to map the rectangular field onto 2048 x 4096 detector pixels.

Figure 33 shows the worst spot size for each group of 10 mirrors in any of the subfields. Note that the spot size for each sample is determined by a set of pupil images (the detector is at an image of the pupil plane). The square box size in the figure is 30 microns (2 pixels) in size. There are only 5 fields shown representing beams at the center of each sample field and at four edges. The geometric radius of the full field spot diagram gives an estimate of the size of the sample image at the detector.

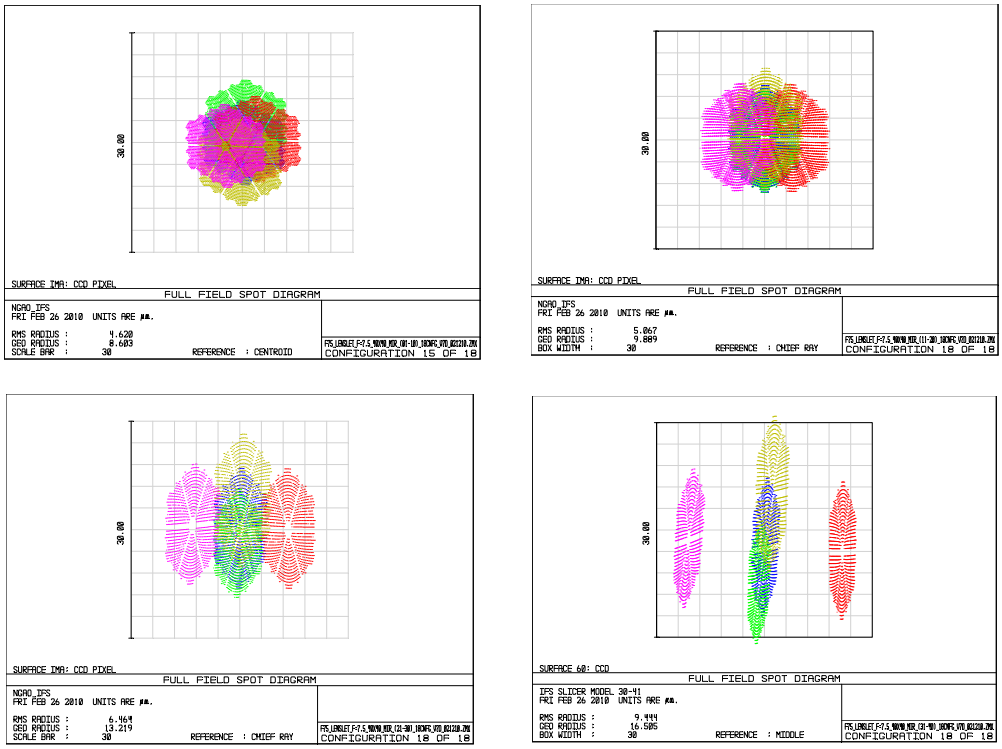

Figure 33: Pupil images at detector (for λ = 1.5 µm).
The box size is 30 µm (2 pixels). The worst case for each of four groups of slicing mirrors is shown. Five field points are shown for each sampling lens. The geometrical radius provides the best estimation for the image size of a single sample at the detector.

The worst spot sizes for four groups of the slicing mirrors are:

Group 1: geometric radius = 8.6 µm
Group 2: geometric radius = 10.0 µm
Group 3: geometric radius = 13.2 µm
Group 4: geometric radius = 16.5 µm

Note that the x axis in Figure 33 corresponds to the spatial sampling direction at the detector. As expected, the worst image quality is for the images from group 4 due to the steep angles of incidence at the spherical mirrors.

6.5.2.2.3 Distortion

There is another aberration that affects the image quality at the detector. This one resembles distortion because the effect appears as a curvature in the spectral direction in a row of pupil images. Again this effect gets bigger with an increasing incidence angle. Figure 34 shows this curvature for four sub-slits located at the edge of the field.

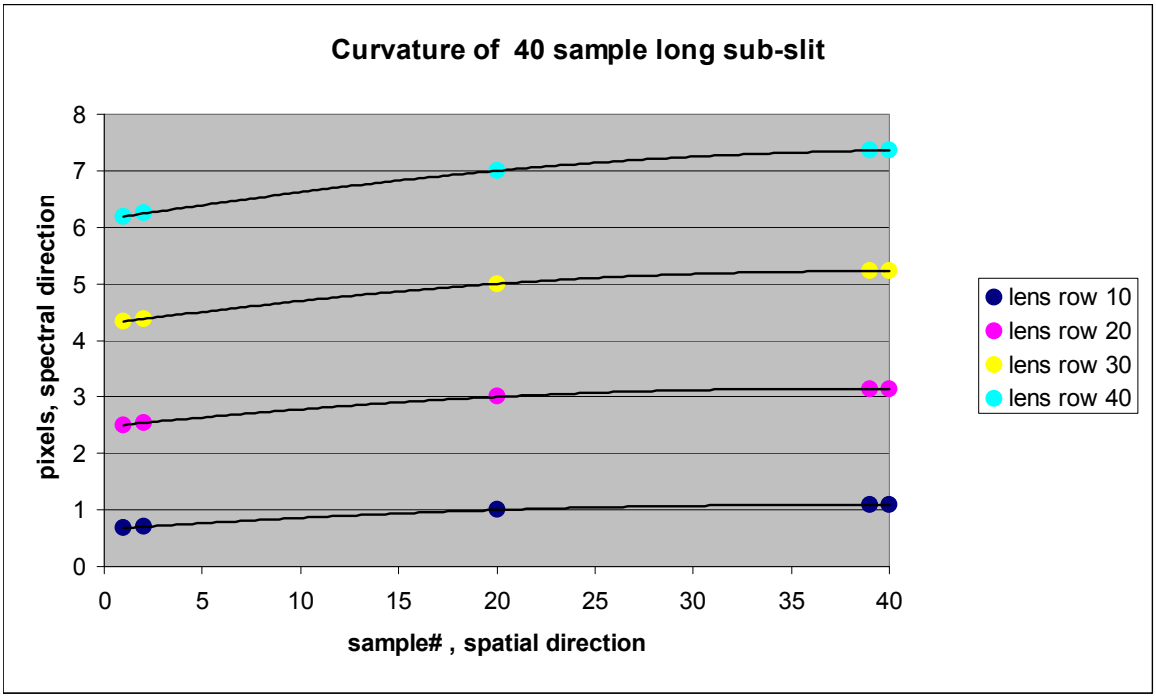

Figure 34: Curvature of single sub-slit in spectral direction.
Four sub-slits at field edge are shown.

This curvature results in an image shift in the spectral direction by almost 1 pixel at the end of a sub-slit, the worst case for a sub-slit from the group 4. The end result is a small overlap between spectra from slit #1, for example, and spectra from slit #2 because there is a difference in the curvature for adjacent slits. This problem will be addressed as the design is further developed.

6.5.2.2.4 Tolerances

Table 14 provides tolerances for the mirror surface with respect to a reference surface for each slice in both slicers. The reference surface may be a mounting surface of a mirror. This will depend on the type of manufacturing (conventional polishing or diamond turning).

Table 14: Tolerances for optical surface position in both slicing mirrors

Slicer 1 (M1)	**plus/minus**
M1 Tx	4'
M1 Ty	2.5'
M1 Dx,Dy	0.05 mm
M1 Dz	0.1 mm
Radius	0.6 mm
Slicer 2 (M2)	
M2 Tx	1.3'
M2 Ty	1.4'
M2 Dx,Dy	0.017 mm
M2 Dz	0.05 mm
Radius	0.05 mm

The positioning tolerances shown in Table 14 were obtained by running a Zemax tolerancing procedure with a merit function set to a +/- 0.25 pixel allowable image shift at the detector. The tolerances are tight and we have obtained quotes showing that they can be met by more than one manufacturer.

6.5.2.2.5 Surface roughness

Surface roughness of mirrors in the image slicers may become an issue if we select diamond turning as a method of manufacturing. The surface roughness may result in throughput losses and an increase in the background. To obtain a tolerance for surface roughness, we can use the well known formula for total integrated scatter given by

$$TIS = (\frac{4\pi\sigma}{\lambda})^2, \sigma << \lambda;$$

where σ is the roughness and λ is wavelength.

Scattering off the M1 slicer will have a negligible effect on the background because of the direction of scatter (Figure 32). Scattering off the M2 slicer will produce two effects. For a roughness tolerance of 8 nm, we calculated the effects shown in Table 15.

Table 15: Scattering as a function of wavelength

Wavelength, microns	0.7	1.2	2.4
TIS,%	2.1%	0.7%	0.2%
Fraction of TIS reaching detector	6.3%	6.3%	6.3%

For the background evaluation we assumed an f/2 spectrograph collimator and a Lambertian bi-directional reflectance distribution function (BDRF). The latter assumption is very rough but BRDF can be evaluated more accurately only by measurements. The total TIS gives a maximal

scatter contribution to the background for the case when the whole scatter will occur in the angle of acceptance of the collimator.

Note that a typical roughness tolerance for precision conventional polishing is 2 nm. For diamond turned parts the manufactures claim typical roughness from 3 nm to 8 nm.

6.5.2.2.6 Hybrid Slicer and IFS Transmission

For the image slicer design with all reflective components coated with bare gold the total transmission is 95% in the J, H, and K bands. The end to end predicted transmission of the DAVINCI IFS is shown in Table 16 when the hybrid slicer combined with the DAVINVI fore-optics and a three mirror anastigmat (TMA) is used for the collimator and the camera.

Surface	I band	Z band	Y band	J band	H band	K band	I band	Z band	Y band	J band	H band	K band
Dewar Window												
Infrasil 302, 25 mm thick	99.23%	99.23%	99.23%	99.23%	99.23%	99.23%						
Coating, 2 surfaces	97.83%	97.84%	94.95%	95.83%	95.50%	96.77%						
Coronagraph Mask												
Infrasil 302, 2 mm thick												
Coating, 2 surfaces												
FM1							97.65%	98.53%	98.79%	99.00%	99.03%	99.17%
OAP1							97.65%	98.53%	98.79%	99.00%	99.03%	99.17%
Cold stop	100.00%	100.00%	92.00%	92.00%	98.00%	98.00%						
Filter	90.00%	90.00%	80.00%	88.00%	85.00%	95.00%						
OAP2							97.65%	98.53%	98.79%	99.00%	99.03%	99.17%
Scale changer	84.93%	84.93%	84.93%	84.93%	84.93%	84.93%						
Lenslet	95.00%	95.00%	95.00%	95.00%	95.00%	95.00%						
Reformatter							91.26%	93.75%	94.47%	95.07%	95.18%	95.58%
Collimator TMA												
1							97.65%	98.53%	98.79%	99.00%	99.03%	99.17%
2							97.65%	98.53%	98.79%	99.00%	99.03%	99.17%
3							97.65%	98.53%	98.79%	99.00%	99.03%	99.17%
Grating							60.00%	60.00%	60.00%	60.00%	60.00%	60.00%
Camera TMA												
1							97.65%	98.53%	98.79%	99.00%	99.03%	99.17%
2							97.65%	98.53%	98.79%	99.00%	99.03%	99.17%
3							97.65%	98.53%	98.79%	99.00%	99.03%	99.17%
%T	70.49%	70.50%	55.95%	62.12%	63.69%	72.13%						
%R							44.22%	49.25%	50.78%	52.09%	52.31%	53.20%
Combined	31.17%	34.72%	28.41%	32.35%	33.32%	38.38%						

Table 16: DAVINCI IFS transmission estimate

6.5.3 DAVINCI IFS Passbands

The DAVINCI IFS passbands each cover ~5% of each of the major spectral bands, I, Z, Y, J, H, and K in order to limit the length of the spectrum from each spatial sample and allow more spatial samples to fit on the detector, allowing a larger FOV. Table 17 shows the initial DAVINCI IFS passbands.

Table 17: IFS passbands

Passband	Narrowband 1			Narrowband 2			Narrowband 3			Narrowband 4		
	Cut-on	Cut-off	CWL	Cut-on	Cut-off	CWL	Cut-on	Cut-off	CWL	Cut-on	Cut-off	CWL
Ia, Ib	700.0	776.5	738.25	776.5	853	814.75						
Za, Zb	855.0	952.5	903.75	952.5	1050	1001.3						
Ya, Yb	970.0	1045	1007.5	1045	1120	1082.5						
Ja, Jb, Jc	1100.0	1200	1150	1200	1300	1250	1300	1400	1350			
Ha, Hb, Hc, Hd	1475.0	1563	1518.8	1563	1650	1606.3	1650	1738	1693.8	1738	1825	1781.3
Ka, Kb, Kc, Kd	2000.0	2100	2050	2100	2200	2150	2200	2300	2250	2300	2400	2350

6.5.4 DAVINCI IFS Spectral Formats

The science requirements for the DAVINCI IFS indicate that a spectral resolution of $3000 \leq R \leq 4000$ is required to resolve OH lines and support kinematic measurements. Two virtual slit configurations for the hybrid slicer are under consideration, one with 8 virtual slits with 20 sub-slits each (mapping 80 x 80 spatial samples into 20 x 40 x 8) and 6 virtual slits with 28 sub-slits each (mapping 82 x 82 samples in to 28 x 40 x 6).

Each sub-band listed in Table 17 will be selected by combination of a bandpass filter and the rotation angle of the diffraction grating. We want to evenly distribute 8 or 6 spectra along 4096 pixels utilizing as many pixels as possible for each spectrum. For a given spacing between the virtual slits, there are three parameters that affect this distribution. They are diffraction grating dispersion, angle of constant deviation (between a beam incident at the diffraction grating and a diffracted beam) and the effective focal length of camera optics. As a baseline for selecting diffraction gratings we can use Table 18 which lists the maximal grove frequency to fit a sub-band spectrum in either 512 pixels or 683 pixels (for 8 or 6 slits).

Table 18: Baseline for groove frequency G (1/mm)

# of slits	Ia	Ib	Za	Zb	Ya	Yb	Ja	Jb	Jc	Ha	Hb	Hc	Hd	Ka	Kb	Kc	Kd
8	636	636	499	499	649	649	486	486	486	556	556	556	556	486	486	486	486
6	848	848	665	665	865	865	649	649	649	741	741	741	741	649	649	649	649

We will use G numbers from the Newport Richardson stock list of plane ruled grating to select a proper grating for each spectral band. This should reduce a cost of the gratings although we have to note that stock gratings with suitable G may not be usable because their blaze angles are not appropriate for our application.

6.5.4.1 8 Virtual Slits

For the eight virtual slit configuration the slits would be arranged in a regular fashion in front of the IFS with 19.3 mm spacing. The length of each slit is 101 mm.

As an example to show how 8 spectra are distributed along the detector we use a constant deviation angle of 90° and a 281 mm EFL for camera optics. The latter is based on a 920 mm collimator EFL and a 0.305 magnification required by spatial sampling in the image slicer design. Table 19 shows parameters for selected diffraction gratings (α = CWL incident angle, β = diffraction angle, D_β = angular dispersion, R = resolution). For simplicity, a band CWL was used for any sub-band when deriving the listed values. To center a set of eight spectra for each band on the detector, the diffraction gratings should be adjusted in angle of rotation shown in Figure 35.

Using the diffraction grating with these parameters will yield the spectra distribution shown in Figure 36. Note that the shown distribution is mostly for illustration to see relationship between the spectrum positions. If needed, it can be adjusted by fine tuning of the grating angle.

Table 19: Diffraction grating parameters for an 8 virtual slit configuration

Passband	cut-on	CWL	cut-off	G	α	β	Dβ	R
	um	um	um	1/mm	deg	deg	1/mm	
Ia	0.700	0.738	0.777	200	-39.0	51.0	317.8	2385
Ib	0.777	0.815	0.853	200	-38.4	51.6	322.1	2668
Za	0.855	0.904	0.953	150	-39.5	50.5	235.8	2167
Zb	0.953	1.001	1.050	150	-38.9	51.1	238.8	2431
Ya	0.970	1.008	1.045	165	-38.2	51.8	266.5	2730
Yb	1.045	1.083	1.120	165	-37.7	52.3	269.5	2966
Ja	1.100	1.150	1.200	135	-38.7	51.3	215.9	2525
Jb	1.200	1.250	1.300	135	-38.1	51.9	218.6	2778
Jc	1.300	1.350	1.400	135	-37.6	52.4	221.3	3037
Ha	1.475	1.519	1.563	135	-36.7	53.3	226.1	3491
Hb	1.563	1.606	1.650	135	-36.2	53.8	228.7	3735
Hc	1.650	1.694	1.738	135	-35.7	54.3	231.4	3984
Hd	1.738	1.781	1.825	135	-35.2	54.8	234.1	4240
Ka	2.000	2.050	2.100	100	-36.7	53.3	167.5	3490
Kb	2.100	2.150	2.200	100	-36.3	53.7	169.1	3696
Kc	2.200	2.250	2.300	100	-35.8	54.2	170.8	3906
Kd	2.300	2.350	2.400	100	-35.4	54.6	172.5	4121

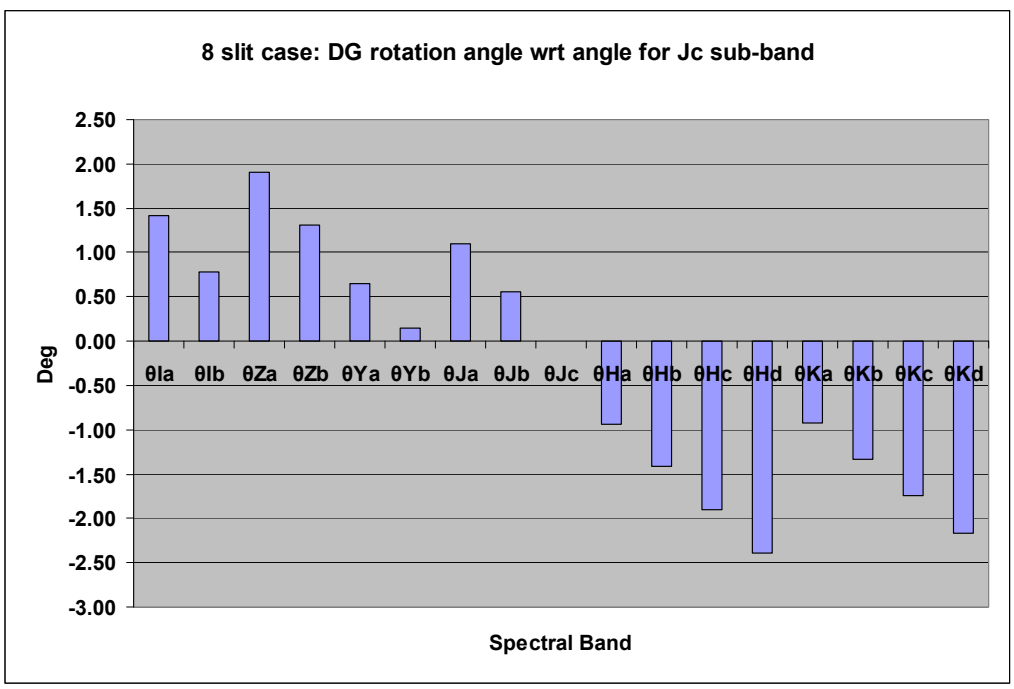

Figure 35: Rotation angles for gratings (8 virtual slits)

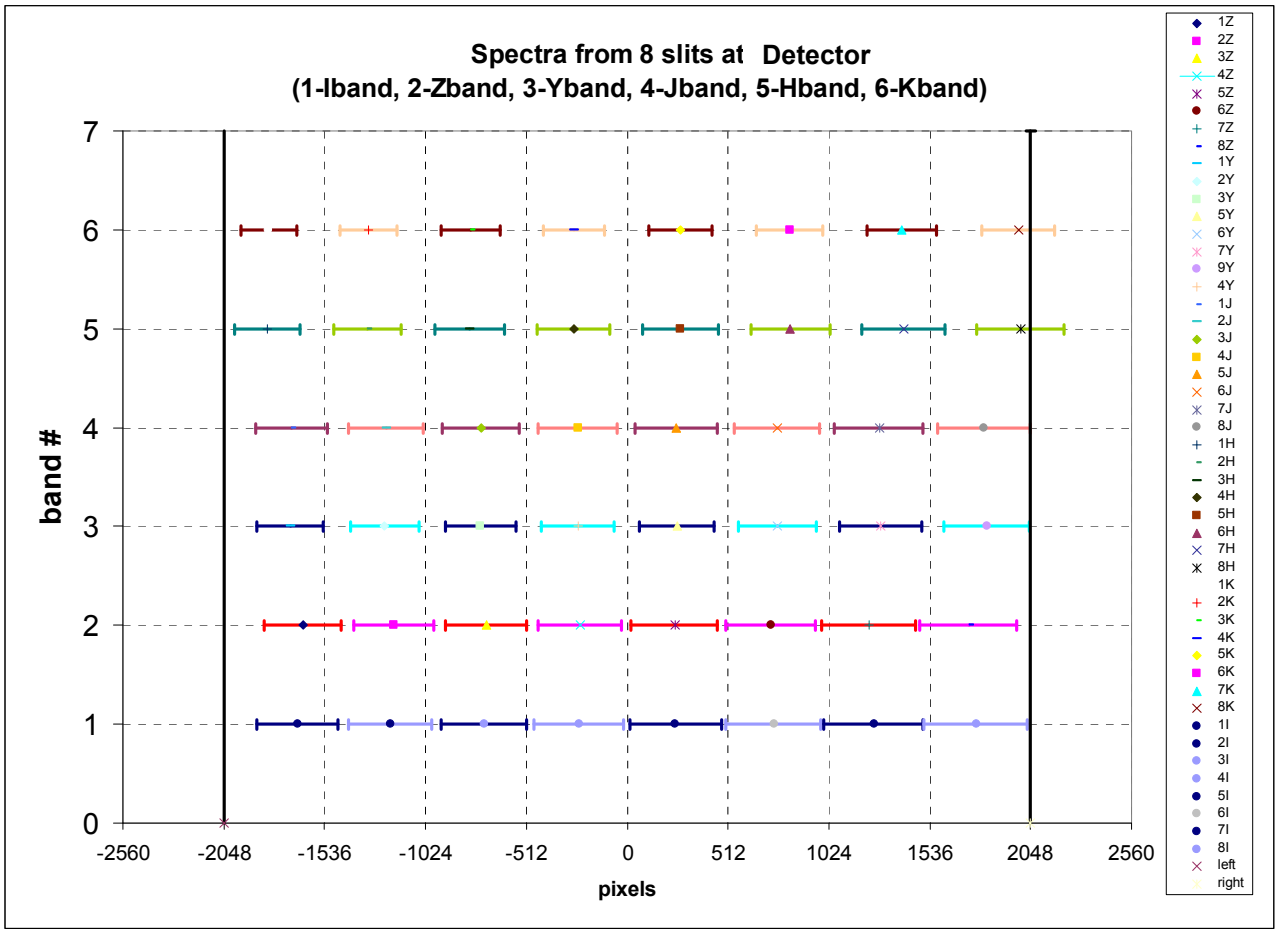

Figure 36: Distribution of spectra on the detector using 8 virtual slits

6.5.4.2 6 Virtual Slits

For the six virtual slit configuration the slits would be arranged in a regular fashion in front of the IFS with 24 mm spacing. The length of each slit is 141 mm.

As in the previous case, to show how spectra from 6 virtual slits are distributed along the detector we use a constant deviation angle of 90° but a different EFL of 275 mm for the camera optics. The latter is based on a 900 mm collimator EFL. Table 19 shows parameters for selected diffraction gratings (α = CWL incident angle, β = diffraction angle, D_β = angular dispersion, R = resolution). Again, for simplicity, a band CWL was used for any sub-band when deriving the listed values. To center a set of six spectra for each band on the detector, the diffraction gratings should be adjusted in the angle of rotation as shown in Figure 37.

Table 20: Diffraction grating parameters for a 6 virtual slit configuration

Passband	cut-on um	CWL um	cut-off um	G 1/mm	α deg	β deg	Dβ 1/mm	R
Ia	0.700	0.738	0.777	272.3	-36.8	53.2	454.3	3410
Ib	0.777	0.815	0.853	272.3	-36.0	54.0	463.5	3840
Za	0.855	0.904	0.953	210	-37.3	52.7	346.6	3185
Zb	0.953	1.001	1.050	210	-36.4	53.6	353.5	3598
Ya	0.970	1.008	1.045	245	-34.9	55.1	427.7	4381
Yb	1.045	1.083	1.120	245	-34.2	55.8	436.0	4798
Ja	1.100	1.150	1.200	180	-36.6	53.4	302.0	3531
Jb	1.200	1.250	1.300	180	-35.8	54.2	307.4	3906
Jc	1.300	1.350	1.400	180	-35.1	54.9	313.0	4296
Ha	1.475	1.519	1.563	150	-35.7	54.3	256.9	3966
Hb	1.563	1.606	1.650	150	-35.2	54.8	260.3	4250
Hc	1.650	1.694	1.738	150	-34.7	55.3	263.8	4543
Hd	1.738	1.781	1.825	150	-34.1	55.9	267.5	4844
Ka	2.000	2.050	2.100	135	-33.7	56.3	243.2	5069
Kb	2.100	2.150	2.200	135	-33.2	56.8	246.8	5395
Kc	2.200	2.250	2.300	135	-32.6	57.4	250.6	5732
Kd	2.300	2.350	2.400	135	-32.0	58.0	254.5	6080

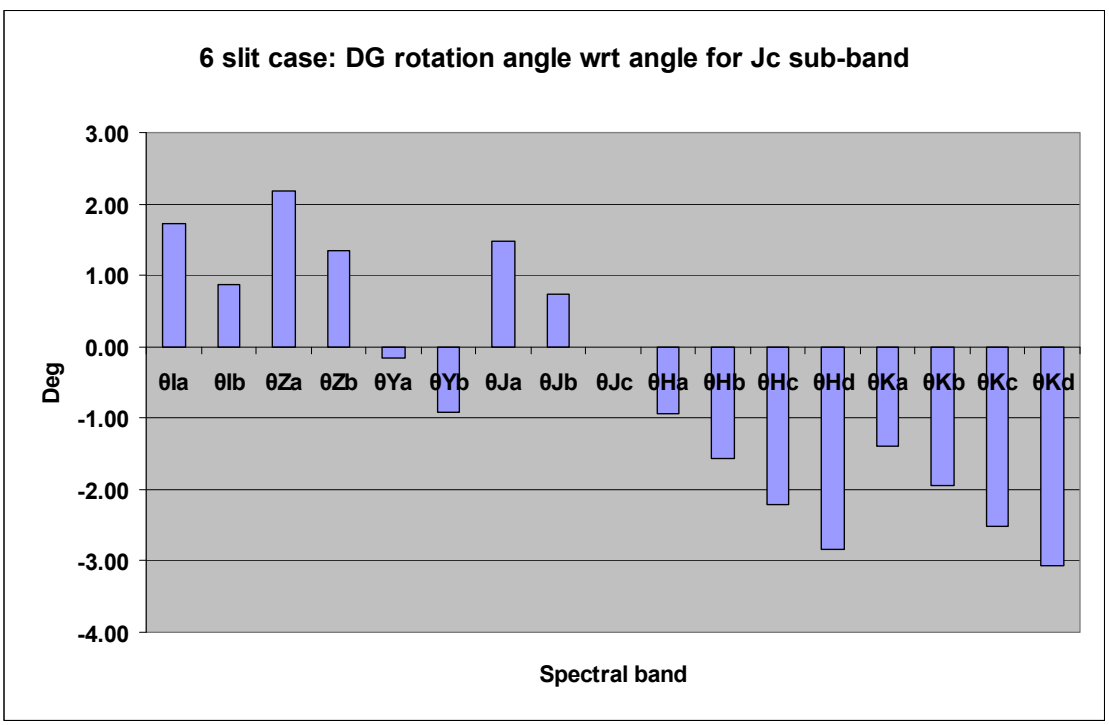

Figure 37: Rotation angles for gratings (6 virtual slits)

Using the diffraction grating with these parameters will yield the spectra distribution shown in Figure 38. Again, the shown distribution is mostly for illustration to see relationship between the spectrum positions. If needed, it can be also adjusted by fine turning of the rotation angle.

The spectrum length is maximized at the I-band and Z-band to meet the resolution requirement. This constrains the parameters for the IFS optics. With these parameters there are large gaps between the spectra for the H-band and the K-band. However the resolution is still sufficient (Table 19).

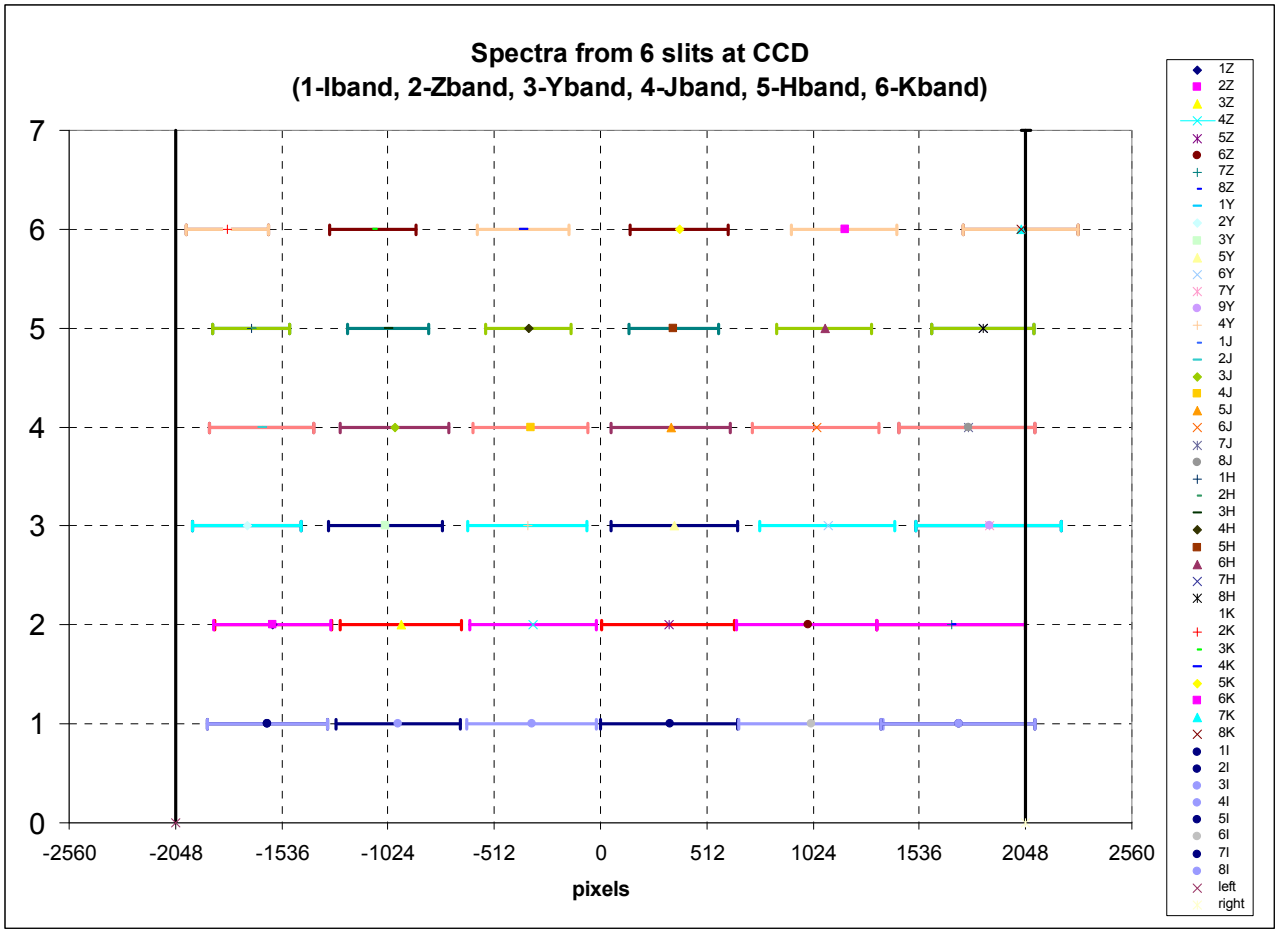

Figure 38: Distribution of spectra on the detector using 6 virtual slits

6.5.5 DAVINCI IFS Collimator and Camera

The basic parameters for the IFS collimator and camera with the hybrid slicer are shown in Table 21.

Table 21: IFS camera and collimator parameters

	Slit plane size		Collimator		Camera	
# of slits	X(spatial)	Y(spectral)	EFL	F#	EFL	F#
8	100.8	135.1	920	3.30	280.6	1.01
6	141.1	120.0	900	3.30	274.5	1.01

7 REFERENCES

Adkins, S. (2009, January 20). Keck Next Generation Adaptive Optics Detectors for NGAO Instrumentation. Keck Adaptive Optics Note 556. Waimea, HI: W. M. Keck Observatory.

Adkins, S. (2010). DAVINCI Plate Scales and Sensitivities. Waimea, HI: W. M. Keck Observatory.

Bacon, R., Adam, G., Baranne, A., Courtes, G., Dubet, D., Dubois, J. P., Emsellem, E., Ferruit, P., Georgelin, Y., Monnet, G., Pecontal, E., Rousset, A., & Say, F. (1995, October). *Astronomy and Astrophysics Supplement, 113*, 347-357.

Baek, M. & Marchis, F. (2007, November 27). Next Generation Adaptive Optics: Optimum Pixel Sampling for Asteroid Companion Studies. Keck Adaptive Optics Note 529. Waimea, HI: W. M. Keck Observatory.

Beck, T.L., McGregor, P. J., Takami, M. & Pyo, T. (2008). Spatially resolved molecular hydrogen emission in the inner 200 AU environments of classical T Tauri stars. *The Astrophysical Journal, 676*(1), 472-489.

Britton, M., Dekany, R., Flicker, R., Max, C., Neyman, C. & Olsen, K. (2007, April 10). AO Photometry for NGAO. Keck Adaptive Optics Note 474. Waimea, HI: W. M. Keck Observatory.

Cameron, B., Britton, M., Lu, J., Ghez, A., Dekany, R., Max, C. & Neyman, C. (2007, May 3). Astrometry for NGAO. Keck Adaptive Optics Note 480. Waimea, HI: W. M. Keck Observatory.

Content, R. (1997). New design for integral field spectroscopy with 8-m telescopes. In Arne L. Ardeberg, A. L. (ed.) *Optical Telescopes of Today and Tomorrow, 1872*, 1295-1305. Bellingham, WA: SPIE.

Chun, M., Toomey, D., Wahhaj, Z., Biller, B., Artigau, E., Hayward, T., Liu, M., Close, L., Hartung, M., Rigaut, F., & Ftaclas, C. (2008). Performance of the near-infrared coronagraphic imager on Gemini-South. *Proceedings of the SPIE, 7015*, 70151V1-70151V9.

Dekany, R., Neyman, C., Wizinowich, P., McGrath, E. & Max, C. (2009, March 10). Build-to-Cost Architecture Wavefront Error Performance. Keck Adaptive Optics Note 644. Waimea, HI: W. M. Keck Observatory.

Eikenberry,S. S., Elston, R., Guzman, R., Raines, S. N., Julian, J., Gruel, N., Boreman, G., Hoffmann, J., Rodgers, M., Glenn, P., Hull-Allen, G., Myrick, B., Flint, S., & Comstock, L. (2006). FISICA: The Florida image slicer for infrared cosmology and astrophysics. *New Astronomy Reviews, 50*(4-5), 365-369.

Hardy, J. W. (1998). *Adaptive optics for astronomical telescopes*. Oxford, UK: Oxford University Press.

Keck Next Generation Adaptive Optics Science Case Requirements Document. (2009, January 27). Keck Adaptive Optics Note 455 [Release 2.2_v6]. Waimea, HI: W. M. Keck Observatory.

Kulas, K. (2010, January). MOSFIRE detector testing status. Retrieved January 15, 2010 from http://irlab.astro.ucla.edu/mosfire/team/meetings/meeting63/20100115-MOSFIRE%20Detector-Kulas.ppt

Kupke, R. (2009, June 11). Keck NGAO Relay Design.

Larkin, J., Barczys, M., Krabbe, A., Adkins, S., Aliado, T., Amico, P., Brims, G., Campbell, R., Canfield, J., Gasaway, T., Honey, A., Iserlohe, C., Johnson, C., Kress, E., LaFreniere, D., Lyke, J., Magnone, K., Magnone, N., McElwain, M., Moon, J., Quirrenbach, A., Skulason, G., Song, I., Spencer, M, Weiss, J., Wright, S. (2006). OSIRIS: a diffraction limited integral field spectrograph for Keck. *New Astronomy Reviews, 50*(4-5), 362-364.

McLean, I. S., Steidel, C. C., Matthews, K., Epps, H., & Adkins, S. M. (2008). MOSFIRE: A multi-object near-infrared spectrograph for the Keck Observatory. *Proceedings of the SPIE, 7014*, 70142Z-70142Z-12.

MOSFIRE: Multi-Object Spectrograph for Infra-Red Exploration, detailed design report. (2007, April 6). http://irlab.astro.ucla.edu/mosfire/MOSFIRE%20DDR%20Report%20v2.pdf

Roth, M. M. (2006). PSF-fitting techniques for crowded field 3D spectroscopy. *New Astronomy Reviews, 49*, 573-581.

Sivaramakrishnan, A., Koresko, C. D., Makidon, R. B., Berkefeld, T., & Kuchner, M. J. (2001). Ground-based coronagraphy with high-order adaptive optics. *The Astrophysical Journal, 552*(1), 397-408.

Soummer, R. (2005). Apodized pupil Lyot coronagraphs for arbitrary telescope apertures. *The Astrophysical Journal, 618*(2), L161-L164.

8 APPENDIX A – ZEMAX PRESCRIPTION

8.1 DAVINCI Imager Zemax Prescription

System/Prescription Data

File:
\\.psf\Home\Desktop\Keck\designs\preliminary_design_phase\KNGAO_relay_v10+davinci_2tier_baseline.ZMX

Title: DAVINCI, 2-tier, Imager and IFS up to Lenslet array
Date : MON APR 12 2010
Configuration 1 of 2

GENERAL LENS DATA:

Surfaces : 94
Stop : 1
System Aperture : Entrance Pupil Diameter = 10949
Glass Catalogs : INFRARED MISC HERAEUS MOSFIRE
Ray Aiming : Real Reference, Cache On
X Pupil shift : 0
Y Pupil shift : 0
Z Pupil shift : 0
X Pupil compress : 0
Y Pupil compress : 0
Apodization : Uniform, factor = 0.00000E+000
Temperature (C) : 2.00000E+001
Pressure (ATM) : 1.00000E+000
Adjust Index Data To Environment : Off
Effective Focal Length : -172898.3 (in air at system temperature and pressure)
Effective Focal Length : -172898.3 (in image space)
Back Focal Length : -39.11141
Total Track : 20587.38
Image Space F/# : 15.79124
Paraxial Working F/# : 15.79124
Working F/# : 29.25044
Image Space NA : 0.03164726
Object Space NA : 5.4745e-007
Stop Radius : 5474.5
Paraxial Image Height : 12.81287
Paraxial Magnification : 0
Entrance Pupil Diameter : 10949
Entrance Pupil Position : 0
Exit Pupil Diameter : 8226.908

Exit Pupil Position : 240793
Field Type : Angle in degrees
Maximum Radial Field : 0.005556
Primary Wavelength : 1.17 ╡m
Lens Units : Millimeters
Angular Magnification : 1042.323

Fields : 9
Field Type: Angle in degrees

#	X-Value	Y-Value	Weight
1	0.000000	0.000000	100.000000
2	-0.002778	0.000000	3.000000
3	0.002778	0.000000	3.000000
4	0.000000	-0.002778	3.000000
5	0.000000	0.002778	3.000000
6	0.000000	0.005556	3.000000
7	0.000000	-0.005556	3.000000
8	0.005556	0.000000	3.000000
9	-0.005556	0.000000	3.000000

Vignetting Factors

#	VDX	VDY	VCX	VCY	VAN
1	0.000000	0.000000	0.000000	0.000000	0.000000
2	0.000000	0.000000	0.000000	0.000000	0.000000
3	0.000000	0.000000	0.000000	0.000000	0.000000
4	0.000000	0.000000	0.000000	0.000000	0.000000
5	0.000000	0.000000	0.000000	0.000000	0.000000
6	0.000000	0.000000	0.000000	0.000000	0.000000
7	0.000000	0.000000	0.000000	0.000000	0.000000
8	0.000000	0.000000	0.000000	0.000000	0.000000
9	0.000000	0.000000	0.000000	0.000000	0.000000

Wavelengths : 6
Units: ╡m

#	Value	Weight
1	1.170000	1.000000
2	1.400000	1.000000
3	1.800000	1.000000
4	2.200000	1.000000
5	2.400000	0.500000
6	0.852000	1.000000

SURFACE DATA SUMMARY:

Surf	Type	Radius	Thickness	Glass	Diameter	Conic	Comment
OBJ	STANDARD	Infinity	Infinity		0	0	
STO	STANDARD	-34974	-15394.99	MIRROR	10949	-1.003683	Keck Primary
2	STANDARD	-4737.916	15394.99	MIRROR	1317.129	-1.644326	Keck Secondary
3	STANDARD	Infinity	2227		208.4837	0	
4	STANDARD	Infinity	272.6466		1000	0	Bulkhead
5	STANDARD	Infinity	-121		29.01261	0	
6	COORDBRK	-	0		-	-	K-mirror rotation
7	STANDARD	Infinity	-243.5	MIRROR	80.38487	0	K mirror 1
8	STANDARD	Infinity	243.5	MIRROR	45.03469	0	K mirror 2
9	STANDARD	Infinity	-150	MIRROR	120.4903	0	K mirror 3
10	STANDARD	Infinity	-247.5		67.5545	0	
11	COORDBRK	-	0		-	-	
12	STANDARD	Infinity	0	MIRROR	107.1503	0	
13	COORDBRK	-	0		-	-	
14	COORDBRK	-	-763.5		-	-	derotate, go 2 focus
15	COORDBRK	-	1276.746		-	-	start 100mm relay
16	STANDARD	-2553.493	0	MIRROR	1261.576	-1	oap1
17	COORDBRK	-	-1492.194		-	-	
18	COORDBRK	-	0		-	-	
19	SZERNSAG	Infinity	0	MIRROR	100.4568	0	100 mm pupil
20	COORDBRK	-	0		-	-	
21	STANDARD	Infinity	625		99.11726	0	
22	COORDBRK	-	0		-	-	start LGS dich
23	STANDARD	Infinity	20	SILICA	190	0	LGS dichroic
24	STANDARD	Infinity	0		190	0	
25	COORDBRK	-	0		-	-	end LGS dich
26	STANDARD	Infinity	-645		111.9833	0	
27	COORDBRK	-	1408.95		-	-	
28	STANDARD	-2553.493	0	MIRROR	1258.904	-1	oap2
29	COORDBRK	-	-500		-	-	
30	STANDARD	Infinity	-908.7574		96.09241	0	relay 1, end
31	STANDARD	Infinity	-100		29.15745	0	intermediate focus
32	COORDBRK	-	0		-	-	
33	STANDARD	Infinity	0	MIRROR	53.41566	0	fold to second relay
34	COORDBRK	-	-100		-	-	
35	COORDBRK	-	317.9877		-	-	
36	STANDARD	-635.9754	0	MIRROR	197.37	-1	OAP 3
37	COORDBRK	-	-326.2408		-	-	
38	COORDBRK	-	0		-	-	
39	SZERNSAG	Infinity	0	MIRROR	24.42455	0	tweeter
40	COORDBRK	-	0		-	-	

41	COORDBRK	-	1234.04	-	-	
42	STANDARD	-1907.925	0	MIRROR	1581.917	-1 OAP4
43	COORDBRK	-	-350	-	-	
44	COORDBRK	-	0	-	-	
45	STANDARD	Infinity	0	MIRROR	127.9385	0 switchyard
46	COORDBRK	-	400	-	-	
47	STANDARD	Infinity	437	110.2178	0	
48	STANDARD	Infinity	25	INFRASIL	120	0 dewar window
49	STANDARD	Infinity	78.556	120	0	
50	COORDBRK	-	999.3693	-	-	
51	STANDARD	-1998.737	0	MIRROR	1634.063	-1 oap1_instr
52	COORDBRK	-	-700	-	-	
53	COORDBRK	-	0	-	-	
54	STANDARD	Infinity	0	MIRROR	80.80314	0
55	COORDBRK	-	0	-	-	
56	STANDARD	Infinity	586.4909	75.23125	0	
57	STANDARD	Infinity	0	26.59406	0	cold stop
58	STANDARD	Infinity	888.292	26.59406	0	
59	COORDBRK	-	0	-	-	
60	STANDARD	-1531.855	0	MIRROR	961.4958	-1 oap2_instr
61	COORDBRK	-	-474.9427	-	-	
62	STANDARD	Infinity	-423.5805	85.66672	0	
63	STANDARD	Infinity	0	74.75814	0	ifs pickoff
64	COORDBRK	-	0	-	-	
65	STANDARD	Infinity	0	MIRROR	90	0 fold up to 2nd tier
66	COORDBRK	-	300	-	-	
67	COORDBRK	-	0	-	-	
68	STANDARD	Infinity	0	MIRROR	100	0 periscope
69	COORDBRK	-	0	-	-	
70	STANDARD	Infinity	300	83.09185	0	
71	COORDBRK	-	-516.5	-	-	
72	STANDARD	1034.001	0	MIRROR	1317.671	-1 oap3_instr
73	COORDBRK	-	879.1171	-	-	
74	STANDARD	Infinity	0	25.84208	0	
75	STANDARD	Infinity	735.41	25.84208	0	
76	COORDBRK	-	0	-	-	
77	STANDARD	-962.1413	0	MIRROR	1074.076	-1 oap4_instr
78	COORDBRK	-	-828	-	-	
IMA	STANDARD	Infinity		62.80239	0	detector

8.2 JHK Scale Changer

System/Prescription Data

File:
\\.psf\Home\Documents\Dropbox\KNGAO_instrument_only_wifs_scalechanger_jhk_2ndrelayfixed.ZMX

Title: Scale changing optics, JHK, DAVINCI IFS
Date : MON APR 12 2010
Configuration 1 of 3

LENS NOTES:
config 1 800
config 2 801
config 3 802

GENERAL LENS DATA:

Surfaces : 12
Stop : 1
System Aperture : Object Space NA = 0.01489
Telecentric Object Space: On
Glass Catalogs : MISC SCHOTT HERAEUS OHARA INFRARED MOSFIRE
Ray Aiming : Off
Apodization : Uniform, factor = 0.00000E+000
Temperature (C) : 2.00000E+001
Pressure (ATM) : 1.00000E+000
Adjust Index Data To Environment : Off
Effective Focal Length : 1e+010 (in air at system temperature and pressure)
Effective Focal Length : 1e+010 (in image space)
Back Focal Length : -5.131667e+013
Total Track : 922.707
Image Space F/# : 33.57586
Paraxial Working F/# : 2405.249
Working F/# : 2406.073
Image Space NA : 0.0002078787
Object Space NA : 0.01489
Stop Radius : 0.1024682
Paraxial Image Height : 52.00792
Paraxial Magnification : 71.63625
Entrance Pupil Diameter : 2.97833e+008
Entrance Pupil Position : 1e+010
Exit Pupil Diameter : 4157574
Exit Pupil Position : 1e+010
Field Type : Object height in Millimeters

Maximum Radial Field : 0.726
Primary Wavelength : 1.475 ╡m
Lens Units : Millimeters
Angular Magnification : -1.911541e-007

Fields : 5
Field Type: Object height in Millimeters

#	X-Value	Y-Value	Weight
1	0.000000	0.000000	100.000000
2	-0.726000	0.000000	50.000000
3	0.726000	0.000000	50.000000
4	0.000000	-0.726000	50.000000
5	0.000000	0.726000	50.000000

Vignetting Factors

#	VDX	VDY	VCX	VCY	VAN
1	0.000000	0.000000	0.000000	0.000000	0.000000
2	0.000000	0.000000	0.000000	0.000000	0.000000
3	0.000000	0.000000	0.000000	0.000000	0.000000
4	0.000000	0.000000	0.000000	0.000000	0.000000
5	0.000000	0.000000	0.000000	0.000000	0.000000

Wavelengths : 5
Units: ╡m

#	Value	Weight
1	1.475000	1.000000
2	1.800000	10.000000
3	2.200000	1.000000
4	2.400000	1.000000
5	1.170000	1.000000

SURFACE DATA SUMMARY:

Surf	Type	Radius	Thickness	Glass	Diameter	Conic	Comment
OBJ	STANDARD	Infinity	6.880918		1.452	0	
STO	STANDARD	6.773085	2	BAF2H120	10	0	
2	STANDARD	-6.806842	6.877347		10	0	
3	STANDARD	Infinity	138.416		0.2444866	0	
4	STANDARD	441.2625	5	BAF2H120	30	0	
5	STANDARD	-77.74181	140.8071		30	0	
6	STANDARD	Infinity	59.90376		27.14098	0	
7	STANDARD	103.7206	8	BAF2H120	30	0	
8	STANDARD	-41.10468	62.30034		30	0	
9	STANDARD	Infinity	237.425		4.199363	0	

10 STANDARD	220.9268	25	BAF2H120	130	0
11 STANDARD	-232.6481	236.9774		130	0
IMA STANDARD	Infinity			104.897	0

8.3 IZ Scale Changer

System/Prescription Data

File:
\\.psf\Home\Documents\Dropbox\KNGAO_instrument_only_wifs_scalechanger_iz_2ndrelayfixed.ZMX

Title: Scale changing optics, IZ, DAVINCI IFS
Date : MON APR 12 2010
Configuration 3 of 3

LENS NOTES:
config 1 800
config 2 801
config 3 802

GENERAL LENS DATA:

Surfaces : 12
Stop : 1
System Aperture : Object Space NA = 0.01489
Telecentric Object Space: On
Glass Catalogs : MISC SCHOTT HERAEUS OHARA INFRARED MOSFIRE
Ray Aiming : Off
Apodization : Uniform, factor = 0.00000E+000
Temperature (C) : 2.00000E+001
Pressure (ATM) : 1.00000E+000
Adjust Index Data To Environment : Off
Effective Focal Length : 1e+010 (in air at system temperature and pressure)
Effective Focal Length : 1e+010 (in image space)
Back Focal Length : -1.697669e+012
Total Track : 895.2639
Image Space F/# : 33.57586
Paraxial Working F/# : 437.4752
Working F/# : 437.6136
Image Space NA : 0.001142921
Object Space NA : 0.01489
Stop Radius : 0.5126384
Paraxial Image Height : 47.29692
Paraxial Magnification : 13.02945
Entrance Pupil Diameter : 2.97833e+008

Entrance Pupil Position : 1e+010
Exit Pupil Diameter : 2.285844e+007
Exit Pupil Position : 1e+010
Field Type : Object height in Millimeters
Maximum Radial Field : 3.63
Primary Wavelength : 0.85211 ╡m
Lens Units : Millimeters
Angular Magnification : -0

Fields : 5
Field Type: Object height in Millimeters

#	X-Value	Y-Value	Weight
1	0.000000	0.000000	100.000000
2	-3.630000	0.000000	50.000000
3	3.630000	0.000000	50.000000
4	0.000000	-3.630000	50.000000
5	0.000000	3.630000	50.000000

Vignetting Factors

#	VDX	VDY	VCX	VCY	VAN
1	0.000000	0.000000	0.000000	0.000000	0.000000
2	0.000000	0.000000	0.000000	0.000000	0.000000
3	0.000000	0.000000	0.000000	0.000000	0.000000
4	0.000000	0.000000	0.000000	0.000000	0.000000
5	0.000000	0.000000	0.000000	0.000000	0.000000

Wavelengths : 2
Units: ╡m

#	Value	Weight
1	0.852110	10.000000
2	0.970000	1.000000

SURFACE DATA SUMMARY:

Surf	Type	Radius	Thickness	Glass	Diameter	Conic	Comment
OBJ	STANDARD	Infinity	34.42455		7.26	0	
STO	STANDARD	47.25033	2	BAF2H120	8.290703	0	
2	STANDARD	-25.45857	34.83521		8.237032	0	
3	STANDARD	Infinity	112.0518		1.193918	0	
4	STANDARD	96.13798	5	BAF2H120	24.77758	0	
5	STANDARD	-119.5316	111.6808		24.97922	0	
6	STANDARD	Infinity	57.35812		23.56845	0	
7	STANDARD	100.2095	8	BAF2H120	23.75944	0	
8	STANDARD	-39.73282	59.74962		23.3489	0	
9	STANDARD	Infinity	240.8639		3.336565	0	

10 STANDARD	205.3838	25	BAF2H120	107.1103	0
11 STANDARD	-263.4573	238.7245		108.3315	0
IMA STANDARD	Infinity			95.82192	0

9 APPENDIX B: ATMOSPHERE AND SYSTEM TRANSMISSIONS

	Cut-on, nm	Cut-off, nm	Atmosphere	Atmosphere, average	AO system	AO system, average
I band						
S, P	700		91.37%	92.26%	44.45%	51.05%
S, P		853	93.15%		57.64%	
Z band						
S	855		93.15%	96.56%	57.64%	57.98%
S		1050	99.97%		58.33%	
P	818		92.90%	96.04%	55.59%	57.57%
P		922	99.18%		59.54%	
Y band						
S	970		99.31%	92.02%	61.08%	59.84%
S		1120	84.74%		58.60%	
P	970		99.31%	99.63%	61.08%	60.51%
P		1070	99.96%		59.93%	
J band						
S	1100		98.72%	63.67%	58.65%	58.56%
S		1400	28.62%		58.47%	
P	1170		99.22%	97.76%	57.48%	57.90%
P		1330	96.30%		58.31%	
H band						
S	1475		96.58%	86.40%	59.59%	61.15%
S		1825	76.23%		62.70%	
P	1490		95.38%	97.10%	59.75%	60.76%
P		1780	98.82%		61.78%	
K band						
S	2000		63.46%	79.31%	62.81%	62.25%
S		2400	95.16%		61.69%	
P	2030		97.19%	90.73%	62.73%	62.23%
P		2370	84.27%		61.73%	

Table 22: Atmosphere and AO system throughput estimates

Cut-on and cut-off wavelengths for spectroscopic (S) and photometric (P) bands shown in nm, green highlighted values used for background predictions.

	Cut-on, nm	Cut-off, nm	R ave. %	3 ref. %
I band	700	853	86.99	65.82
Z band	855	1050	91.58	76.81
Y band	970	1120	94.42	84.18
J band	1100	1400	96.22	89.09
H band	1475	1825	97.13	91.62
K band	2000	2400	97.35	92.26

Table 23: Keck telescope transmission